University of Alberta

Preamplifier Noise Figure Measurement and Radio Frequency Field Optimization in High Field Magnetic Resonance Imaging

by

Russell Luke Lagore

A thesis submitted to the Faculty of Graduate Studies and Research
in partial fulfillment of the requirements for the degree of

Master of Science

Department of Biomedical Engineering

Fall 2013
Edmonton, Alberta

Abstract

High field magnetic resonance imaging (MRI) is an area of research interest due to the associated improvement in image quality possible. This improvement comes at a cost. Hardware design becomes more complex in order to overcome technical challenges at these higher field strengths. Signal-to-noise ratio is of paramount importance to MR image quality and this comes from carefully designed hardware and pulse sequences.

This thesis focuses on the radiofrequency hardware of a high field MRI system. As frequency increases, the difficulties associated with radiofrequency hardware design increase.

A noise figure and noise parameter measurement system was developed for measurement of the noise added by measurement electronics in MRI. Noise figure was found to increase for many transistor semiconductors as magnetic field increased.

The radiofrequency transmit field was also studied. Radiofrequency hardware was modified to optimize the radiofrequency field to achieve proper contrast in MR images and improve transmit power efficiency.

Acknowledgements

I would like to thank my supervisors Drs. Nicola De Zanche and Alan H. Wilman for all their guidance and patience. Thank you to the support staff at the Peter S. Allen MR Research Centre. In particular, thanks to Mr. Peter Seres for teaching me how to run the 4.7 T console and Mr. Al-Karim Damji for spending hours working with me on various projects. Thank you to Corey Baron for inspiring my TORO coil rotation experiment and Kelly McPhee for discovering that my B_1 mapping method was, in fact, correct from the outset. Thanks to Hongfu, Dylan, Kelly, Luke, and Amanda for being willing volunteers for my MRI experiments.

With regards to the noise figure work, thanks to Dr. Kambiz Moez for access to the HP8970A noise figure meter, Mr. Al-Karim Damji for assistance with measurements at 200 MHz, and Philips and InVivo for the preamplifiers and assistance. Thanks to my co-authors Brodi Roberts, Drs. Cecilia Possanzini, Charles Saylor, B. Gino Fallone, and Nicola De Zanche.

I thank God for the opportunity I have to pursue higher education. Thank you Mom and Dad for reading my long e-mails and providing advice and support. Thanks to Amanda, my sister, for always believing in and encouraging me. Thank you to Melodie, my wife, for supporting me emotionally and seeing me through the good and the bad of this degree. To Tim, my pastor and friend, thank you for the timely encouragement over a cup of coffee. Thank you Grandma and Grandpa for everything you've done to help me through the past eight years of university! I'm sure there are others who deserve recognition who I've missed. If you're one of those people reading this now: Thank you!

Funding I would like to acknowledge funding from my supervisor (Alan H. Wilman) via a CIHR operating grant, the Heritage Scholarship from the province of Alberta, the J Gordin Kaplan Graduate Student Travel Award, and two Queen Elizabeth II scholarships from the University of Alberta. Research was funded by grants from the Natural Sciences and Engineering Research Council (Canada).

Contents

1 High Field Magnetic Resonance Imaging and Radio Frequency Hardware 1

1.1 Introduction . . . 1
1.2 Motivation . . . 1
1.3 Nuclear Magnetic Resonance . . . 2
1.4 Magnetic Resonance Imaging . . . 2
  1.4.1 The B_0 Field . . . 3
  1.4.2 The B_1 Field . . . 5
1.5 RF Circuit Concepts . . . 8
  1.5.1 Impedance and Admittance . . . 8
  1.5.2 Transmission Line Theory . . . 9
  1.5.3 S-parameters . . . 11
  1.5.4 Reflection Coefficients . . . 11
  1.5.5 Smith Chart . . . 12
1.6 MRI RF Hardware . . . 14
  1.6.1 RF Coils . . . 14
  1.6.2 Surface Coils . . . 14
  1.6.3 The Birdcage RF Coil . . . 15
  1.6.4 Quadrature Drive . . . 17
  1.6.5 Quadrature Hybrid Coupler . . . 19

2 Noise Figure of MRI Preamplifiers 21

2.1 Summary . . . 21
2.2 Introduction . . . 21
  2.2.1 Motivation . . . 21
  2.2.2 Noise Figure Basics . . . 22
  2.2.3 Noise Figure Correction Factors . . . 23
2.3 The Noise Figure Measurement System . . . 24
  2.3.1 Hardware Setup . . . 25
  2.3.2 Measurement Procedure . . . 27
  2.3.3 Performance Optimization and Validation . . . 29
  2.3.4 Results . . . 30
2.4 Characterization in Strong Magnetic Fields . . . 31
  2.4.1 Measurement Setup and Corrections . . . 32
  2.4.2 Results . . . 34
2.5 Noise Parameter Measurements . . . 36
  2.5.1 Linear Noise Model . . . 36
  2.5.2 Tuner Design . . . 37
  2.5.3 Calibrations . . . 38
  2.5.4 Results . . . 40
2.6 Conclusions and Future Work . . . 43

3 B_1 Shimming via Quadrature Phase Shifting 45
3.1 Summary . . . 45
3.2 Introduction . . . 46
  3.2.1 Circularly Polarized B_1 Field . . . 46
  3.2.2 B_1 Mapping . . . 46
  3.2.3 B_1 Shimming . . . 47
  3.2.4 Hardware . . . 48
  3.2.5 Motivation . . . 50
3.3 Phantoms for Phase Shifting Experiments . . . 51
3.4 RF Hardware Port Loading . . . 52
  3.4.1 B_1 Field Variation . . . 52
  3.4.2 Electrical Measurements . . . 55
  3.4.3 Discussion . . . 56
3.5 Phase Shifting . . . 57
  3.5.1 Phase Shifting with Coaxial Adapters . . . 57
  3.5.2 Phase Shifting with a Line Stretcher . . . 59
3.6 Positioning of the Transmit Coil and Phantom . . . 62
  3.6.1 Transmit Coil Rotation . . . 62
  3.6.2 Transmit Coil Translation . . . 63
  3.6.3 Translation of the Phantom . . . 65
  3.6.4 Transmit Power Efficiency . . . 65
3.7 Phantom Evaluation . . . 66
3.8 B_1 Maps of Individual Transmit Ports . . . 67
  3.8.1 Computing B_1 Field for the Circularly Polarized Coil . 67
  3.8.2 Elliptical Polarization . . . 69
  3.8.3 Computing Optimum Phase Shift for B_1 Shimming . . 70
3.9 Current Limitations and Future Work . . . 72
3.10 Conclusions . . . 73

4 Conclusion 75
4.1 Noise Figure of MRI Preamplifiers . . . 75
  4.1.1 Summary . . . 75
  4.1.2 Results and Conclusions . . . 75
  4.1.3 Future Work . . . 76
4.2 B_1 Shimming via Quadrature Phase Shifting . . . 76
  4.2.1 Summary . . . 76
  4.2.2 Results and Conclusions . . . 76
  4.2.3 Future Work . . . 77
4.3 RF Hardware in High Field MRI . . . 78

5 References 79

List of Tables

1 Noise souce ENR table 25
2 Noise figure comparison 31
3 Noise parameter results and comparison 40
4 BF998 noise parameter comparison. 42
5 Invivo preamp noise parameter comparison. 43
6 Coupling and reflection coefficients of the quad hybrid 56
7 S-parameters of the transmit coil 56
8 Line-stretcher phase measurements. 59
9 B_1 scaling factors and phase offsets. 68

List of Figures

1 The B_0 and B_1 field relative to magnet bore 3
2 Magnetization of an imaging sample. 4
3 The Smith chart 13
4 Block diagram of the RF system 14
5 Surface RF coil 15
6 The birdcage RF coil 16
7 Linearly vs. circularly polarized B_1 field 18
8 Branchline coupler 20
9 NF measurement system GUI 25
10 Block diagram of NF measurement system 26
11 Test fixtures 28
12 B_0 variation along the magnet bore. 32
13 In-bore measurement setup 33
14 Effect of B_0 on NF, G_a, I, and S_{11} (128 MHz). 35
15 Effect of B_0 on NF and G_a (200 MHz). 36
16 Varactor Tuning Board circuit diagram. 37
17 Smith chart of Y_{opt} and Varactor Tuning Board coverage. . . . 39
18 Linear noise parameter plots. 41
19 TORO birdcage coil cross-sectional view 48
20 4-element array coil images. 49
21 Image shading and inhomogeneous B_1 map. 50
22 Phase Shift Phantom 51
23 B_1 difference maps for the loaded vs. unloaded quad hybrid. . 54
24 Block diagram of TORO and quad hybrid 55
25 Silicone oil phantom B_1 maps. 58
26 Preliminary phase shifting B_1 maps. 58
27 Line-stretcher phase shifting B_1 maps 59
28 TORO B_1 maps before and after repair. 60
29 Post-repair small increment phase shifting B_1 maps. 61
30 B_1 maps for large phase shifts. 61

31 B_1 maps comparing transmit coil rotations. 62
32 B_1 maps in two slices of a phantom. 63
33 TORO birdcage coil Z-axis and markings 64
34 B_1 maps comparing transmit coil positions. 64
35 B_1 field at boundary of phantom. 66
36 Port B_1 maps and phase difference. 67
37 Elliptically polarized coil 69
38 Experimental vs. computed B_1 maps 71

1 High Field Magnetic Resonance Imaging and Radio Frequency Hardware

1.1 Introduction

Magnetic Resonance Imaging, or MRI, is a medical imaging modality that exploits nuclear magnetic resonance (NMR) of certain atomic species. The rapid growth of MRI over the past 30 to 40 years [1] is due, in part, to MRI's superior soft tissue contrast and use of non-ionizing radiation [2].

A continuing area of interest is in high field MRI. While clinical systems employ magnetic field strengths of 1.5 tesla (T), and more recently, 3.0 T; the push is always towards greater field strength due to the increased signal-to-noise ratio (SNR) potential [3]. Popular high field magnets are 4 T, 7 T, and 9.4 T. There are unfortunately significant technical difficulties that arise at high magnetic field strengths [3, 4]. These difficulties are being addressed with new software and hardware techniques [5, 6].

The Peter S. Allen MR Research Centre at the University of Alberta hospital (Edmonton, Alberta) has three research MRI systems: 1.5 T, 3 T, and 4.7 T. High field MRI research conducted by the Department of Biomedical Engineering takes place on the 4.7 T system. Furthermore, the Department of Oncology has access to a 3 T human MRI system and 9.4 T animal MRI system located at the Cross Cancer Institute (Edmonton, Alberta). This thesis focuses on radio frequency (RF) hardware in high field MRI at field strengths of 3 T, 4.7 T and beyond.

1.2 Motivation

Good MR image quality requires high contrast, which depends on the pulse sequences used, but also on uniform contrast and high SNR.

High SNR allows one to differentiate detail of the imaging sample from the background noise. Higher SNR can additionally allow for increased resolution in images which brings out fine detail that can not be seen at lower resolutions. High field MRI has the benefit of higher SNR over lower field MRI, however SNR can be lost if the design of the receive coil and receive chain is not carefully considered. By understanding the noise behavior of measurement electronics as the magnetic field strength increases, strategies can be developed to minimize the noise added by these measurement electronics, thus preserving SNR. The noise figure of MRI preamplifiers (the measurement electronics) is studied in Chapter 2 of this thesis.

Good contrast in an image requires uniform sensitivity without dark and bright spots that are unrelated to the anatomy of the imaging sample. This uniform sensitivity is achieved by optimizing the transmit radio frequency field which is responsible for this uniform sensitivity. Optimization of transmit power efficiency and radio frequency field homogeneity using existing radio frequency hardware is explored in an attempt to achieve high contrast throughout an MR image. Optimization of this radio frequency field is discussing in Chapter 3 of this thesis.

It is important to understand the basics of MRI in order to properly understand and appreciate the role of RF hardware in an MRI system. Because not all subsystems or concepts of MRI are important to this thesis, a comprehensive background on MRI is not provided. This is better left to textbooks on the topic written by more knowledgeable authors. This introductory chapter will describe fundamentals of MRI pertinent to RF hardware for high field MRI so those with an electrical engineering background are able to grasp the research projects later in the thesis. For those who are familiar with MRI, this chapter also provides a brief explanation of electrical engineering concepts necessary to understand RF hardware.

1.3 Nuclear Magnetic Resonance

Nuclear Magnetic Resonance (NMR) relies on the nuclear magnetic moments of certain atomic species. Any atomic species posessing an odd mass or atomic number has a nuclear magnetic dipole moment and spin. When an atomic species with a magnetic moment is placed within a strong magnetic field, a net magnetization results. Resonance refers to the fact that atoms will precess, or spin, about the axis of magnetization [7,8]. Since this magnetization precesses about the axis of the strong magnetic field, it cannot be directly measured. The magnetic dipoles making up the magnetization can be excited. This spin excitation is visualized as a tipping of the magnetization vector into the plane perpendicular to the strong magnetic field. This flipping of the magnetization is achieved with a magnetic field which rotates at the same frequency as the atomic spins. The resulting magnetization spins in the transverse plane (perpendicular to the strong magnetic field) about the strong magnetic field's axis. The time-varying magnetic field produced by the rotating magnetization can be measured due to the changing magnetic flux using a simple loop or coil of wire. The changing magnetic flux induces a very weak electromotive force (*emf*) on the wire [9, pg. 1-21] which can be amplified, digitized, and processed by a computer.

1.4 Magnetic Resonance Imaging

The nuclear species that is most useful to MRI is hydrogen (^{1}H) which is composed of one proton and no neutrons. Hydrogen is so useful because the imaging sample of most interest to researchers is the human body (or other animals). The human body has a high abundance of hydrogen in the form of water and fat. In addition to its natural abundance, it's also isotopically abundant. Lastly, hydrogen has a high gyromagnetic ratio, which means that the resonant frequency at which it precesses is higher than other atomic species [8, 10]. A higher frequency translates to a greater amount of induced *emf*, and hence, higher signal-to-noise ratio (SNR) [11]. As higher magnetic fields are used, the frequency of other atomic species increases to a point where they become interesting research areas. One example is Sodium (^{23}Na) imaging. These atomic species still suffer from low isotopic and natural abundance, however, and suffer greatly in terms of SNR.

The signal produced by the flipped magnetization cannot be interpreted into an image without additional work since the signal cannot be localized and emanates from the entire imaging sample. As mentioned earlier, the resonant frequency of the proton spins increases as magnetic field strength increases [9, pg. 1-21]. The rate at which frequency (ω) increases with magnetic field (B) is expressed as

$$\omega = \gamma B \tag{1}$$

where γ is the gyromagnetic ratio of the atomic species (usually hydrogen). Therefore, by changing the magnetic field strength, the frequency of precession will change. If magnetic field strength changes with position, then frequencies can be interpreted as position with knowledge of the field variation. In MRI, the signal is spatially encoded in frequency during signal acquisition using gradient magnetic fields in three axes which are superimposed on the main magnetic field. The resulting frequency spectrum can be interpreted as an image using a fast Fourier transform to convert from the frequency domain to spatial domain [12, 13].

1.4.1 The B_0 Field

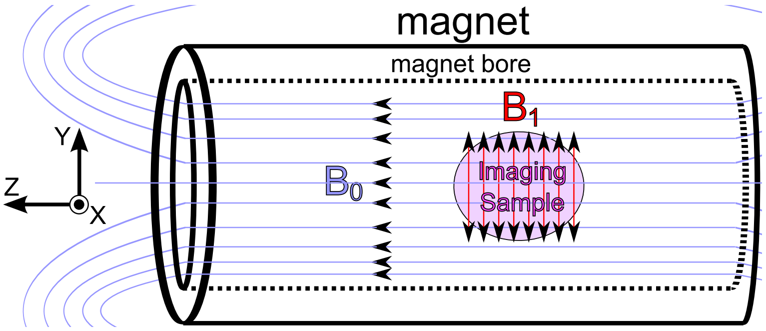

Figure 1: The magnet bore and B_0 field direction is defined as the Z-axis with the X and Y axes defined relative to this axis. The B_1 field is in the plane perpendicular (illustrated with double arrows) to the B_0 field in the XY-plane.

The B_0 field is the name given to the strong magnetic field used in MRI to create a magnetization in the imaging sample. This field must be homogeneous throughout the imaging sample so that the frequency of proton spins is equal in every part of the sample and when a gradient field is superimposed, the frequency of spins does indeed relate to their exact position. Images acquired using an inhomogeneous B_0 field can be warped due to an assumption of the magnetic field strength at a specific location. The B_0 field must also be extremely strong. While permanent magnets can be used for low field strength MRI, the magnet used for human high field imaging is always a cryogenic superconducting electromagnet. The magnet has a central bore where a strong, homogeneous B_0 field is generated [14]. This magnet bore and the B_0 field are usually defined as the Z-axis in the coordinate system for MRI. Other axes are defined relative to this axis (figure 1)

When a sample containing protons is placed in the B_0 field, the protons' magnetic moments align parallel and anti-parallel to the B_0 field (see figure 2). Protons align parallel or anti-parallel to the magnetic field based on their spin state (+1/2 or -1/2). The higher energy state is responsible for the anti-parallel magnetization, and the lower energy state is responsible for the parallel magnetization. A small excess of protons will spin in the lower energy state. This small excess leads to a small, but measurable, magnetization parallel to B_0 (M_0) [7,15]. The magnitude of this magnetization can be calculated from

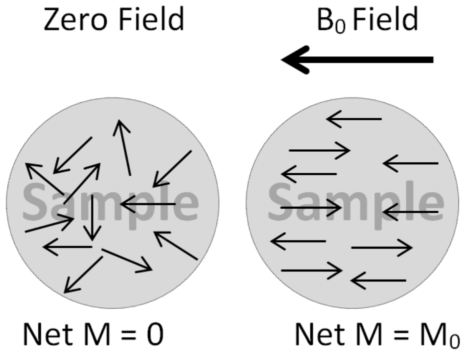

Figure 2: When an imaging sample is placed in a strong magnetic field, the nuclear magnetic moments align parallel and anti-parallel. An excess of spins in the parallel direction create a magnetization M_0 parallel to B_0.

$$M_0 = \frac{n\hbar^2\gamma^2 I(I+1)}{3kT} B_0 \tag{2}$$

where k is the Boltzmann constant ($k = 1.38 \times 10^{-23}$ J/K), T is temperature (in Kelvin, K) of the imaging sample, I is spin (for hydrogen, $I = 1/2$), n is the total number of spins, and $\hbar = h/2\pi$ where h is Planck's constant ($h = 6.63 \times 10^{-34}$ J s) [15].

The greater the net magnetization, the greater the signal that can be obtained from a sample. More signal produces better images and/or allows for faster image acquisition. The most practical way to increase the net magnetization is to increase the strength of the B_0 field. This is why high field MRI is an area of research interest.

Signal-to-Noise Ratio The signal-to-noise ratio is simply the ratio of the amount of signal to the amount of noise expressed very simply as SNR = S/N. Often, this ratio is expressed in decibels (dB), shown in equation 3.

$$SNR_{dB} = 20\log_{10}\left(\frac{S}{N}\right) = S_{dB} - N_{dB} \tag{3}$$

It's important to understand what influences SNR in order to appreciate the role played by high field MRI. The SNR of an imaging sequence is proportional to acquisition time, image resolution, and magnetic field strength as expressed by

$$SNR \propto M_{xy} V \sqrt{T_{acq}} \tag{4}$$

where M_{xy} is the net magnetization rotated into the transverse plane, V is the voxel size (volumetric pixel), and T_{acq} is the total acquisition time for all data used to reconstruct the MR image [16]. The NMR signal decays according to time constants which are beyond the scope of this thesis. Assuming an image is proton-density weighted (the image contrast is due to the concentration of protons and not different rates of signal decay), then $M_{xy} = M_0$ which means M_0 in equation 2 can be substituted for M_{xy} in equation 4 to yield

$$SNR \propto \frac{n\hbar^2\gamma^2 I(I+1)}{3kT} B_0 V \sqrt{T_{acq}} \tag{5}$$

Given proton imaging, the spin (I) and gyromagnetic ratio (γ) are set. The number of spins (n) is determined by the imaging sample. Therefore, the only quantities that can be varied are temperature (T), field strength (B_0), voxel size (V), and acquisition time (T_{acq}). In human MRI, temperature of our sample cannot be reduced and is determined by the temperature of the human body. By increasing the acquisition time in an MRI experiment, the patient is put at greater discomfort and the cost of MRI increases. Either resolution must be sacrificed by increasing voxel size, or field strength must be increased in order to obtain greater SNR while minimizing patient discomfort and MRI cost.

1.4.2 The B_1 Field

As discussed in §1.3, the net magnetization created in an imaging sample by the B_0 field must be tipped by exciting the proton spins with a rotating magnetic field. Since the magnetization points parallel to the B_0 field and is the axis of precession for the magnetic moments, it is impossible to measure the magnitude of magnetization of the protons as there is no variation of magnetic flux (which would be required to induce an *emf* in a wire loop and measure a signal). To measure the magnetization, it must be rotated perpendicular to the B_0 field (into the transverse XY plane) in order to be measured. This is done by applying a torque to the magnetization vector. This is accomplished using a second magnetic field, B_1, which is perpendicular to B_0. In order to apply a torque large enough to rotate the magnetization into the transverse plane, this field must be time-varying and resonate at the Larmor frequency [7]. This time-varying, resonant B_1 field is created by passing a radio frequency pulse through a loop or coil of wire. Ampere's law describes the relationship between current and magnetic field. The radio frequency pulse used for excitation is at the same frequency at which the proton spins resonate. This is called the Larmor frequency which is expressed in terms of B_0 and is identical to equation 1.

$$f_0 = \bar{\gamma} B_0 \quad [\text{MHz}] \tag{6}$$

$$\omega_0 = \gamma B_0 \quad [\text{rad/s}] \tag{7}$$

$$\bar{\gamma} = \gamma / 2\pi$$

$$\gamma(^1\text{H}) = 267.5 \times 10^6 \text{ rad/T/s} \qquad \bar{\gamma}(^1\text{H}) = 42.58 \text{ MHz/T [7]}$$

The loop or coil of wire through which the RF pulse passes to generate the B_1 field must also resonate at the Larmor frequency. These coils are referred to as RF coils and are used to generate the B_1 field as well as receive the signal which is induced by the rotating magnetization vector [9, pg. 1-21].

Flip Angle Flip angle is the name given to the angle by which the magnetization (M_0) is flipped out of the Z-axis by an RF pulse. The degree of flip imparted can be varied by increasing the amplitude (B_1) or duration (τ) of the RF pulse (and hence, the B_1 field) [7, 10]. Flip angle (θ), in degrees, can be calculated by taking the integral of B_1 over time,

$$\theta = \left(\frac{180^\circ}{\pi}\right) \gamma \int_0^\tau B_1 \mathrm{d}t$$

or for a rectangular pulse [7],

$$\theta = \left(\frac{180^\circ}{\pi}\right) \gamma B_1 \tau$$

The signal intensity (I) of any given voxel of an image is related to the transverse component of the magnetization which is expressed as $I = M_0 \sin(\theta)$ [7]. To achieve even brightness and contrast throughout an image, the entire sample must experience the same flip angle so that the intensity of any one voxel is related to the spin density of the voxel rather than the B_1 field in the voxel. In order to flip the magnetization of the entire sample equally, the B_1 field must be homogeneous. A solenoid can be used to create a homogeneous field, however patient access is problematic due to the orientation of the solenoid perpendicular to the magnet bore. Field homogeneity throughout a sample volume is achieved through use of a variety of so-called volume coils. As a result of this homogeneity, a volume coil often has a large field-of-view (FOV) useful for imaging large objects. Due to the characteristics of volume coils, they frequently trade SNR for FOV and homogeneity. For this reason, a volume coil is often used to transmit the RF pulse.

If, instead, sensitivity is desired over a smaller FOV, a simple loop of wire may be used. A loop of wire positioned against the skin of a human subject, or surface of an imaging phantom, is referred to simply as a surface coil. Because of the reduced FOV, often these loops are used in large arrays known as receive arrays, surface arrays, or phased arrays. Due to their inhomogeneous B_1 field profile but high sensitivity, they are used primarily to receive the RF produced by the imaging sample [17].

High Field MRI High field MRI systems, such as the Varian 4.7 T available at the Peter S. Allen MR Research Centre, produce better SNR and higher resolution images than clinical systems 1.5 T (and now 3.0 T) systems [16, 18]. One of the drawbacks, however, is the radio frequency (RF) wavelength associated with the Larmor frequency at high field. When the RF wavelength is short enough to be comparable to human anatomy, there are B_1 field homogeneity effects [19].

In high field MRI, B_1 homogeneity becomes a challenge since the Larmor frequency increases in proportion to B_0 field strength. While homogeneity does not pose a significant challenge at a standard clinical field strength of 1.5 T, at field strengths of 3 T or greater, field homogeneity poses a greater concern.

To understand the reason behind this inhomogeneity, it is important to note that as Larmor frequency (f_0) increases, wavelength (λ) decreases. This wavelength, in free space, can be calculated from:

$$\lambda = \frac{c}{f} \tag{8}$$

where c is the speed of light. Furthermore, the speed of light can be written in terms of permittivity (ϵ) and permeability (μ):

$$c = \frac{1}{\sqrt{\mu\epsilon}} \tag{9}$$

This allows wavelength to be expressed in terms of permittivity:

$$\lambda = \frac{1}{f\sqrt{\mu\epsilon}} \tag{10}$$

Frequency of an electromagnetic (EM) wave remains constant across dielectric boundaries. Keeping this in mind, equation 9 can be written in terms of different dielectrics and frequency can be equated to yield,

$$\lambda\sqrt{\mu\epsilon} = \lambda_0\sqrt{\mu_0\epsilon_0} \tag{11}$$

where subscript *0* indicates free space quantities. For materials that are not ferromagnetic (diamagnetic or paramagnetic) it can generally be approximated that μ=μ_0 [20]. Dielectric permittivity (ϵ) is related to permittivity of free space (ϵ_0) by the relative permittivity (ϵ_r) according to $\epsilon = \epsilon_r\epsilon_0$. Equation 11 can then be rearranged to yield the following relationship between wavelength and relative permittivity:

$$\lambda = \frac{\lambda_0}{\sqrt{\epsilon_r}} \tag{12}$$

In an NMR sample, the relative permittivity is usually large enough to reduce the wavelength in high field MRI to a scale comparable to human anatomy. For example, at 4.7 T the Larmor frequency is 200 MHz and the wavelength in free space is 1.5 meters. Water has an ϵ_r of 81 [20] with a resulting wavelength of 16.7 cm inside a water phantom. Because H_2O is a polar molecule, it is strongly polarized in an electric field and hence its relative permittivity is very high [20]. Since the human body is composed largely of water, the wavelength in the human body is only slightly longer than in pure water (17 - 22 cm in the human head). This is on the same order of magnitude as human anatomy and many MRI phantoms.

When the dielectric effect on wavelength is considered, the quasi-static analysis usually performed on RF coils, such as use of the Biot-Savart Law [21], is no longer valid to accurately model the B_1 field [22]. This sort of analysis is only valid for wavelenths much larger than the imaging sample. The short wavelength at high field of the B_1 field within the imaging sample results in a magnetic field that varies with position in the imaging sample. Because of the wave-like behaviour of the B_1 field in high field MRI, the B_1 field becomes susceptible to constructive and destructive interference within the NMR sample which results in bright and dark regions in an MRI image not indicative of the structure or anatomy of the imaging sample [4,19,22,23].

1.5 RF Circuit Concepts

For those who are unfamiliar with the basics of RF circuit design and the associated mathematical concepts and terminology, this section attempts to briefly cover concepts of impedance, admittance, transmission line equations and impedance transformations, S-parameters, reflection coefficients, and the Smith Chart. This is necessary before any discussion on RF hardware from an electrical engineering perspective.

1.5.1 Impedance and Admittance

Impedance (Z), units in ohms (Ω), is a complex-valued quantity to describe the amount of resistance and capacitance or inductance that is presented by a circuit, circuit component, etc. It's expressed as

$$Z = R + \jmath X \quad [\Omega]$$

where R is resistance and X is reactance. Reactance can be calculated from capacitance (C) or inductance (L).

$$X = \begin{cases} \omega L, & \text{inductive reactance.} \\ -\frac{1}{\omega C}, & \text{capacitive reactance.} \end{cases}$$

The admittance (Y) is the reciprocal of impedance, $Y = 1/Z$, with units in siemens (S) and is expressed as

$$Y = G + \jmath B = \frac{1}{R + \jmath X} \quad [\text{S}]$$

where G is conductance and B is susceptance which can be calculated from capacitance or inductance.

$$B = \begin{cases} \omega C, & \text{capacitive susceptance.} \\ -\frac{1}{\omega L}, & \text{inductive susceptance.} \end{cases}$$

1.5.2 Transmission Line Theory

The equations needed to understand radio frequency circuits are more complicated than those needed to understand direct current (DC) and alternating current (AC) circuits. This is because at radio-frequencies, the wavelength of the electrical signals is not much larger than the circuit elements including the copper traces and cables connecting devices. For low frequency circuits, it can be assumed that for a given span of line or copper trace, the voltage or current is constant across it because the wavelength of the signal is much larger than the circuit element [24]. In order to analyze radio frequency circuits, it becomes necessary to use transmission line circuits which were first used in power system analysis due to the long stretches of transmission lines which begin to approach the wavelength of AC power [25].

By assuming that an incremental length of transmission line (a generic term to refer to anything from a power line to a copper trace of a circuit board) contains a certain amount of series resistance (R), series inductance (L), shunt conductance (G), and shunt capacitance (C), the characteristic impedance (Z_0) of the transmission line can be calculated from these per-unit-length quantities using

$$Z_0 = \sqrt{\frac{\jmath \omega L + R}{\jmath \omega C + G}}. \tag{13}$$

For an RF system, this characteristic impedance is typically 50 Ω. In all practical cases, the resistance and conductance can be assumed to be negligible (R, $G = 0$) and the line becomes a lossless transmission line ($Z_0 = \sqrt{L/C}$). The voltage (equation 14) and current (equation 15) at some point (z) along a transmission line can be expressed in terms of the forward and reverse traveling voltage amplitudes (V^+ and V^-), the characteristic impedance (which relates voltage to current) and a complex exponential described by the propagation constant (γ, not to be confused with the gyromagnetic constant) and position (z) which represents the wave nature of the voltage and current [24].

$$V(z) = V^+ e^{-\gamma z} + V^- e^{\gamma z} \tag{14}$$

$$I(z) = \frac{V^+}{Z_0} e^{-\gamma z} - \frac{V^-}{Z_0} e^{\gamma z} \tag{15}$$

The propagation constant, like the characteristic impedance, can be defined using the same parameters present in equation 13 [24].

$$\gamma = \sqrt{(R + \jmath\omega L)(G + \jmath\omega C)}$$

For the lossless case $\gamma = \jmath\omega\sqrt{LC}$ and it is helpful to define the propagation constant in terms of a real-valued constant as follows: $\gamma = \jmath\beta$. It's also helpful to note that the wavelength (λ) in the transmission line can be expressed as $\lambda = 2\pi/\beta$ [26].

These equations and quantities can then be used to describe the impedance transforming properties of transmission lines which is a powerful tool in RF circuit design. Equation 16 describes the input impedance (Z_{in}) of a length of transmission line (ℓ) which is terminated at the opposite end by some load resistance (Z_L).

$$Z_{in} = Z_0 \frac{Z_L + jZ_0 \tan(\beta\ell)}{Z_0 + jZ_L \tan(\beta\ell)} \tag{16}$$

From this, some interesting observations can be made which prove useful. Any length of transmission line that is an integer multiple of half of the wavelength ($\ell = N\lambda/2$, $N \in \mathbb{Z}$) of the RF wave will not transform the load impedance. For a quarter-wavelength ($\lambda/4$) transmission line [27], equation 16 reduces to

$$Z_{in} = \frac{Z_0^2}{Z_L}$$

If the load impedance is an open circuit ($Z_L = \infty$), then the input impedance (Z_{in}) becomes zero (short circuit). If, on the other hand, the load impedance is a short circuit ($Z_L = 0$), the input impedance looks like an open circuit instead. Finally, if the load impedance is the same as the characteristic impedance, then the input impedance is simply the characteristic impedance. In fact, this holds true for any transmission line length, not only quarter-wavelength lines.

1.5.3 S-parameters

Scattering (S) parameters describe how energy delivered to one port of a device is scattered to all ports of the device. This is used to describe characteristics of an RF circuit. The proportion of power delivered to port j as a result of incident power at port i is described by the parameter S_{ji}. The proportion of power reflected at the incident port is described, likewise, by parameter S_{ii}. An N-port device will have N^2 S-parameters [24].

Two-Port Device The most common device dealt with in MRI RF hardware is a two port device which has one input, and one output (or simply two ports, regardless of the port's purpose). This applies to RF LNAs (low noise amplifiers), two-port birdcage or surface coils, lengths of coaxial cable, etc. For a two port device, the S-parameter matrix is expressed as

$$S = \begin{bmatrix} S_{11} & S_{12} \\ S_{21} & S_{22} \end{bmatrix}$$

where S_{11} and S_{22} are the input and output reflection coefficients (Γ_{in} and Γ_{out}), respectively (when the opposite port is terminated by 50 Ω). The forward gain (or attenuation) of the device is expressed by $|S_{21}|$ and the reverse gain is expressed by $|S_{12}|$. Similar concepts extend to devices where the number of ports is larger ($N > 2$) [24].

1.5.4 Reflection Coefficients

Reflection coefficients express the amount of power that is reflected when a traveling wave passes a boundary. While in general electromagnetics, this boundary can be where two different dielectrics meet, in RF circuits this boundary is usually a change in circuit impedance. By characterizing the input impedance of an electronic device, it's possible to calculate the amount of RF power reflected when a wave is incident on the device's input. By assuming that the device is connected to a transmission line with a 50 Ω characteristic impedance (Z_0), and the load impedance is the input impedance of the device (Z_L) the following equation can be used to obtain the reflection coefficient [24, 27],

$$\Gamma = \frac{Z_L - Z_0}{Z_L + Z_0}$$

The more poorly matched the load impedance is to the characteristic impedance, the greater the reflection coefficient is. The reflection coefficient is zero for a perfectly matched load impedance. The reflection coefficient can also be calculated directly from S-parameters. This is convenient since S-parameters are easily measured on a vector network analyzer and specified in datasheets for many off-the-shelf devices. Usually the S_{nn} parameters of an N-port device ($1 \leq n \leq N$), for example S_{11} or S_{22} of a two-port device, are roughly equivalent to the reflection coefficient if all other ports of the device are terminated by the characteristic impedance, 50 Ω. This is because S-parameter measurements are conducted with the device ports attached to matched ports of the network analyzer. If, however, the port(s) not being measured is terminated by an unmatched load, then the reflection coefficient is not equal to these S-parameters.

1.5.5 Smith Chart

The Smith chart provides a convenient way to represent S-parameters, impedances (Z), admittances (Y), and reflection coefficients (Γ). It is an extremely useful aid in designing matching networks and tuned circuits. The Smith chart is a polar plot of reflection coefficients, where the origin represents $\Gamma = 0$. The limits of the polar plot lie on a unit circle at $|\Gamma| = 1$. This is the limit of the Smith chart [27]. In the same way, S-parameters can be plotted on the Smith chart where zero is at the centre of the plot and unity is on the edge of the plot. Quantities can be plotted as phasors (magnitude and angle) or as a complex number in Cartesian coordinates where the horizontal axis is real and vertical axis is imaginary. The second way to use the Smith chart is to plot impedances or admittances to it. These values must be normalized. An impedance (Z) can be scaled by the characteristic impedance,

$$z = r + \jmath x = \frac{Z_L}{Z_0}$$

and then mapped to the Smith chart by using circles of constant resistance (r, shown as blue solid lines in figure 3) and curves (circles in actuality) of constant reactance (x, dashed blue in figure 3), which can also be expressed as a reflection coefficient [27],

$$\Gamma = \frac{Z_L - Z_0}{Z_L + Z_0} = \frac{z-1}{z+1}$$

Likewise, admittances can be scaled by the characteristic admittance (Y_0, normally 20 mS),

$$y = g + \jmath b = \frac{Y_L}{Y_0}$$

and then mapped to the Smith Chart using circles of constant conductance (g, dotted red in figure 3) and curves of constant susceptance (b, dash-dotted red in figure 3).

$$\Gamma = \frac{Y_0 - Y_L}{Y_0 + Y_L} = \frac{1-y}{1+y}$$

The classical Smith chart is an impedance chart. Any impedance Smith chart can be rotated 180° to get an admittance chart. Then, any mapped impedance can be rotated about the centre of the rotated polar chart 180° to find its admittance [24]. Figure 3 is a combination impedance and admittance chart, for convenience.

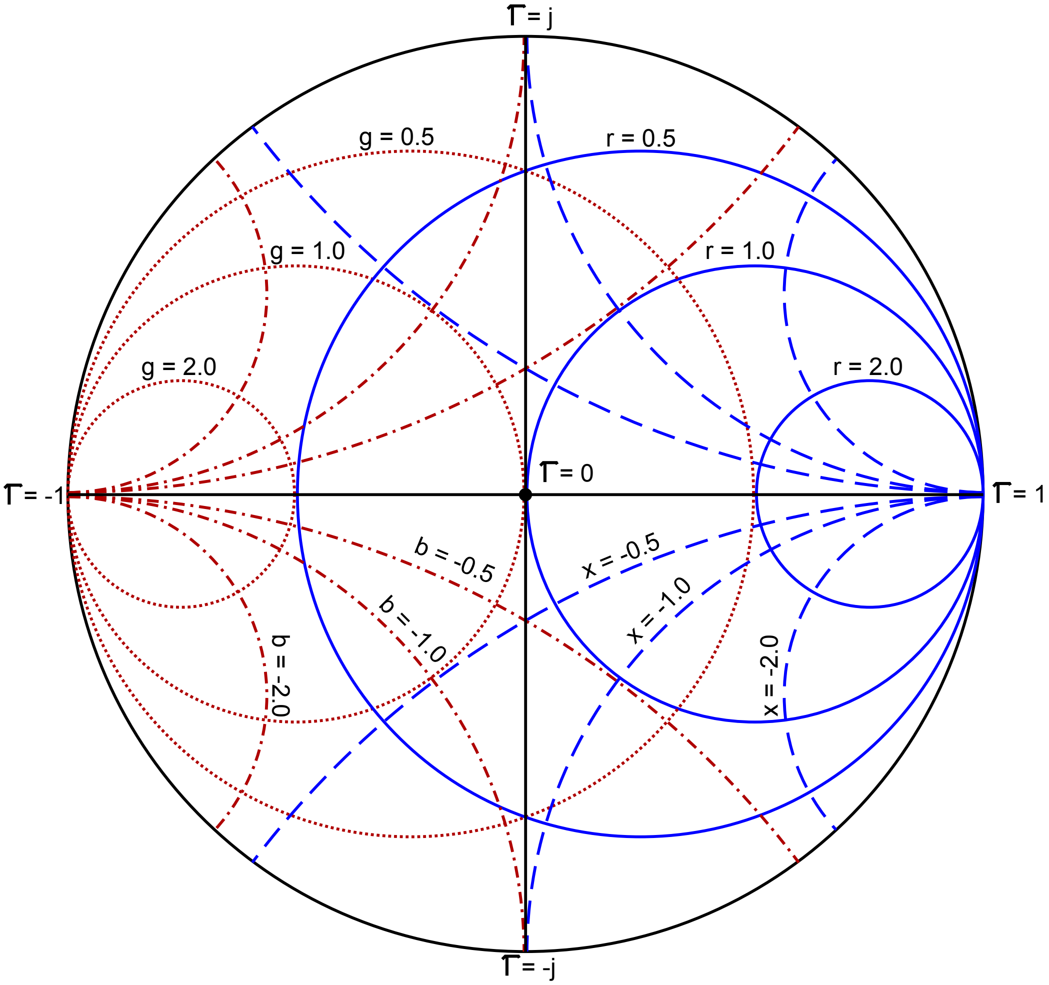

Figure 3: The Smith Chart with the admittance chart superimposed. The impedance chart (classical Smith Chart) is composed of constant resistance circles (r, in solid blue) and constant reactance curves (x, in dashed blue). The admittance chart is composed of constant conductance circles (g, dash-dot red) and constant susceptance curves (b, dotted red).

1.6 MRI RF Hardware

The RF hardware chain is pictured in figure 4. The entire RF chain continues to be a focus of research and development in an effort to further improve MRI. This thesis, focused on RF hardware, specifically focuses on RF coils (transmit and receive) and the RF circuits immediately upstream (for transmit) and downstream (for receive) of these coils.

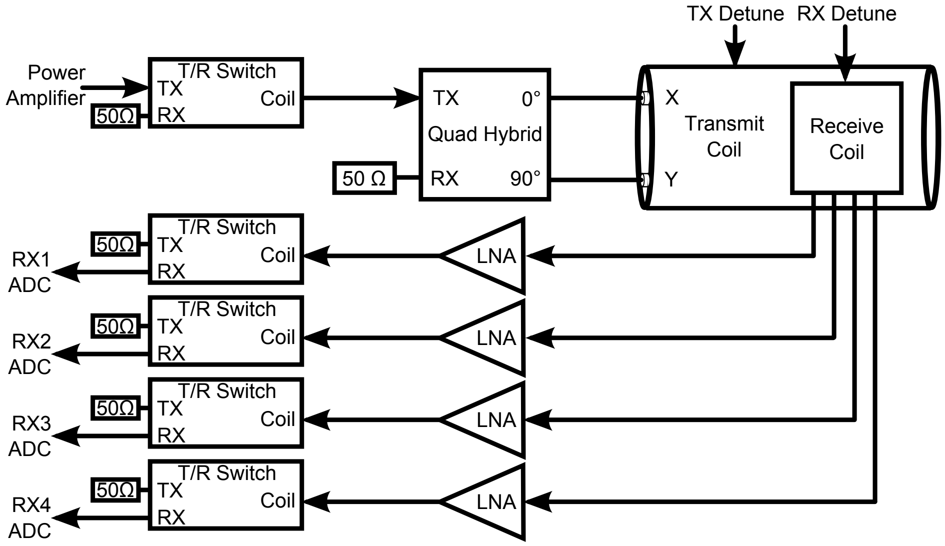

Figure 4: Block diagram of a one transmit and four receive channel with a quadrature driven transmit RF coil and separate four-channel receive RF coil.

1.6.1 RF Coils

There are a wide variety of RF coils used in MRI. These fall into two very broad categories: surface coils and volume coils. A surface coil gets its name because it is usually positioned against the surface of the imaging sample and generates a B_1 field near the coil at the surface of the imaging sample. A volume coil is named because it usually is positioned around the entire sample and produces a B_1 field throughout the volume of the coil. The focus of this work is primarily on transmit volume coils and the receive chain downstream from receive surface coils.

1.6.2 Surface Coils

Surface coils are made of a simple loop of wire and tuned to the Larmor frequency (f_0) with a shunt capacitor for tuning (C_t) according to $f_0 = 1/2\pi\sqrt{LC_t}$. It is common practice to match the coil input impedance to the characteristic impedance of the coaxial cable and RF system (50 Ω) to which the coil is connected using a matching capacitor (C_m) [9, pg. 437-491]. Because it is becoming more common to place low-noise amplifiers (called preamplifiers in MRI when referring to the first stage device) immediately on the coil elements, a more effective strategy is to match the coil to the optimum impedance of the low-noise preamplifier used to amplify the NMR signal, rather than match to the characteristic impedance (see §2). This alternative strategy minimizes the noise introduced to the signal by the amplifier.

As frequency and/or loop size increases, loops must be partitioned into multiple sections (with an electrical length less than $\lambda/20$) with coupling capacitors to keep copper sections impedances in check and prevent self-resonance [9, pg. 437-491].

Large arrays of coils can be constructed as long as the coupling between individual loops is eliminated. This has historically been done using two strategies. The first is to physically decouple the coils via overlapping of the coils, capacitive tuning, or inductive tuning. Second, a low input impedance preamplifier is used to decouple non-neighboring coils (which cannot be physically decoupled) by minimizing the current that flows in the coil, hence minimizing coupling [28].

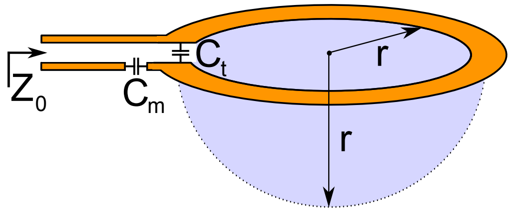

Figure 5: A simple copper loop used as a surface coil with tuning (C_t) and matching (C_m) capacitors. The blue area beneath the coil is the area of best sensitivity (technically, the coil is sensitive above as well).

Surface coils produce a heterogeneous B_1 field. As a result, when used for transmit, they produce a wide range of flip angles. For this reason, surface coils are not typically the best choice for transmit if a homogeneous B_1 field is desired. In the role of a receive coil, a surface coil provides a small region-of-interest (ROI) but a high SNR within this region. Typically, for a surface coil of radius r, the best sensitivity is seen at distances within r of the coil plane (figure 5) [9, pg. 437-491].

1.6.3 The Birdcage RF Coil

In order to create a perfectly homogeneous, time-varying magnetic field a metallic sphere with sinusoidal current distribution may be used. Alternatively, an infinitely long cylinder with a sinusoidal current distribution may be used [17]. Since neither of these options is possible nor practical for real world use (especially in human MRI) the characteristics of these options must be mimicked using a more practical implementation. The most common implementation of the cylinder with sinusoidal current distribution, and most common form of volume coil, is the birdcage RF coil (figure 6b). Named for its appearance, the birdcage RF coil is a ladder transmission line (figure 6a) wrapped into a cylinder such that the end of the ladder transmission line connects back to the beginning. The electrical length of the line is equal to one wavelength at the Larmor frequency, hence each end-ring of the cylinder has an electrical length of one wavelength and can support a standing wave cosine current distribution along its structure [9]. Capacitance usually comes

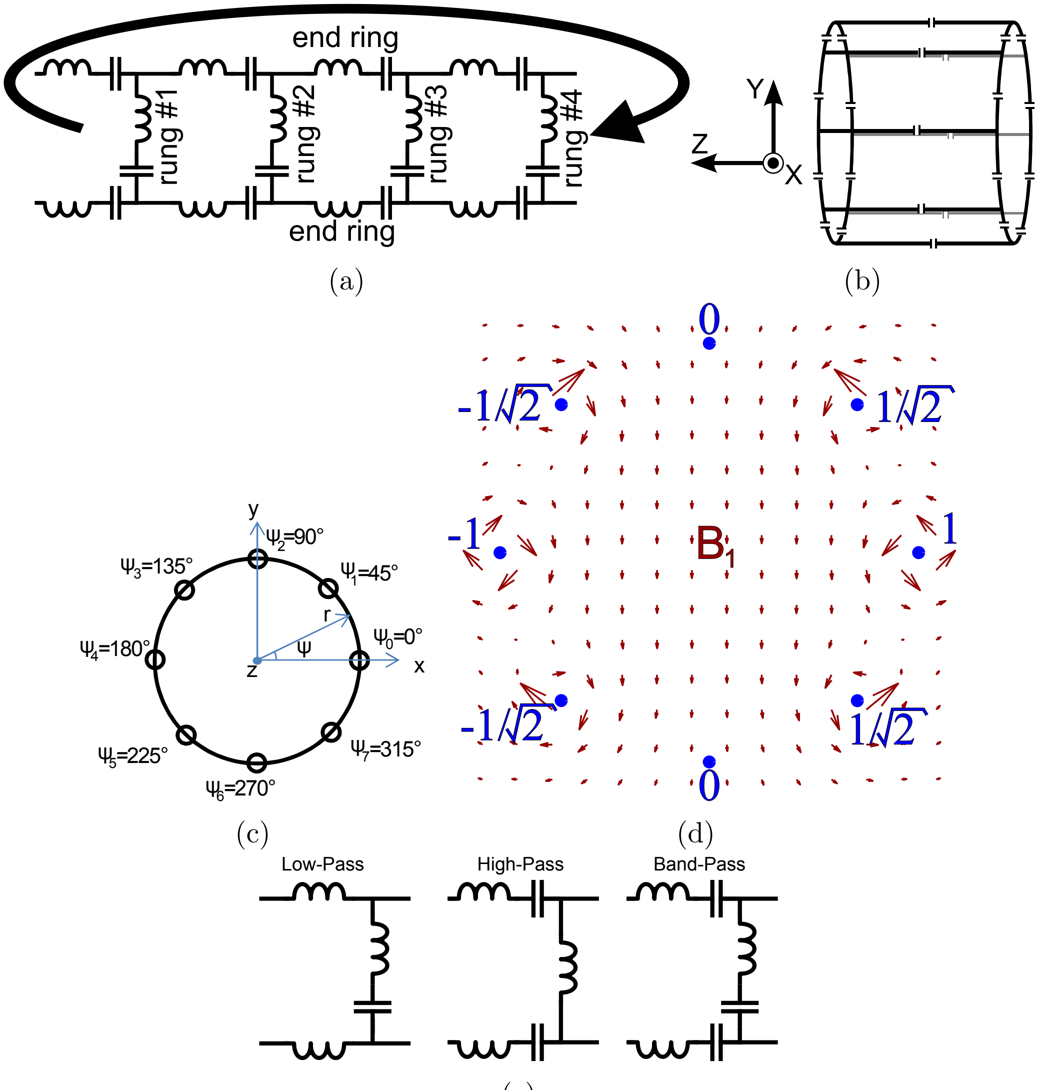

(a) (b) (c) (d) (e)

Figure 6: (a) A four-rung example of a ladder transmission line (one wavelength in electrical length), which when wrapped about a cylinder such that the start of the line is connected to the end (as indicated by the arrow), becomes a birdcage RF coil. (b) Side view of an 8-rung band-pass birdcage RF coil. Capacitors are shown. Inductance is due to copper lengths and mutual inductance. (c) One example of rung positioning about the end ring of an 8-rung birdcage coil. (d) A cross-sectional view of the homogeneous B_1 field caused by the sinusoidal current distribution (normalized current magnitude) on an 8-rung birdcage coil, calculated via the Biot-Savarts law. (e) Circuit schematics for one rung and section of end rings on the low-pass, high-pass, and band-pass birdcage coil designs. Inductance is as a result of the copper rungs and end-rings as well as mutual inductance between these structures, and the capacitors are usually high-voltage high-Q chip-capacitors in the picofarad range.

from lumped components: high-Q chip capacitors. Inductance comes from both self inductance of each element and the significant amount of mutual inductance between the various elements on the birdcage coil. [9]

The rungs of the ladder transmission line connect the two end rings. Rungs are spaced evenly about the cylindrical structure (figure 6c). The angular separation, in degrees, for an N-rung birdcage coil is simply $\Delta\psi = 360°/N$. Since the objective is to simulate an infinitely long cylinder with sinusoidal current distribution, each rung must have close to uniform current density along its length. The electrical length of each rung is kept shorter than $\lambda/20$. In order to ensure this, at higher frequencies, rungs will often be partitioned using capacitors. Based on the arrangement of capacitors in the transmission line, three types of coils can be constructed: Low pass, band-pass, and high pass coils (figure 6e) [9].

It's important to understand the nature of the B_1 field produced by a birdcage coil. This starts by understanding the current distribution. The sinusoidal current distribution can be expressed mathematically. The current (I_n) on the n^{th} rung at a position ψ_n on the birdcage relative to a port at position $\psi = 0°$ which is driving the coil, can be expressed as a function of frequency (f_0), time (t), phase (ϕ), and driving current (I_p):

$$I_n = I_p \cos(2\pi f_0 t + \phi)\cos(\psi_n) \tag{17}$$

The Biot-Savarts Law can be applied to each rung of the birdcage coil (as well as the end rings, however their influence is small enough to ignore for now since it's more important to get an intuitive understanding of the B_1 field) and the superposition of the magnetic fields from all of the rungs in the birdcage coil make up the net field which is the B_1 field. For a current distribution in which the rung on the positive X-axis ($\psi_0 = 0°$) has current $I_0 = I_p$ with all other rungs having current according to equation 17, the magnetic field components along the X-axis cancel out due to the symmetry about the Y-axis of the current distribution. The resultant magnetic field points along the negative Y-axis, hence B_1 is along the axis perpendicular to the rung with peak positive and negative currents. Simulating this field with the current distribution described by equation 17 produces a B_1 field as shown in (figure 6d).

1.6.4 Quadrature Drive

While a single port may be used to feed RF power to the coil and excite proton spins, this option results in a linearly driven coil. The rungs have sinusoidal current distribution and only the magnitude of the B_1 field along a single axis varies. Examining equation 17 in §1.6.3, it's apparent that rungs at $\psi = \pm 90°$ are always at zero current and never contribute to the B_1 field. The B_1 field oscillates in a single axis only (the Y-axis). This linear polarization can be represented using two vectors rotating in opposite directions (figure 7a). Only one of these vector components will excite proton spins (the clockwise rotating component relative to the B_0 field, the left-hand rule [7]), hence linear polarization only achieves 50% efficiency as the other vector component is wasted energy. For this reason, two-port quadrature-driven coils have been developed. In the case of a quadrature driven birdcage coil, two ports are located at points along the ladder network separated physically by 90° so the current distribution equation 17 is shifted by this 90°.

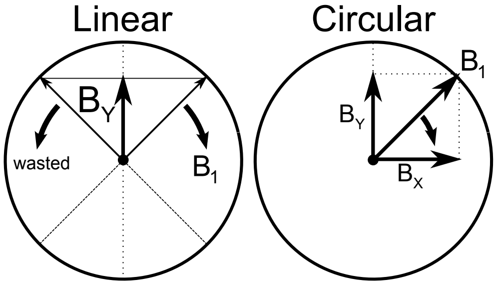

(a) (b)

Figure 7: (a) A linearly polarized coil represented by a growing and shrinking vertical vector, which can be broken down into two vectors rotating in opposite directions. (b) A circularly polarized coil represented by a single rotating vector. Vectors are viewed from the +Z-axis (magnetization, M_0, pointing out of the page).

As established in §1.6.3, a port on the positive X-axis creates a B_1 field pointing along the negative Y-axis. Therefore, a second port lies on the positive Y-axis (at +90°) and creates a B_1 field pointing along the positive X-axis. In order to create a circularly rotating field, the RF pulses which excite each port and create each field must be separated by 90° in phase. The field along the Y-axis is denoted B_Y and that along the X-axis is denoted B_X. The magnitude of the field is related to the current through a scaling factor, V,

$$\overrightarrow{\mathbf{B_X}} = V I_p \cos(2\pi f_0 t + \phi_X)\hat{\mathbf{x}} \tag{18}$$

$$\overrightarrow{\mathbf{B_Y}} = -V I_p \sin(2\pi f_0 t + \phi_Y)\hat{\mathbf{y}} \tag{19}$$

where ϕ_X and ϕ_Y are phase offsets of the RF pulse (a 90° phase delay on B_Y is already assumed in the equation). To obtain the circularly rotating B_1 field, the B_X and B_Y fields can be combined. Since B_X has no phase delay, the port driving this field is referred to as the in-phase port. The B_Y field is phase delayed by 90° and its port is therefore referred to as the quadrature port. The phase offsets (ϕ_X and ϕ_Y) can be assumed to be zero, however these can be changed to achieve elliptical field polarization, or even linear polarization using two ports. The resultant circularly polarized B_1 field can be described by,

$$\overrightarrow{\mathbf{B_1}} = V I_p \{\cos(2\pi f_0 t)\hat{\mathbf{x}} - \sin(2\pi f_0 t)\hat{\mathbf{y}}\} \tag{20}$$

Equation 20 describes a single, clockwise rotating vector (figure 7b) of the B_1

field created by a quadrature-driven, circularly polarized birdcage coil. Each port may be driven with half the power of a linearly driven coil's port. While the total power supplied will be the same, there is a $\sqrt{2}$ increase in excitation to the protons and SNR, which means the RF pulse amplitude or duration may be decreased to achieve an identical flip angle [9, pg. 131-186] [4]. The power efficiency was found to decrease somewhat for imaging samples that were not symmetric and instead had an elliptical cross-section [4].

1.6.5 Quadrature Hybrid Coupler

In order to drive a quadrature birdcage coil using a single transmit channel, the RF power must be evenly split between the two-port coil, and a 90° phase shift must be introduced to one port. Both of these requirements are met by a piece of hardware called a quadrature hybrid coupler (figure 8). This device has four ports. An input/transmit (In/TX), isolation/receive (Iso/RX), in-phase (I / 0°), and quadrature (Q / 90°) port. The transmit signal is split evenly at each of the output ports (I and Q) with a phase shift between the ports of 90°.

A quadrature hybrid can be constructed a variety of ways, however the branchline coupler will be described here. The branchline coupler (figure 8) is constructed with a network of microstrips, striplines, coaxial lines, or lumped elements (though lumped element designs suffer from narrow operating bandwidth) [29]. In the microstrip design, four quarter wavelength ($\lambda/4$) microstrips are connected in a square where each port is located at each corner of the square structure [29]. The microstrip impedance is chosen such that all ports are matched to 50 Ω. This means that the shunted microstrips (those connecting the transmit to receive and the in-phase to quadrature port) have the characteristic impedance of 50 Ω. Meanwhile, the series microstrips (connecting the transmit to the in-phase port and receive to quadrature port) have an impedance of $1/\sqrt{2}$ the characteristic impedance (35.4 Ω for a system with a 50 Ω characteristic impedance) [9, pg. 131-186], [30].

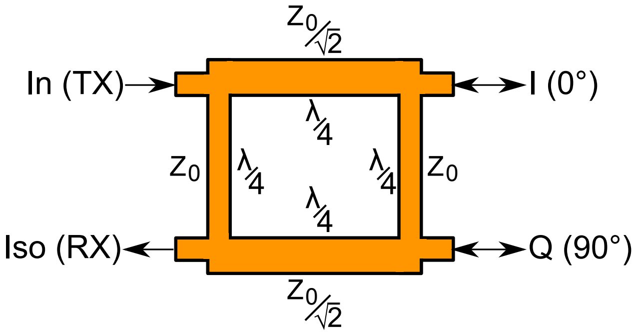

Figure 8: Schematic of a transmission line (stripline or microstrip) branchline coupler designed as a quadrature hybrid. The RF signal (RF) to the transmit (TX) port is split evenly ($RF/\sqrt{2}$) to the in-phase, I (no phase delay), and quadrature, Q (90° phase delay). Signals from I and Q are recombined at the receive port (RX).

The S-parameter S_{QT} describes the proportion of power transmitted from the transmit (T) port to the quadrature (Q) port. The S-parameter S_{IT} describes the amount of power coupled from the transmit port to the in-phase (I) port. Ideally, no power is transmitted from the transmit to the receive (R) port (S_{RT}) [30]. The S-parameter matrix for the ideal quadrature hybrid is shown below, where ports are termed: transmit/input, T; receive/isolation, R; in-phase, I; and quadrature, Q.

$$S = \begin{bmatrix} S_{TT} & S_{TR} & S_{TI} & S_{TQ} \\ S_{RT} & S_{RR} & S_{RI} & S_{RQ} \\ S_{IT} & S_{IR} & S_{II} & S_{IQ} \\ S_{QT} & S_{QR} & S_{QI} & S_{QQ} \end{bmatrix} = \begin{bmatrix} 0 & 0 & \frac{e^{-j\pi/2}}{\sqrt{2}} & \frac{e^{-j\pi}}{\sqrt{2}} \\ 0 & 0 & \frac{e^{-j\pi}}{\sqrt{2}} & \frac{e^{-j\pi/2}}{\sqrt{2}} \\ \frac{e^{-j\pi/2}}{\sqrt{2}} & \frac{e^{-j\pi}}{\sqrt{2}} & 0 & 0 \\ \frac{e^{-j\pi}}{\sqrt{2}} & \frac{e^{-j\pi/2}}{\sqrt{2}} & 0 & 0 \end{bmatrix}$$

2 Noise Figure of MRI Preamplifiers

2.1 Summary

A noise figure and noise parameter measurement system was developed which consists of a combination spectrum and network analyzer, preamplifier, programmable power supply, noise source, tuning board, and desktop computer. The system uses the Y-factor method for noise figure calculation and allows calibrations to correct for loss of excess noise ratio between the noise source and device under test, second stage (system) noise, ambient temperature variations, and available gain of the device under test. Noise parameters are extracted by performing noise figure measurements at several source impedance values obtained by setting control voltages in the tuner. Results for several amplifiers agree with independent measurements and with the corresponding datasheets.

With some modifications the system was also used to characterize the noise figure of MRI preamplifiers in strong static magnetic fields up to 9.4 T. In most amplifiers tested the gain was found to be reduced by the magnetic field, while the noise figure increased. These changes are detrimental to signal quality and are related to the electron mobility and configuration of the amplifiers semiconductor devices. Consequently, gallium arsenide (GaAs) field-effect transistors are most sensitive to magnetic fields due to their high electron mobility and long, narrow channel, while silicon-germanium (SiGe) bipolar transistor amplifiers are largely immune due to their very thin base.

2.2 Introduction

2.2.1 Motivation

Minimizing electrical noise is critical to achieving optimal signal-to-noise ratio (SNR), and thus, image or spectral quality. The amount of noise added by a device such as a preamplifier is described by its noise figure (NF), which can change according to the circuit to which its input is connected as described by the noise parameters [31]. Knowing noise parameters in addition to the scattering or S-parameters is therefore critical in the design of MR coil preamplifiers and the arrays into which they are integrated. Commercial noise figure meters are not found in most MR laboratories due to cost, favoring the indispensable vector network analyzer (VNA) which is used to measure coil tuning and matching. Some VNAs are integrated with a spectrum analyzer, and in this work we show how this combination can be exploited to perform accurate NF measurements. Noise parameter measurements require, additionally, a tuner that can vary the impedance presented at the input of the device under test (DUT). Tuners are part of expensive, specialized systems and are usually designed for frequencies used in the telecommunications industry (900 MHz and above) which are much higher than those used in MR imaging systems. We show that a tuner for MR frequencies is readily built and controlled in conjunction with the combination analyzer to provide automatic noise figure and noise parameter measurements. The strong static magnetic field (B_0) used in MRI is known to affect the performance of preamplifiers through the Hall effect [32–34]. In modern high field systems it is critical to understand how noise figure varies with B_0 field strength since noise figure is known to change as both the strength of the magnetic field and its orientation with respect to the semiconductor device are varied. Noise figure measurements, especially those on low-noise devices, require placing the DUT as close as possible to the instrumentation to minimize measurement errors. The instrumentation, however, cannot be used within the fringe field of an MRI system. Our NF measurement system allows accurate measurements to be performed in the magnet bore while keeping all sensitive equipment outside the 5 gauss line.

2.2.2 Noise Figure Basics

The Y-factor method is a common method of measuring noise figure that uses a noise source with a selectable equivalent noise temperature. The Y-factor is the ratio of the two noise powers at the output of the DUT when at its input the noise source produces hot (N_h) and cold (N_c) noise powers equivalent to a hot (T_h) and a cold (T_c) temperature [31].

$$Y = \frac{N_h}{N_c} \tag{21}$$

Noise temperature, T, relates the available noise power, N_P (e.g. N_h, N_c), produced by a resistor to its temperature (e.g. T_h, T_c) over a given measurement bandwidth, Δf, as

$$N_P = kT\Delta f \tag{22}$$

where k is the Boltzmann constant.

An RF noise source consists of a 50 Ω resistor for which the cold noise temperature (T_c) is often simply ambient room temperature. In order to obtain accurate measurements, the temperature to which the resistor would need to be heated for the hot noise temperature (T_h) is impractically high ($>$ 1000 K). An equivalent hot noise temperature is simulated by reverse biasing a PN diode into avalanche breakdown, thereby injecting additional white noise when connected in parallel with the resistor. The Excess Noise Ratio (ENR) of the noise source expresses the additional noise injected by the diode relative to the standard temperature $T_0 = 290$ K:

$$ENR = \frac{T_h - T_c}{T_0} \tag{23}$$

With an independently calibrated ENR, measured Y-factor, and assuming $T_c = T_0$, the noise factor of a device is expressed as [31]

$$F = \frac{ENR}{Y - 1} \tag{24}$$

Noise figure is the noise factor expressed in decibels (dB), i.e.,

$$NF = 10 \log_{10} F$$

2.2.3 Noise Figure Correction Factors

Because of realities of the measurement system, such as the thermal noise introduced by the system itself, some correction factors are required to accurately calculate the noise figure from the data obtained. If T_c differs from T_0 (a rather cool laboratory temperature of 17° C), the expression for the noise factor in Eq. 24 must be modified to [35, 36]

$$F = \frac{ENR + Y\left(1 - \frac{T_c}{T_0}\right)}{Y - 1} \tag{25}$$

Similarly to Eq. 24, this expression includes all noise created between the noise source and measurement instrument, including noise added by preamplification stages needed to make the measurement instrument sufficiently sensitive to small noise levels. To extract the DUT's noise factor (F_1) from the total F we make use of the Friis formula for cascaded noisy devices, appropriately rearranged [31],

$$F_1 = F - \frac{F_2 - 1}{G_1} \tag{26}$$

where G_1 is the *available* gain of the first stage (DUT). This will correct the measured F to remove the noise contributed by the measurement system (the second stage noise factor, F_2). A separate calibration step is required to measure F_2 by connecting the noise source directly to the input of the measurement system and applying Eq. 25. Available gain, G_a, is calculated from the DUT's S-parameters together with the reflection coefficients at the input and output of the DUT (respectively, Γ_S^D and Γ_O^D, looking in the direction of the noise source) according to [37],

$$G_a = \frac{1 - |\Gamma_S^D|^2}{|1 - S_{11}^D \Gamma_S^D|^2} \frac{|S_{21}^D|^2}{1 - |\Gamma_O^D|^2} \tag{27}$$

$$\Gamma_O^D = S_{22}^D + \frac{S_{12}^D S_{21}^D \Gamma_S^D}{1 - S_{11}^D \Gamma_S^D} \tag{28}$$

$$\Gamma_S^D = S_{22}^{in} + \frac{S_{12}^{in} S_{21}^{in} \Gamma_S^{NS}}{1 - S_{11}^{in} \Gamma_S^{NS}} \tag{29}$$

where S_{ij}^{in} are the S parameters of any device placed between the noise source and DUT, and Γ_S^{NS} is the reflection coefficient of the noise source. When available gain is not available (e.g., when using some dedicated noise figure meters), the insertion gain, G_i, can be used as an approximation since it can be readily calculated from the measured noise powers [37].

$$G_i = \frac{N_h - N_c}{N_{h_2} - N_{c_2}} \tag{30}$$

The approximation can be subsequently corrected by applying the following to the DUT's noise figure (F_1)

$$F_1^{corr} = F_1 + (F_2 - 1)\left(\frac{1}{G_i} - \frac{1}{G_a}\right) \tag{31}$$

A final correction factor is required to account for losses between the noise source and DUT which will cause reductions in the effective ENR seen at the DUT's input. Devices before the input of the DUT are therefore lumped together with the noise source and a new, effective ENR can be obtained by multiplication with the devices' available gain [38],

$$ENR' = ENR\frac{1 - |\Gamma_S^{NS}|^2}{|1 - S_{11}^{in}\Gamma_S^{NS}|^2}\frac{|S_{21}^{in}|^2}{1 - |\Gamma_S^{D}|^2} \tag{32}$$

where the reflection coefficients and S-parameters are those of Eqs. 28 and 29.

2.3 The Noise Figure Measurement System

The measurement system developed for measuring noise figure relies on a combination spectrum and network analyzer (HP4396B, Agilent, USA) with a two-port S-parameter test set (HP85046A). The combination analyzer is controlled via a GPIB bus by a desktop computer running LabVIEW 8.5 (National Instruments, Austin, USA). This graphical software interface (Figure 9) automates the measurement of S-parameters and noise powers, as well as the calculation of correction factors, noise figure, and noise parameters. The greatest advantage of our measurement system over a dedicated noise figure meter is flexibility, since the programming can be altered in any number of ways to suit different circumstances. Additionally, new hardware and correction methods can be integrated into the measurement system as needed to improve the capabilities of the system. For example, the tuner can be inserted into the measurement chain when noise parameters are needed and controlled by activating the corresponding software module. Finally, since the measurement data is sent to a desktop computer for processing, there are no practical limits to the amount of post-processing and number of calculations that can be performed. All raw data can also be permanently saved and later reviewed and re-analyzed.

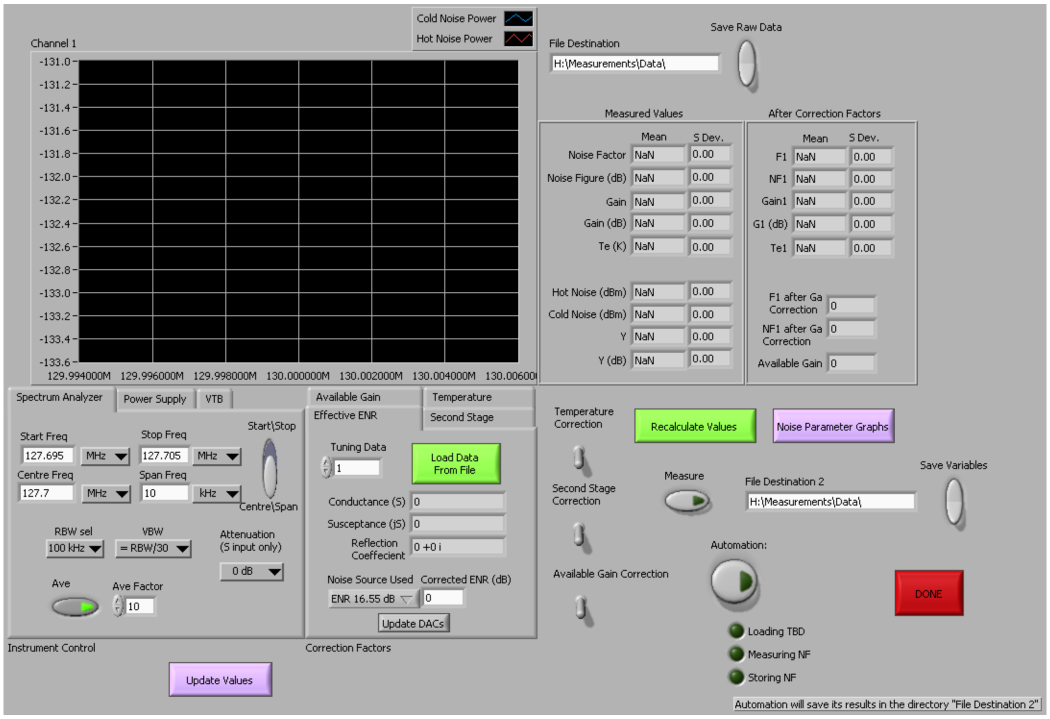

File Destination: H:\Measurements\Data\

Start Freq: 127.695 MHz
Stop Freq: 127.705 MHz
Centre Freq: 127.7 MHz
Span Freq: 10 kHz
RBW sel: 100 kHz
VBW: = RBW/30
Attenuation (S input only): 0 dB
Ave Factor: 10

Tuning Data: 1
Conductance (S): 0
Susceptance (jS): 0
Reflection Coeffecient: 0 +0 i
Noise Source Used: ENR 16.55 dB
Corrected ENR (dB): 0

Measured Values

	Mean	S Dev.
Noise Factor	NaN	0.00
Noise Figure (dB)	NaN	0.00
Gain	NaN	0.00
Gain (dB)	NaN	0.00
Te (K)	NaN	0.00
Hot Noise (dBm)	NaN	0.00
Cold Noise (dBm)	NaN	0.00
Y	NaN	0.00
Y (dB)	NaN	0.00

After Correction Factors

	Mean	S Dev.
F1	NaN	0.00
NF1	NaN	0.00
Gain1	NaN	0.00
G1 (dB)	NaN	0.00
Te1	NaN	0.00

F1 after Ga Correction: 0
NF1 after Ga Correction: 0
Available Gain: 0

File Destination 2: H:\Measurements\Data\

Automation will save its results in the directory "File Destination 2"

Figure 9: LabVIEW Virtual Instrument developed for NF measurement system's user interface.

2.3.1 Hardware Setup

An overview of the entire measurement and instrument control system is provided in Figure 10. The 4396B combination analyzer provides true RMS noise powers (N_h, N_{h_2}, N_c, and N_{c_2}) using its spectrum analyzer function [39] and, through the 85046A S-parameter test set, the DUT's S-parameters (S_{11}, S_{22}, S_{12}, and S_{21}) or reflection coefficients (Γ).

A calibrated 50 Ω RF noise source (NW1M500-6-CS, NoiseWave, USA) produces a $T_h \approx 1361$°C when it is biased with +28 V and T_c equal to room temperature with 0 V bias (ENR of 6.66 dB at 127.73 MHz, obtained by linear interpolation of the values calibrated at 100 and 300 MHz). The ENR table for this noise source is shown in table 1. Bias voltage is provided by a Tenma 72-6630 programmable DC power supply which is controlled through its RS-485 port and a USB adapter by the desktop computer.

Frequency (MHz)	ENR (dB)
1	7.24
10	7.21
50	6.78
100	6.70
300	6.42
500	6.39

Table 1: The ENR vs. frequency table for the calibrated 50Ω noise source NW1M500-6-CS (NoiseWave, USA).

Noise power measurements using a spectrum analyzer require a preamplifier between the DUT and the analyzer's input to enhance sensitivity. The

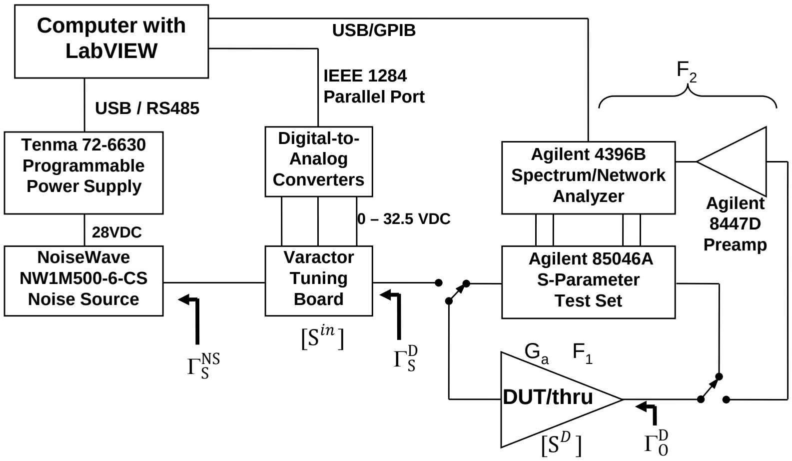

Figure 10: Block diagram of complete system setup including the Varactor Tuning Board (VTB) used for full noise parameter determination (see §2.5). Calibrating the system (second stage correction) requires replacing the DUT with a thru connection. Measurement quantities (S-parameters and reflection coefficients, Γ) used for available gain and NF determination are shown on the diagram. System NF (F_2) combines noise added by the 8447D preamplifier and the spectrum analyzer.

preamplifier raises the noise levels well above the instrument's noise floor and reduces system noise figure since spectrum analyzers tend to have high noise figures (by placing a lower noise figure device as the first block in the receiver the noise figure decreases according to the Friis formula for noise) [40, 41].

Our system uses an HP8447D preamplifier (Agilent, USA) which provides a nominal 25 dB of gain (actually measured $\sim$ 30 dB between 100 - 500 MHz) and input impedance very close to 50 Ω. Its noise figure is 5 dB between 100 and 500 MHz.

Proper connections are important to maintain low losses and adequate shielding from possible external sources of interference. Signal connections are therefore made using either RG-223 or double-braided RG-174 (G-02232D, Huber & Suhner, Switzerland) coaxial cable. Gold-plated SMA connectors were used for all connections except to the preamplifier and spectrum analyzer which require adapters to mate to the BNC and N connectors, respectively. Some preamplifiers receive DC power via the RF output in which case a bias tee (ZFBT-4R2G-FT+, Mini-Circuits, USA) was used. Since any contribution to noise figure from the bias tee is accounted for during the second stage noise correction, it has no influence on the final NF measured.

In addition to well-shielded cables, each device that was tested was housed in an RF-shielded enclosure. Most devices required test fixtures that were fabricated using double-clad copper FR4 PCB, including a ground plane that acted as part of the RF shield. The upper portion of the shield consisted of a folded brass foil box (Fotofab, Chicago, USA) which mates to the PCB ground plane by direct soldering or attached to spring clips (S1711-46R, Harwin, Portsmouth, UK) (figure 11a). To maximize shielding effectiveness, the test fixture was also tightly wrapped in kitchen-grade aluminum foil (figures 11b-11d). For some devices shielding using the PCB's ground plane was not possible, and therefore a dedicated metal box (model 392.16, TEKO Enclosure Solutions, Bridgeville, USA) was used. Holes were cut for connectors and a comb-lipped lid was used to close the box once the device was installed inside (figure 11e). Proper grounding was achieved by connecting the metal box to signal ground via a soldered internal connection. Cabling for DC bias voltages to the noise source and tuner (see §2.5.2) do not require the same level of shielding but care must be taken to avoid transferring environmental noise to the measurement chain through these connections. Both devices contain integrated low-pass filters where these DC connections penetrate the RF shield.

2.3.2 Measurement Procedure

The LabVIEW interface allows the user to specify typical measurement parameters including frequency, span, resolution and video bandwidth, as well as number of averages. Further details such as the voltage level and timing of the power supply states (relative to the spectrum analyzer measurements to achieve synchronization and ensure stable bias voltage) can also be adjusted.

The measurement procedure for noise figure with a standard source impedance of 50 Ω is summarized as:

1. Perform full 2-port calibration of network analyzer (SOLT)
2. Measure S-parameters of the DUT and noise source
3. Calculate available gain from S-parameters
4. Connect noise source directly to system preamplifier (thru connection)
5. Measure system noise figure
6. Apply correction factors to system noise figure:
   (a) Effective ENR correction
   (b) Temperature correction
7. Replace thru connection with DUT and measure overall noise figure
8. Apply correction factors to overall noise figure:
   (a) Effective ENR correction
   (b) Temperature correction
9. Apply Second Stage correction to extract DUT NF from overall NF.
10. Apply Available Gain correction to DUT NF
11. Export measurement data and calculated NF to text file.

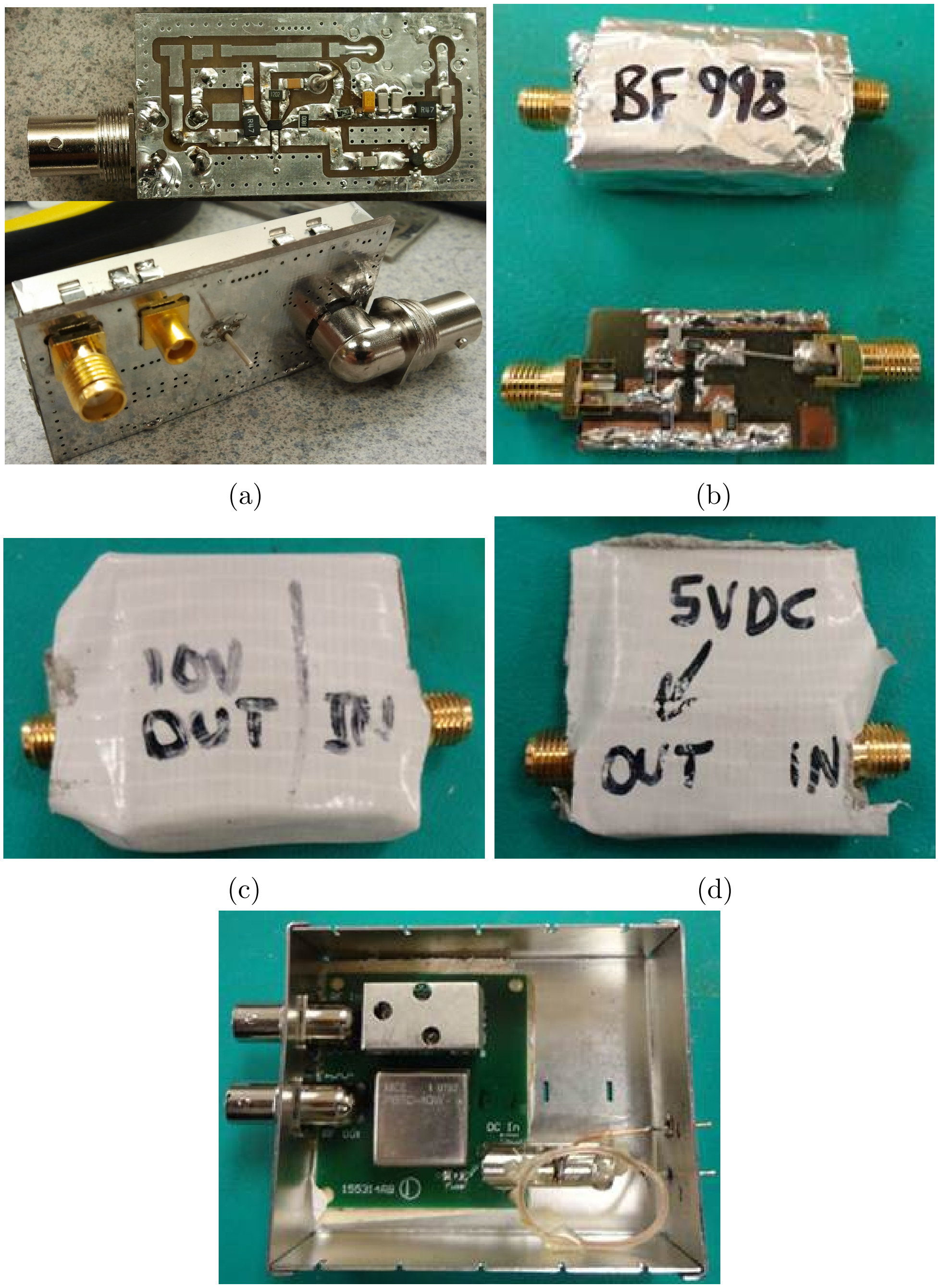

(a) (b)

(c) (d)

(e)

Figure 11: (a) A self built two stage preamplifier (BGB707L7ESD first stage, SGA-4286 second stage) using double-sided FR4 PCB and a folded brass foil box for RF shielding. (b) The BF998 amplifier test board unshielded (bottom) and RF shielded with aluminum foil (top). (c) The RF shielded MAR-8A+ amplifier test board. (d) The RF shielded MGA-53543 amplifier test board. (e) The metal box used for RF shielding with the proprietary MRI amplifier from Invivo installed.

Measurements were typically performed at a single frequency of 130 MHz in the RF lab (to avoid RF interference from a nearby 3T scanner) and 127.73 MHz (Larmor Frequency at 3T) in the RF shielded magnet room (c.f. §2.4). S-parameters are those of the amplifier and test board. S-Parameters were not de-embedded from the test board. Additionally, it should be noted that the test boards were assembled by hand and did not take advantage of reflow soldering. Since everything was done by hand, landing patterns and assembly methods specified by manufacturers were not always adhered to.

2.3.3 Performance Optimization and Validation

The choice of resolution bandwidth (RBW) and video bandwidth (VBW) have a great impact on measurement precision as well as measurement time. In general, to ensure accuracy RBW should not exceed the passband of the DUT but also be wide enough so that noise powers are not near the system's noise floor [40, 41]. In the 4396B measurement time decreases as RBW is increased with the fastest measurement times being 25 μs per point for an RBW of 10, 30, and 100 kHz (801 points total, VBW = RBW). Below RBW = 10 kHz measurement times increase approximately one order of magnitude due to an internal change from digital to analog filtering. As VBW is reduced (1/1, 1/3, 1/10, 1/30, 1/100, and 1/300 of RBW) measurement uncertainty improves at the cost of increased measurement time (up to 6.4 ms per point for VBW = RBW/300).

A reasonable compromise between measurement time and uncertainty is achieved when each noise power measurement is performed at a single frequency using RBW = 100 kHz, VBW = RBW/30, 30 averages, and a fictitious frequency span of 10 kHz, divided into 801 points of measurement. The measurement time is 0.8 ms per point, for a total of 19 s for each noise power measurement and a total time of 50 s for the two powers required for the Y-factor measurement, including delays in data transfer and power supply switching.

The final noise power measurement is obtained by calculating the mean of the 801 individual points; the standard deviation can also be calculated to assess the accuracy of the measurements. Standard deviation of the 801 Y-factor measurements was ~ 0.2 dB with a corresponding noise figure standard deviation of $0.2 - 0.3$ dB. Measurement time is directly proportional to the averaging factor, and the standard deviation is thus proportional to the square root of measurement time. If averaging is increased to 100, the standard deviations for Y-factor and noise figure drop predictably ~ 0.1 dB and $0.1-0.2$ dB, respectively. However, the means were found to be unaffected by this increase in averaging and therefore an averaging factor greater than 30 was rarely used.

2.3.4 Results

The noise figures of a variety of standard commercial and dedicated MRI amplifiers were measured. The commercial devices (tested directly soldered to corresponding test boards etched in-house) and corresponding semiconductor descriptions are:

- MGA-53543 (Avago, USA): GaAs pHEMT RFIC;
- MAR-8A+ (Mini-Circuits, USA): InGaP HBT in Darlington configuration;
- BF998 (NXP Semiconductors, Eindhoven, The Netherlands): N-channel Si dual-gate MOSFET;
- BGB707L7ESD (Infineon, USA): SiGe MMIC .

The proprietary purpose-built 3T and 4.7T MRI preamplifiers were measured while connected to dedicated test boards and connection adapters as needed. The devices, and corresponding semiconductor technology when known, are

- InVivo (Gainesville, FL, USA) integrated GaAs preamplifier
- Microwave Technology (Fremont, CA, USA) MPH200282, four units, 200 MHz (abbreviated "MwT")
- Philips (Best, The Netherlands) research preamp #1: Si MOSFET
- Philips research preamp #2: SiGe
- USA Instruments (Aurora, OH, USA) Low Noise Pre-amplifier model 110595 (inside Philips 8-channel interface box, abbreviated "USAI")

Additionally, the 8447D (Agilent, USA) preamplifier for the measurement system was also measured. Because this amplifier is normally used as the measurement system's pre-amplifier, the MSA-0786 (Avago, USA) amplifier (on a test board) was used as a stand-in preamplifier for the measurement system during measurement of the 8447D (since a second 8447D was not available for this measurement). Table 2 compares the results obtained with our measurement system to those from an HP8970A Noise Figure Meter (Agilent, USA) and from a ZVL3 Vector Network Analyzer (Rohde & Schwarz, USA) with noise figure option (FSL-K30), both using the aforementioned noise source (NW1M500-6-CS, NoiseWave, USA). All measurements used the same noise source to ensure consistency. Note that since the above commercial instruments do not have tuners, these noise figures are not necessarily minimum noise figures, but simply noise figures corresponding to a source impedance of 50 Ω at the DUT input. Since our measurement system was the only one capable of available gain correction, comparisons between the instruments are made with noise figures calculated using insertion gain. These measurements are in excellent agreement (typically within < 0.1 dB) thus confirming that our methods are consistent with those of established instrumentation. In the case of the BF998, the 0.2 dB measurement range is attributed to the highly reflective input and output reflection coefficients, low gain of this amplifier, and optimal source impedance that is much different from 50 Ω, leading to a

	Amplifier	**M.S.**	**M.S. w/o $\mathbf{G_a}$ corr**	**NFM**	**ZVL**
NF (dB)	MGA-53543	0.73	0.71	0.76	0.71
	MAR-8A+	2.35	2.35	2.37	2.34
	BF998	4.47	3.63	3.41	3.31
	USAI	0.92	0.92		0.96
	InVivo	0.55	0.55	0.55	0.56
	Philips Si	1.76	1.59		1.60
	8447D	4.99	4.97		4.83
$\mathbf{G_i}$ (dB)	MGA-53543	23.14		22.68	23.59
	MAR-8A+	30.04		30.08	31.45
	BF998	7.13		6.91	8.79
	GE	25.49			24.43
	Invivo	27.89		27.66	28.63
	Philips	15.92			17.44
	8447D	28.93			30.11

Table 2: Noise figures and insertion gains obtained with a 50 Ω source impedance at 130 MHz using our measurement system (M.S.) with and without available gain (G_a) correction, compared to those obtained using the commercial HP8970A noise figure meter (NFM) and ZVL3 VNA with built-in NF option (ZVL). The BGB707L7ESD, MPH200282, and Philips SiGe amplifier were not used for system validation and do not appear in this table. Not all devices were measured using the Noise Figure Meter and as such, some values are missing in this column.

relatively large noise figure (see §2.5). The Agilent 8447D also has a 0.2 dB measurement range due similarly to the large ~ 5 dB noise figure as well as to the use of a low gain preamplifier (MSA-0786).

Data are provided in Table 2 using available gain correction to show that it has greater effect on amplifiers that have low noise figures and reflective inputs. These requirements are typical of preamps used for MRI array coils and thus available gain correction is essential to obtain precise noise figure measurements for these devices. Note that the BGB707L7ESD, MPH200282, and Philips SiGe preamplifier do not appear in this table as these devices were measured later and not used for initial validation of the measurement system.

2.4 Characterization in Strong Magnetic Fields

Noise figure and gain in a semiconductor device are affected by magnetic field strength and orientation [32–34]. This is a consequence of the Hall effect which describes how the paths of motion of charge carriers within the semiconductor changes as a result of the Lorentz force. The relationship between direction of current flow and magnetic field orientation is important since only the magnetic field component perpendicular to charge motion will create a force.

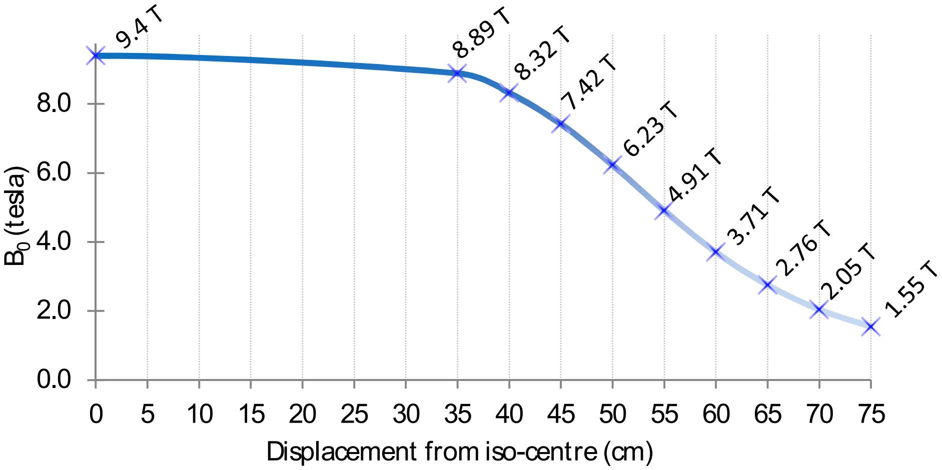

Figure 12: B_0 drops off as the distance from magnet iso-centre increases on the 9.4 T animal magnet. Preamplifier measurement positions are marked with an x.

To test the influence of the Hall effect on noise figure, measurements were performed on several amplifiers in the presence of a strong magnetic field produced by a 9.4 T animal magnet (205 mm bore, Magnex, UK). The B_0 field strength was varied from 1.55 T to 9.4 T by positioning the DUT at different points along the axis of the magnet bore (figure 12). An additional measurement was performed with the DUT in a corner of the magnet room's iron shield to approximate a zero field point.

Because of the dependence on orientation S-parameters were first measured with the amplifier placed in three orthogonal orientations (Figure 13, bottom). The three orthogonal orientations of the DUT are denoted as parallel, transverse, and through-plane, corresponding, respectively, to orientation of the test board with the magnet axis parallel to the axis of the RF connectors or RF signal path; parallel to the test board but orthogonal to the RF signal path; and orthogonal to the test board. The orientation that resulted in the greatest change in $|S_{21}|$ relative to zero field was chosen as the orientation used to characterize the noise figure's sensitivity to B_0. The S-parameters were acquired for each location inside the bore, allowing for an available gain correction for each measurement point. The DC current draw of each amplifier was also measured at each location with a digital multi-meter to monitor changes in bias point.

2.4.1 Measurement Setup and Corrections

The measurement system was kept outside the 5 gauss line for safety (some ferromagnetic material is present) as well as to avoid damage to the instruments' electronics from the magnetic field and to avoid unknown influences on the measurements that cannot be calibrated. Consequently, two lengths of 8.5-meter double-shielded coaxial cable (RG-223) were run from the measurement system, through bulkhead BNC connectors in the magnets RF cage to the magnet bore. The network analyzer was calibrated with these cables in place to obtain accurate DUT S-parameters. Because of attenuation due to the length of the cable between the DUT and noise source, the ENR of the noise source must be replaced with the effective ENR according to Eq. 32, where the S-parameters are those of the 8.5-m coaxial cable [38]. The preamps did not require the same level of shielding used for bench measurements since no external interference is present within the RF cage.

The noise figure measurement procedure is that described in §2.3.2 for a 50 Ω source impedance at zero field. After a thru connection was placed between the two 8.5 meter coaxes (one cable leading from the noise source to magnet bore, and the other from the magnet bore to the preamplifier and spectrum analyzer) where the DUT would be connected in the magnet bore, the second stage noise figure was measured using the effective ENR. The temperature correction was applied to the noise figure and the data was stored for use in the second stage correction. The thru connection was then replaced with the DUT and the noise figure was measured at each of the positions in the magnet bore. Each noise figure was calculated with the effective ENR and corrected for temperature, second stage noise figure, and the available gain that corresponds to that magnetic field strength. Figure 13 provides an overview of the system setup.

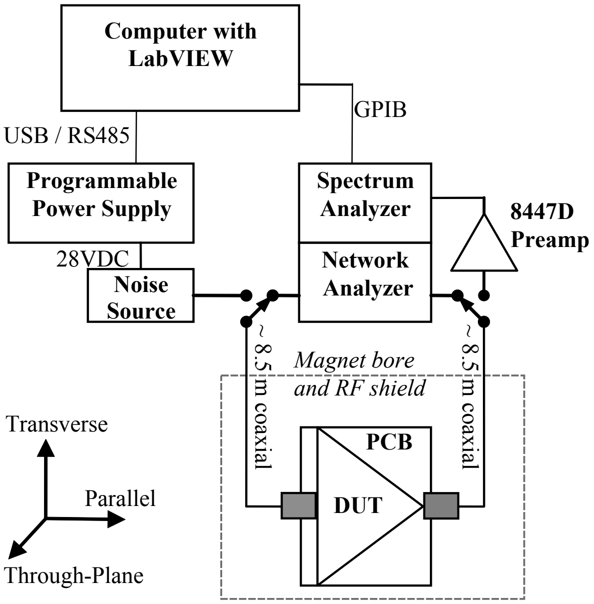

Figure 13: Setup for in-bore noise figure measurement (50 Ω source impedance) excludes the VTB and employs long coaxial cables to reach from the 5 gauss line into the magnet bore. Three orientations were used: parallel to coaxial connectors (signal path), perpendicular to connectors but parallel to PCB (transverse), and perpendicular to PCB (through-plane). ENR correction is especially important due to the long coaxial cables.

2.4.2 Results

The MGA-53543, MAR-8A+, BF998, BGB707L7ESD, MwT MPH200282, InVivo proprietary, and two Philips research amplifiers were all measured at 127.73 MHz and characterized in the magnetic field. The 8447D and USA Instruments amplifiers are in housings that are physically too large to fit within the 12-cm gradient-coil bore and were thus excluded from these measurements.

The two silicon-germanium (SiGe) amplifiers (Philips research MRI amplifier #2 and the BGB707L7ESD) demonstrated little to no change in S-parameters, regardless of the orientation of the amplifier within the magnetic field. Among the rest of the amplifiers, with the exception of the MAR-8A+, all amplifiers experienced the greatest change in $|S_{21}|$ in the through-plane orientation relative to the magnetic field. The MAR-8A+ saw its greatest change in $|S_{21}|$ when the amplifier was placed in parallel orientation relative to the magnetic field.

The noise figure of most amplifiers increased noticeably as the strength of the magnetic field was increased (Figure 14a). Likewise $|S_{21}|$ and available gain of most amplifiers was reduced by increasing magnet field strength (Figure 14b). The degree of reduction was related to the electron mobility of the semiconductor and device geometry (e.g., channel length and width in field-effect transistors) used: field-effect devices with lower mobility such as silicon exhibit a lower sensitivity than those with high mobility such as GaAs. Conversely, the SiGe devices are based on bipolar transistors with a very thin base and hence their insensitivity results from the short distance over which the magnetic field acts on electrons [33, 34]. The input reflection coefficient (S_{11}) was nearly constant for most devices as a function of magnetic field strength (Figure 14d), with the exception of the MGA-53543 and MAR-8A+.

The Philips research silicon (Si) MRI amplifier #1, which employed active current biasing, was notable because the effect of B_0 was much more limited for this amplifier than for the other Si amplifier (BF998). Furthermore, while the current draw on all other amplifiers dropped as the field strength increased (with the exception of SiGe amplifiers, which were not affected in any way), the current draw of the Philips Si amplifier increased to nearly double its zero field current draw at 9.4 T (Figure 14c). The noise figure and gain of the Philips Si amplifier were essentially constant throughout the entire range of field strengths. These results suggest that active bias adjustment may be able to compensate for the effects of B_0, although adjusting the bias voltage of other preamps to maintain a constant current was found to be insufficient.

Four MwT receive array preamps (MPH200282), arranged in pairs on two circuit boards, were measured against varying B_0 field at 200 MHz. On each board, one preamp had a lower NF (~ 0.6 dB, devices 1 and 3) and the other had a higher NF (~ 0.7 dB, devices 2 and 4), probably due to manufacturing differences. The noise figure of all four devices increased with increasing B_0,

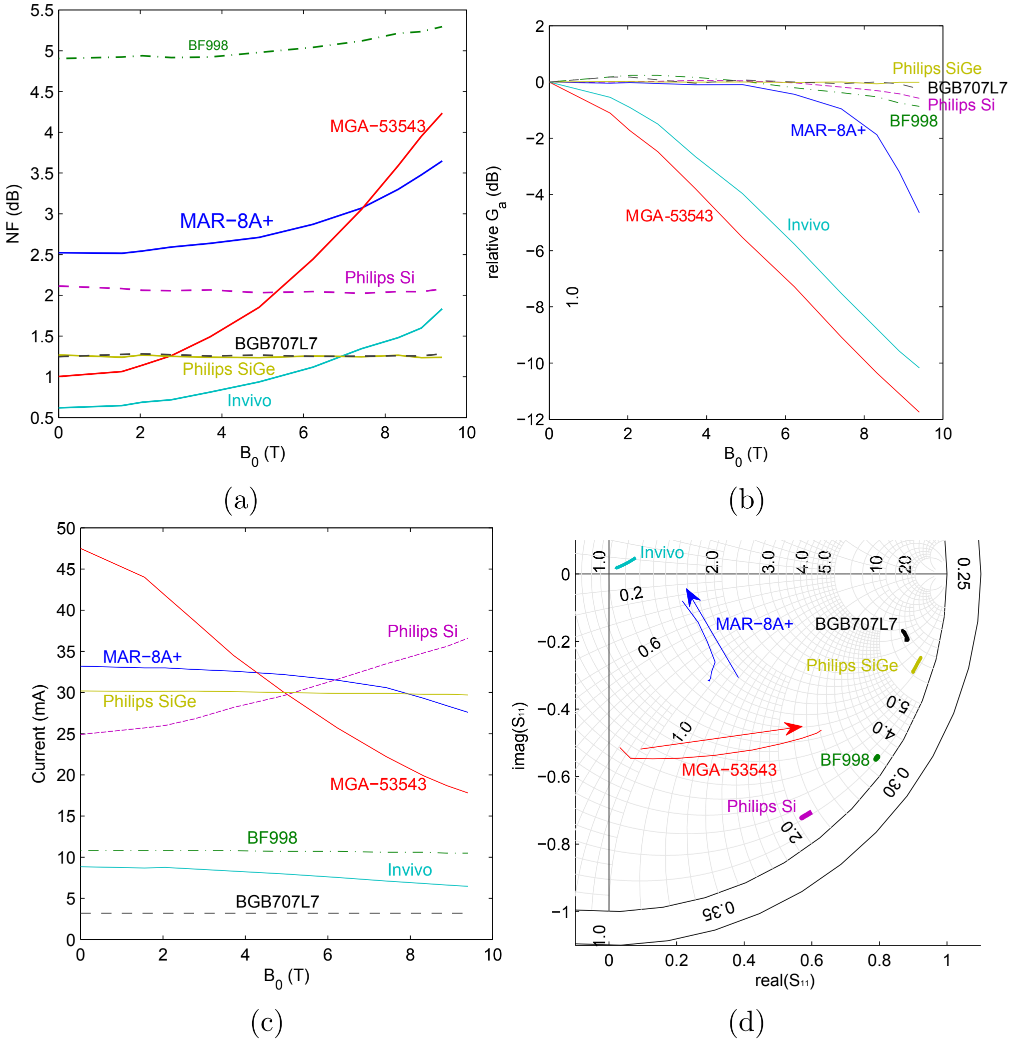

(a) (b) (c) (d)

Figure 14: Effect of magnetic field strength on (a) noise figure, (b) available gain (relative to zero field), (c) current draw, (d) and S_{11} (arrows indicate direction of increasing B_0). All measurements are performed at 128 MHz and in the most sensitive (worst-case) orientation for each amplifier

but this increase was higher for the devices with a higher baseline NF. The test board for the BGB707L7 device measured earlier at 127.73 MHz was upgraded to a two-stage amplifier with the addition of an SGA-4286 (RFMD, USA) as a second stage. The available gain of this two-stage amplifier was similar to that of the MPH200282 ($G_a = 29.4$ dB compared to 26.4 dB for the MPH200282) allowing for a fair comparison of these widely differing semiconductor technologies. Results shown in Figure 15 confirm the SiGe device's insensitivity to B_0.

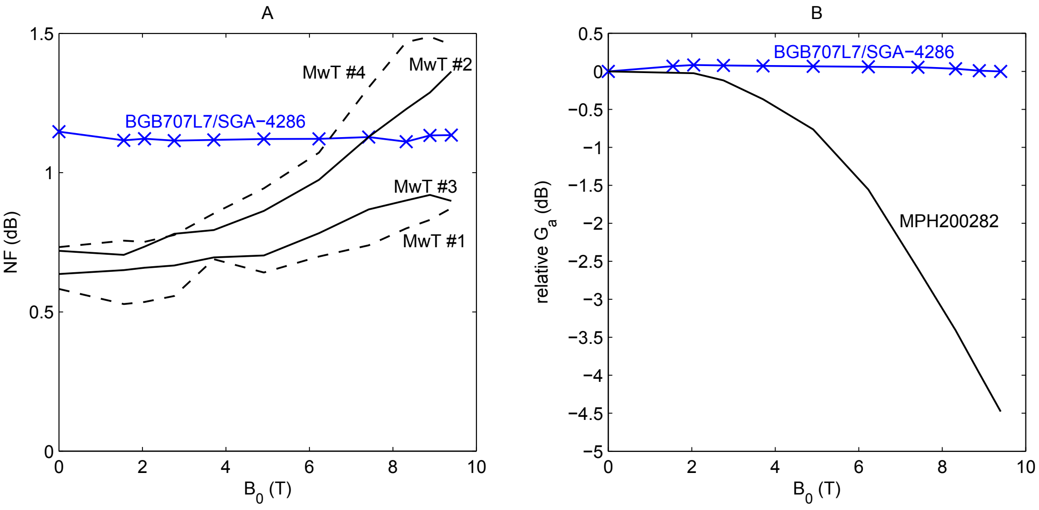

Figure 15: Effects of the magnetic field at 200 MHz on (a) the noise figure of a BGB707L7/SGA-4286 two-stage amplifier and four MPH200282 (MwT) MRI array preamplifiers; (b) the corresponding change in available gain (relative to zero field) of the aforementioned devices.

2.5 Noise Parameter Measurements

2.5.1 Linear Noise Model

The noise figure of a linear device such as an amplifier is a function of the impedance or admittance of the signal source connected to its input. This variation in noise figure is described by the linear noise model [31]

$$F = F_{min} + \frac{R_n}{G_S}|Y_S - Y_{opt}|^2 \tag{33}$$

where the noise resistance (R_n), optimal conductance (G_{opt}), optimal susceptance (B_{opt}), and minimum noise factor (F_{min}) are known as the noise parameters. These noise parameters may be determined by making several noise factor (F) measurements at various input admittances ($Y_S = G_S + \jmath B_S$). With at least four data points, fitting routines are used to estimate the noise parameters [31, 42, 43].

Since the noise source presents a 20 mS admittance (Y_S) at its output, a tuner is required to transform it to other values required to determine the noise parameters. In automatic systems such as ours, an electronically adjustable tuner (Figure 16) is connected between the noise source and the DUT (Figure 10), transmitting the noise from the noise source, and presenting it to the DUT with an adjustable source admittance.

2.5.2 Tuner Design

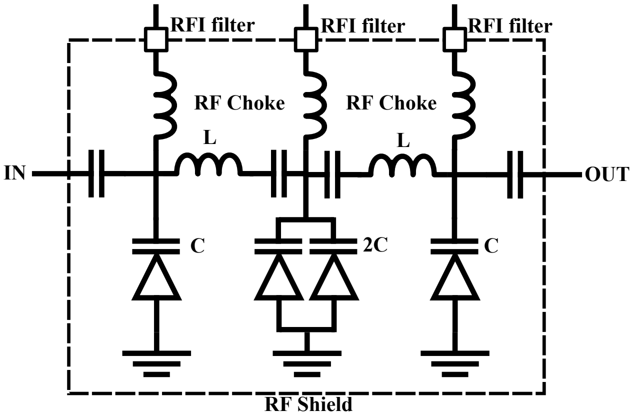

Figure 16: Double-π varactor diode tuning board circuit. Dashed box indicates RF shielding through which RF signals are routed using coaxial SMA connectors and DC control voltages through RFI filters (4209-053LF, Tusonix, Tucson, USA). Inductors (L) are 68 nH RF chip inductors (1206 CS, Coilcraft, USA). Varactors (C) are ZC836BTA (Zetex Inc.).

The varactor tuning board (VTB) used in our system consists of a double-π network of capacitances and inductances (Figure 16), and is inspired by the half-wavelength transmission-line tuners used at higher frequencies [44–46]. Varying the reverse bias voltage across varactor diodes (ZC836BTA, Zetex Inc.) adjusts the small-signal capacitances, which allows the 20 mS admittance of the noise source to be transformed to nearly any complex value.

The diodes' bias voltages are produced by three AD420 (Analog Devices, USA) digital-to-analog converters (DAC) with 16-bit registers. LabVIEW controls each DAC by sending it a 16-bit unsigned integer value through the PC's parallel port. The DACs produce a DC current at the output between 0 and 20 mA (in steps of 305 nA) which is converted to a voltage between 0 and 25.4 V by passing this current through a 1.27 kΩ resistor. These DC voltages are then fed into the RF shielded enclosure housing the tuning board via RFI filters (4209-053LF, Tusonix, Tucson, USA) and to the varactors through 1.2 μH RF chokes (9250-122-RC, Bourns, Riverside, USA) to maximize shielding and isolation between the DC lines.

The double-π network (Figure 16) was simulated in MATLAB to determine the theoretical coverage of the Smith Chart using 68 nH inductors and the above bias voltage range (dashed contour in Figure 17). The 16 bit resolution of the DACs does not limit the variety of achievable source admittances. The simulation shows complete coverage of the central region of the Smith Chart, while, similarly to other tuner designs, achieving all highly reflective admittances at the edges is not possible due to limited capacitance range and losses. This limitation, however, is not restrictive since optimal source impedances are typically not found in these regions. A table was created (see Calibrations, §2.5.3, below) of the effective ENR value corresponding to each tuning state to be used for each individual NF measurement point. In some regions the effective ENR values that are achieved can be too small to yield reliable NF measurements, thus further limiting the useful coverage of the Smith Chart. The noise parameter measurements below were obtained using the 85 admittance points shown in Figure 17 which were chosen to cover uniformly as much of the Smith Chart as possible while maintaining an effective ENR greater than 3 dB.

The tuning board was not designed to operate within a strong magnetic field so if noise parameter measurements are desired at high field, the tuning board must be kept outside of the 5 gauss line.

2.5.3 Calibrations

Figure 10 provides an overview of the system setup for noise parameter measurement. Since the tuning board is positioned between the noise source and DUT, the S-parameters of the tuning board were measured separately to calculate the effective ENR at each source admittance point. This was automated using the LabVIEW program by stepping through all the chosen points and measuring the S-parameters of the VTB using the network analyzer. These data are saved in a table containing, for each tuning point, the three 16-bit integers required for that tuning setting (DAC voltages), the calculated effective ENR, as well as the source admittance.

Once the effective ENR correction data was saved, second stage noise figure calibration was performed by connecting the tuning board between the noise source and the system preamplifier. The tuning board was tuned to 20 mS input admittance and the second stage noise figure was measured and stored (using the effective ENR for that tuning and corrected for ambient temperature) similarly to the procedure in §2.3.2.

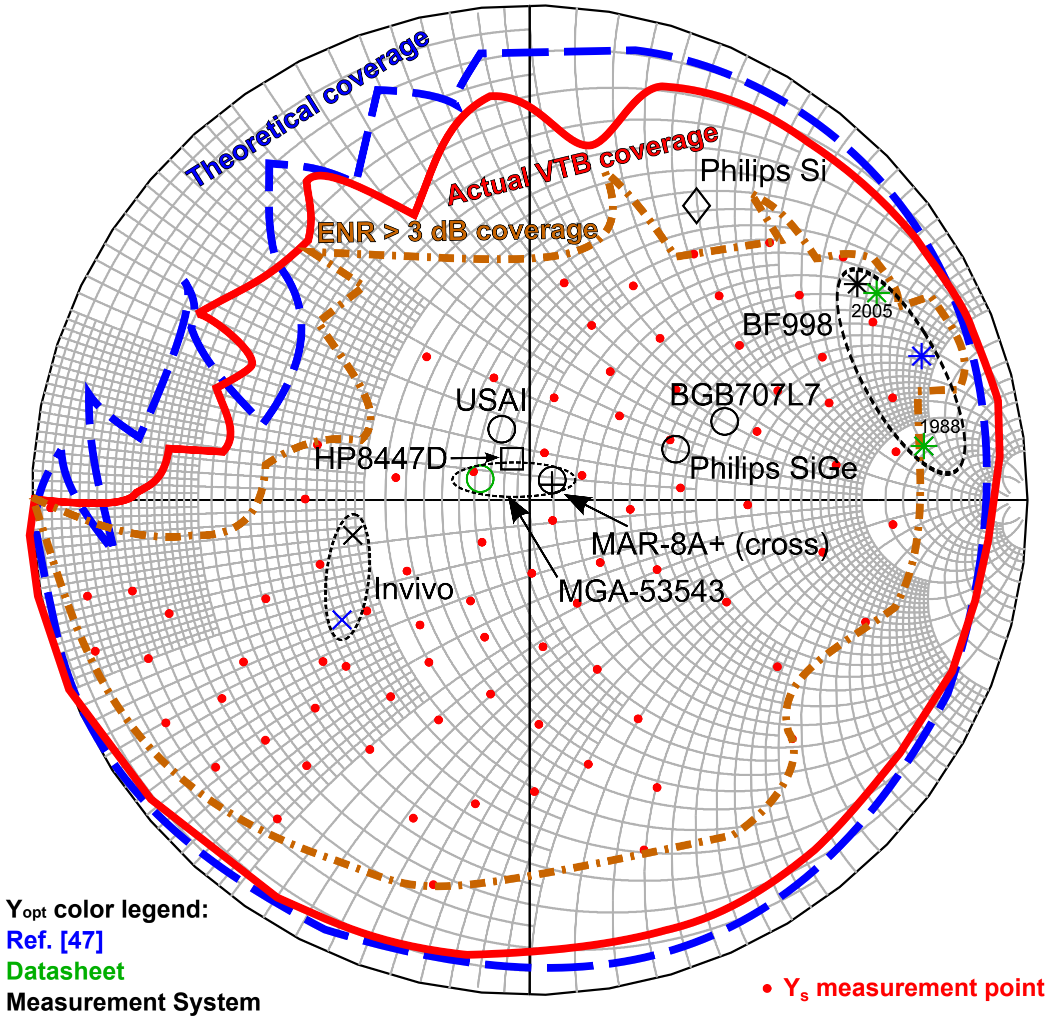

Figure 17: Optimal source admittances (color coded by data source) of the preamplifiers of Figures 14. Red dots are the source admittance points used for the noise parameter fitting. Contours show the theoretical Smith Chart coverage of the tuning board (blue/dashed), actual coverage (red/solid), and coverage achieved with an effective ENR > 3 dB (brown/dash-dot). Theoretical coverage includes a rotation of 25° clockwise to account for a short length of coaxial cable after the tuning board output.

The DUT was then inserted between the tuning board and system preamplifier and the noise figure was measured at all 85 tuning points using the corresponding effective ENRs. The noise figure was corrected for temperature, second stage noise figure, available gain, and second stage noise figure (Eqs. 25, 26, and 31). Source admittances corresponding to measured noise figures were saved to a data file and subsequently used with a least-squares fitting method to calculate the noise parameters (see §2.5.1) using Lane's linearization method [42, 43].

2.5.4 Results

Table 3 lists the noise parameters of the MGA-53543, BF998, MAR-8A+, InVivo, USA Instruments, 8447D, BGB-707L7ESD and Philips research amplifiers obtained by fitting the linear noise model of Eq. 33 to the noise factors measured over all 85 source admittances of Figure 17. This figure also provides a comparison between the optimal source admittances, Y_{opt}, determined with our system and those provided by the manufacturer or those in Ref. [47]. There is good qualitative agreement between these admittances as indicated by distances that are below 0.2 when displayed on the Smith Chart (a circle of unit radius).

	$\mathbf{R_n(\Omega)}$	$\mathbf{G_{opt}}$ **(mS)**	$\mathbf{B_{opt}}$ **(mS)**	$\mathbf{F_{min}}$ **(dB)**	$\mathbf{G_a}$ **(dB)**	$\mathbf{R^2}$	**RMS fit error (dB)**
MGA-53543	5.07 (5.00)	18.21 (24.30)	-1.48 (-2.12)	0.73 (1.07)	23.75	0.99	0.09
MAR-8A+	19.27	18.26	-1.15	2.23 (2.26)	30.65	0.99	0.14
BF998	79.8	2.60	-5.93	1.42	12.84	0.96	0.27
USAI	5.62	21.42	-6.3	0.9	24.57	0.96	0.18
InVivo	1.52	41.27	6.77	0.43	28.0	0.99	0.08
Philips Si	20.91	4.89	-11.01	0.73	22.30	0.99	0.18
8447D	39.38	21.14	-3.57	4.89 (5.07)	28.40	0.97	0.22
Philips SiGe	12.88	10.74	-2.45	1.08	19.30	0.99*	0.10
BGB707L7	17.50 (11.50)	8.37 (3.81)	-3.24 (-3.36)	0.47 (0.4)	13.30	0.98	0.39

*rounds to 1.00

Table 3: Noise parameters measured at 130 MHz using our system equipped with the Varactor Tuning Board (VTB). Values from the devices' datasheets are reported in parentheses for the MGA-53543, MAR-8A+ and BGB707L7 (at frequencies of 500 MHz, 100 MHz, and 150 MHz, respectively). For the HP8447D the datasheet F_{min} was calculated from the gains and noise factors at 100 MHz of the three stages from which it is assembled (MSA-0786 first stage and MSA-0486 for the 2nd and 3rd stages).

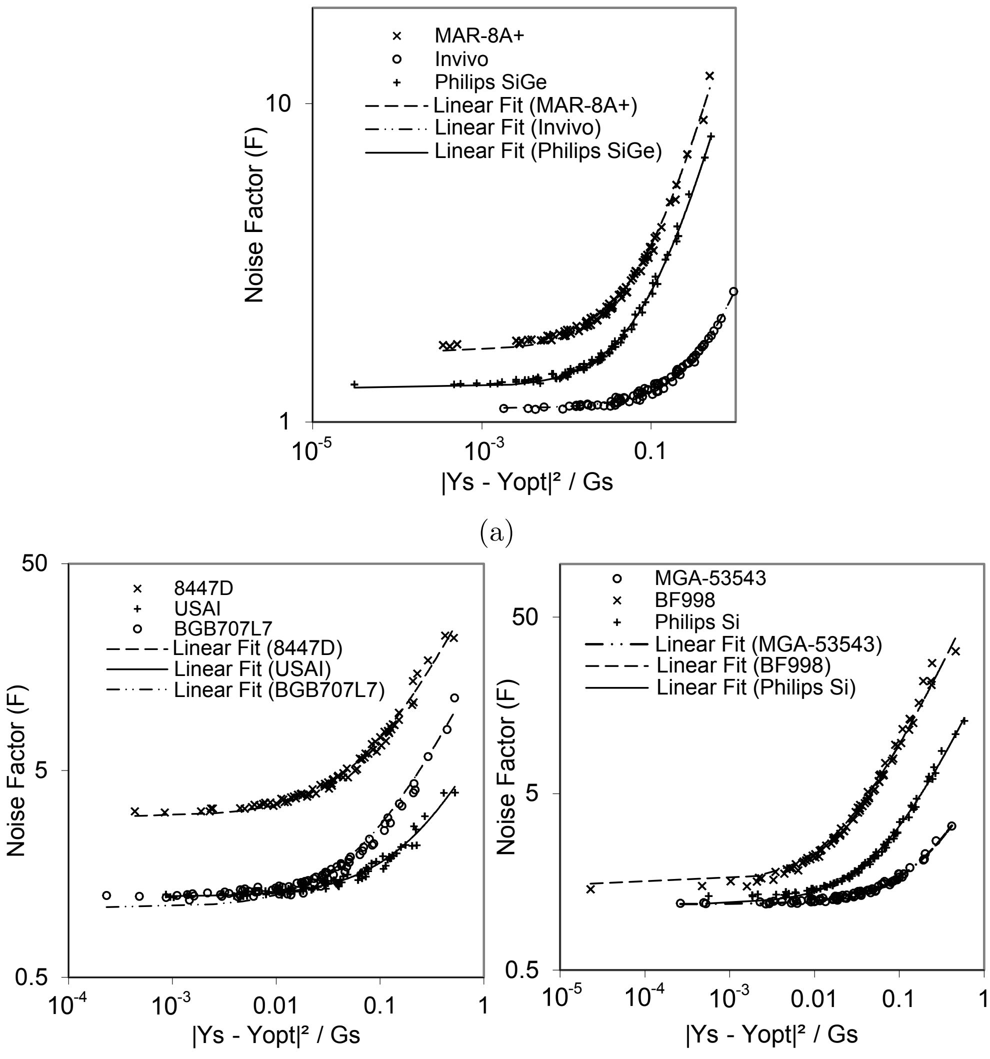

(a)

(b)

(c)

Figure 18: (a) representation of noise parameter fits for the MAR-8A+, InVivo integrated preamplifier, and Philips SiGe research MRI amplifier; (b) 8447D (Agilent, USA), USA Instruments (USAI), and BGB707L7ESD (Infineon, USA); (c) MGA-53543 (Avago, USA), BF998 (NXP Semiconductors, Eindhoven, The Netherlands), and research Philips Si MRI preamplifier at 128 MHz. Note the use of logarithmic scales on both axes to accentuate the spread of the data points.

The quality of the noise parameter fits is illustrated in Figure 18 and quantified by the coefficients of determination (R^2) and RMS fit errors in Table 4. The best fitting quality is obtained for preamplifiers that have optimal source admittances that are near the centre of the Smith chart. Conversely, preamps whose Y_{opt} is near the edge of the tuner's useful range (e.g., BF998) can deviate somewhat from the theoretical model. These deviations may be due to the consequently highly asymmetric sampling distribution around Y_{opt}

as well as to the small number of points in its proximity and the correspondingly low ENR in these peripheral regions of the Smith chart. For the BF998 and BGB707L7 the relatively low gain may also contribute to what appears to be an underestimation of the noise factor. Table 3 includes values provided in the manufacturers' datasheets for the MGA-53543, BGB707L7, and the MAR-8A+ at 500 MHz, 150 MHz, and 100 MHz, respectively.

BF998	**VTB**	**s2p parameter file**		**Ref. [47]**
		Infineon 2005	**SIEMENS 1988**	
$\mathbf{NF_{min}(dB)}$	1.42	1.59	0.77	1.45
$\mathbf{R_n(\Omega)}$	79.8	128.8	65	98.5
$\mathbf{G_{opt}(mS)}$	2.60	2.22	2.23	1.80
$\mathbf{B_{opt}(mS)}$	-5.93	-5.48	-1.38	-3.55
RMS fit error	0.27			0.11
$\mathbf{S_{11}}$ **mag (dB)**	-0.12			-0.51
$\mathbf{S_{11}}$ **angle** (°)	-23.9			-31.6

Table 4: Noise parameters of the BF998 (NXP Semiconductors, Eindhoven, The Netherlands) measured using the Varactor Tuning Board (VTB), compared to values from the manufacturer (interpolated to 130 MHz from s2p device parameter files from Infineon Technologies (2005) and Siemens (now Infineon), Munich, Germany (1988)) [48, 49], and those in Ref. [47].

There is overall agreement in the noise parameters of all three devices, especially for the minimum noise factors, F_{min}. Some discrepancies could be due to the fact that our measurements were performed at 130 MHz with test fixtures that differ from those used by the manufacturers. For the MGA-53543 the F_{min} measured at 130 MHz is substantially lower than that at 500 MHz, which is consistent with this device's trend of noise figure decreasing with decreasing frequency. The minimum noise factor is not available at specific frequencies from the manufacturer of the HP8447D system preamplifier (only $NF < 8.5$ dB is specified for $0.1-1300$ MHz). The value used for comparison in Table 3 was therefore calculated using the Friis formula from the gains and noise factors of the three stages from which it is assembled. Datasheet values at 100 MHz were obtained for the MSA-0786 first stage and MSA-0486 for the 2^{nd} and 3^{rd} stages (both devices Avago, USA), and the resulting noise factor is within 0.2 dB of the measured value.

Representative noise parameter results for the BF998 are shown in Table 4 including values from one manufacturer's simulation model [48, 49] and those in Ref. [47]. Because of the poor quality of the fitting for this device, large noise figure measurements at the opposite side of the Smith chart have a great influence on the fitted noise parameters, and if these are excluded the solution changes considerably.

The noise parameters of the integrated MRI amplifier supplied by InVivo are shown in Table 5 along with values found in Ref. [47] and the noise figure provided by the manufacturer for comparison.

Invivo	**VTB**	**Datasheet**	**Ref. [47]**
$\mathbf{NF_{min}}$(dB)	0.43	0.45	0.46
$\mathbf{R_n}$(Ω)	1.52		1.56
$\mathbf{G_{opt}}$(mS)	41.27		35.79
$\mathbf{B_{opt}}$(mS)	6.77		-21.64
RMS fit error	0.08		0.08
$\mathbf{S_{11}}$ mag (dB)	-0.06		-2.39
$\mathbf{S_{11}}$ angle (°)	-179		171

Table 5: noise parameters of the InVivo integrated preamplifier measured via the Varactor Tuning Board (VTB), compared to those from the manufacturer, and those from Ref. [47].

Results do not suggest that the tuning board injects any noise into the measurement system as noise figure measurements at 50 Ω source impedance matches noise figure measurements using the noise source without tuning board (which is a 50 Ω source impedance).

2.6 Conclusions and Future Work

The noise figure measurement system described above is an effective solution for the typical MR laboratory. Measurements are repeatable, with an acceptable standard deviation, and the accuracy was validated against both a dedicated noise figure meter and a spectrum analyzer with a noise figure measurement feature. Our system's modular programming allows additional correction factors to be included for more accurate determination of the noise figure. Available gain correction, for example, is not available on either of the other two commercial NF measurement systems. New features can be easily implemented due to the flexibility of the system and programming environment.

The system was used to measure the noise figure behavior of several preamplifiers in high magnetic fields. Noise figure tends to increase as the field strength increases, and the extent of this effect is dependent on the orientation of the device and on the semiconductor's manufacturing parameters such as electron mobility and channel length. Bipolar SiGe devices were found to be insensitive to fields up to 9.4 T thanks to their very thin base. Amplification, or $|S_{21}|$, tends to be attenuated by high field strength while for most devices input match (S_{11}) remained stable.

Noise parameter measurements are also presented for several preamplifiers. These measurements are often unavailable from manufacturers even though they are required to determine the optimal noise matching condition which maximizes SNR. Our results indicate overall agreement with data that is available for comparison, but they also highlight variability in the quality of fitting to the standard linear noise model. The best fits were achieved for devices with high gain and optimal source impedance near the centre of the

Smith chart. Results may be improved by tuner designs with reduced losses.

Further areas of improvement include implementation of RF switches to automate switching between network and spectrum analyzer ports, thus allowing faster and more automated noise figure measurements.

3 B_1 Shimming via Quadrature Phase Shifting

3.1 Summary

The homogeneity of the B_1 field suffers in high field MRI due to the reduced RF wavelength at higher frequencies and the shortening effects of dielectrics upon this wavelength. Based on empirical observations made by others, a variety of strategies were employed to optimize the performance of the transmit coil. In specific improving the B_1 homogeneity and transmit power efficiency was of interest. The transmit coil has good homogeneity when the coil is loaded with a silicone oil phantom, suggesting that the poor homogeneity of the coil is due to dielectric effects rather than poor coil design. Measurements of the coil do, however, indicate that both ports of the quadrature-driven coil are poorly matched and there is significant coupling between the ports when the coil is loaded with an insert receive array, phantom, and placed at iso-centre within the magnet bore of the MRI system.

B_1 shimming was attempted by altering the phase delay on the quadrature port of the birdcage coil. While experiments within the human head indicated that a phase shift greater than quadrature (90°) by about 28° (for a total delay of 118°) improved overall coil efficiency and homogeneity, these results could not be verified in an imaging phantom purpose-built to simulate the axial cross-section of the human head. To better understand the behaviour of the B_1 field, the transmit coil was repositioned along the axis of the bore and rotated. The imaging phantom was also moved along the axis of the bore. By far the greatest influence on the B_1 field is the dielectric effect both at the boundaries and within the imaging sample.

Effective B_1 shimming experiments can only be performed with a human volunteer or a life-like phantom that accurately models the human head. Using a longer cable on the quadrature port of the birdcage coil (with an excess electrical length of 28° or physical length of 7.4 cm) will maximize transmit power efficiency for the average human head. Certain phantoms require a phase shift in excess of 50° to produce any visible effect on the B_1 field. The reason behind this can be easily explained by looking at the individual port B_1 maps for the birdcage coil and examining how the fields are combined with a phase shift to produce the circularly polarized B_1 field.

B_1 field homogeneity could be improved by rotating the birdcage coil by a quarter-turn. Transmit power efficiency could be increased by repositioning the coil centre 60 mm above magnet iso-centre. There exists an optimal loading condition for the coil which minimizes the power reflected (and consequently dumped into a 50 Ω load).

3.2 Introduction

The high field MRI system available at the Peter S. Allen MR Research Centre is the Varian INOVA 4.7 T. This system produces better SNR and higher resolution images than clinical systems. As discussed in §1.4.2, the radio frequency (RF) wavelength is reduced due to an increase in the Larmor frequency. As the RF wavelength is shortened, B_1 field homogeneity degrades [19]. The wavelength (λ) is further shortened by the relative permittivity of the imaging sample (ϵ_r) according to:

$$\lambda = \frac{\lambda_0}{\sqrt{\epsilon_r}} \tag{34}$$

This shortening of the RF wavelength and increasing inhomogeneity of the B_1 field is responsible for image artifacts which manifest as shading in images which is not indicative of the geometry (or anatomy) of the imaging sample [4]. In the case of a radially symmetric imaging sample, the B_1 field tends to focus in the centre of the phantom. This field focusing is responsible for a central brightening of the imaging sample [50].

3.2.1 Circularly Polarized B_1 Field

The B_1 field for an RF coil system can be broken down into transmit and receive fields, denoted as B_1^+ and B_1^-, respectively [4]. The B_1 field produced by a quadrature driven birdcage coil is the superposition of the B_1 fields from each port [4]. The transmit and receive fields can be expressed as:

$$\hat{\boldsymbol{B}}_{\boldsymbol{1}}^{+} = \left(\hat{\boldsymbol{B}}_{\boldsymbol{X}} + \jmath\hat{\boldsymbol{B}}_{\boldsymbol{Y}}\right)/2 \tag{35}$$

$$\hat{\boldsymbol{B}}_{\boldsymbol{1}}^{-} = \left(\hat{\boldsymbol{B}}_{\boldsymbol{X}} - \jmath\hat{\boldsymbol{B}}_{\boldsymbol{Y}}\right)^{*}/2 \tag{36}$$

where $\hat{\boldsymbol{B}}_{\boldsymbol{X}}$ is the B_1 field produced by the in-phase port and $\hat{\boldsymbol{B}}_{\boldsymbol{Y}}$ is the B_1 field produced by the quadrature port [23].

3.2.2 B_1 Mapping

B_1 mapping is the name given to the technique used to image the B_1 field in an imaging sample. The double-angle method (DAM) is one method used to map the B_1 field [51–53]. In the double-angle method, intensity maps (images) are acquired using two different flip angles: α and 2α. Since theoretically the image intensity (I), which is the transverse component of the magnetization (M_0), will be related to the flip angle (θ) via

$$I = M_0 \sin(\theta) \tag{37}$$

and the trigonometric identity $\sin(2\alpha) = 2\sin(\alpha)\cos(\alpha)$ can be used to relate α to 2α, a ratio of intensities from two images can be used to calculate the flip angle α:

$$\frac{I_{2\alpha}}{I_\alpha} = \frac{2M_0\sin(\alpha)\cos(\alpha)}{M_0\sin(\alpha)} = 2\cos(\alpha) \tag{38}$$

and solving for α results in the following relationship:

$$\alpha = \cos^{-1}\left(\frac{I_{2\alpha}}{2I_\alpha}\right) \tag{39}$$

where I_1 and I_2 are the pixel intensities of the images acquired using α and 2α flip angles, respectively. Mapping the B_1 field becomes increasingly important at high B_0 field as the B_1 field becomes increasingly inhomogeneous.

It should be noted that the B_1 mapping and the B_1 field discussed in this work refer to the transmit B_1 field, or B_1^+. Signal Intensity (I) can be expressed simplistically in terms of magnetization and flip angle as shown in equation 37. Magnetization depends on the proton density (ρ) in a particular region of a sample and the amount of signal this magnetization induces depends on the receive coil sensitivity, or receive B_1 field (B_1^-), in that region of the sample. Furthermore, as discussed in §1.4.2, the flip angle can be expressed in terms of gyromagnetic ratio (γ), RF pulse duration (τ), and a scaling factor (V) [23, 51]. This proportionality can be expressed as:

$$I \propto \rho|\hat{\boldsymbol{B}}_{\mathbf{1}}^-|\sin\left(V\gamma|\hat{\boldsymbol{B}}_{\mathbf{1}}^+|\tau\right) \tag{40}$$

In a ratio of intensity maps both acquired with the same coil and setup, it becomes apparent that the B_1^- factor (among others) drops out of the equation. Because of this fact, the DAM of B_1 mapping produces B_1^+ maps. The B_1^- field can usually be disregarded, however if the receive field is sufficiently low, the SNR of intensity maps will also be low. As such, B_1 maps will become noisy. Thresholding images prior to B_1 map calculation supresses noisy regions. Unless otherwise specified, when the B_1 field is discussed in this chapter, it is the B_1^+ field that is being discussed.

3.2.3 B_1 Shimming

The modification of the RF setup to achieve B_1 homogeneity is referred to as B_1 shimming [50]. The name B_1 shimming comes from a related concept called B_0 shimming where iron shims were used to modify the B_0 field (passive shimming) and improve B_0 field homogeneity. In the same way, B_1 shimming is used to improve the homogeneity of the B_1 field.

A wide variety of techniques have been employed in the area of B_1 shimming. Shimming can be achieved simply by using a high permittivity dielectric pad pressed against the imaging sample to modify the interference pattern [54]. A more elaborate method is to transmit simultaneously via multiple coils such as a surface coil and volume coil [55]. The most common approach, however, employs a multiple port transmit coil and multiple transmit channels. By understanding the influence of each channel on the B_1 field, homogeneity of the field can be optimized by combining port excitations in magnitude and phase. Practically, this is done by exciting each port using an individual RF pulse which is customized in terms of amplitude and phase.

3.2.4 Hardware

MRI system Although the Varian INOVA console used on the 4.7 T system has two RF transmit channels, the second channel is not implemented in current pulse sequences. Since the primary focus of this thesis is on RF hardware development rather than pulse programming, the objective of this project was to develop a simple method of B_1 shimming that involved only a single transmit channel and would provide a straightforward solution for researchers to improve B_1 homogeneity in their experiments.
The 4.7 T system has two transmit channels, four receive channels, and the following RF coils available [56]:

- volume head transmit & receive "TORO" (proton)
- 4-channel receive insert "PulseTeq 4-element array" (proton)
- MRII volume head transmit & receive
- MRII 4 channel receive insert "flex coil" (proton)
- knee (proton & sodium)
- head transmit & receive (sodium)

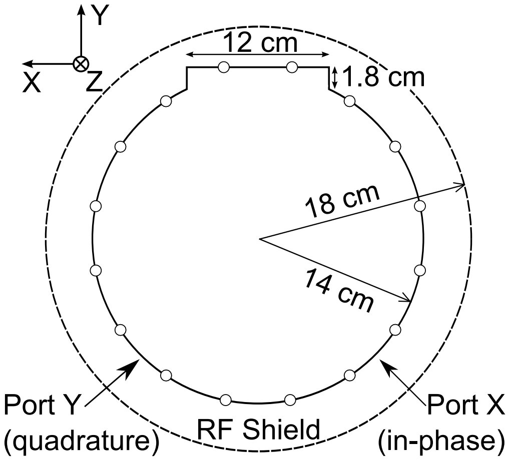

Figure 19: TORO birdcage coil cross-sectional view showing rung positions (circles), port locations, and size and position of the notch.

Transmit Coil The current proton birdcage RF coil available for the 4.7 T system is the aforementioned TORO coil [57]. It is an asymmetric 16-rung two-port quadrature driven band-pass birdcage coil. This coil is commonly referred to as the TORO (Transmit Only Receive Only) coil and is manufactured by XL Resonance (now XLR Imaging Inc., London, Ontario, Canada). While geometrically symmetric about the Y-axis (when positioned on the patient bed in the magnet bore), an asymmetry exists about the X-axis in the form of a slot, or notch, in the top of the cylindrical head coil where a quadrature surface coil or mirror can be mounted in front of the patient's face. As a result, two rungs deviate from the cylindrical arrangement of the other rungs and are a greater distance from coil center than other rungs. A cross-sectional view of the coil with the rung positions is depicted in figure 19. The entire coil is encompassed by an open-ended cylindrical RF shield with a radius of 18 cm and length of 38 cm. The cylindrical portion of the birdcage coil structure has a radius of 14 cm and length of 27 cm. The coil is not centred length-wise in the RF shield and is shifted from the centre by 1.5 cm. Rungs are 24.5 cm long and 1.27 cm (1/2 inch) wide. End rings are likewise 1.27 cm wide. Power is coupled to the coil at -45° and 45° from the bottom which is symmetrical about the Y-axis (figure 19). This is probably done due to the symmetry of the human head about the Y-axis [58].

Quadrature Hybrid The TORO coil is driven by a quadrature hybrid with a specified bandwidth of 128 MHz to 200 MHz. The measured coupling to the in-phase and quadrature ports at 200 MHz is approximately -3 dB. The quadrature (0°) port is preferentially coupled power when far from the centre frequency. Isolation (power coupled to the receive (RX) port) is in excess of 30 dB across the bandwidth of the device. All ports are closely matched to 50 Ω. Two equal length coaxial cables carry the signals from the quadrature hybrid to the coil ports.

Receive Coil The PulseTeq 4-element array (Head Array Coil model 4028-3, PulseTeq Ltd., Surrey, UK) is a 200.4 MHz 4-channel surface array that fits inside the TORO coil. It is designed for proton brain imaging at 4.7 T and encloses the top of the human head with four irregularly shaped coil elements, two at the back of the head covering the left and right quadrants, and two at the front of the head covering the left and right quadrants. The front two elements detach as a single unit from the coil base to ease access for the patient. Coil preamplifiers, bias tees, and tune/detune controls are integrated into the device. There are two sets of preamplifiers, one set on the coil and the other outside the magnet bore at the coil interface to the rest of the system. Contrary to the performance specified in [59], SNR per-

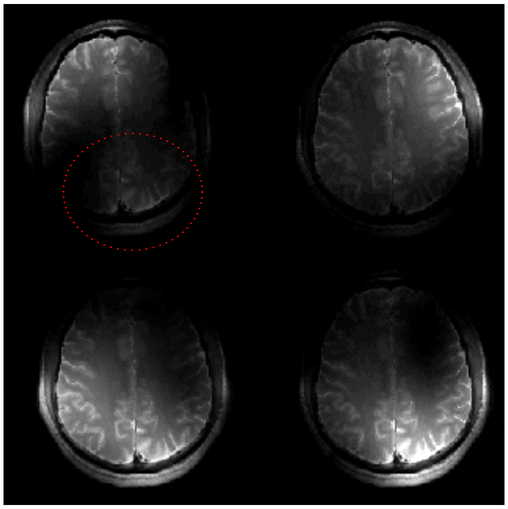

Figure 20: FSE Images of a human head from each coil of the PulseTeq 4-element array demonstrating coupling on the top left element (indicated by dotted circle) and reduced SNR from the top two elements. Images are normalized according to noise arrays from each element.

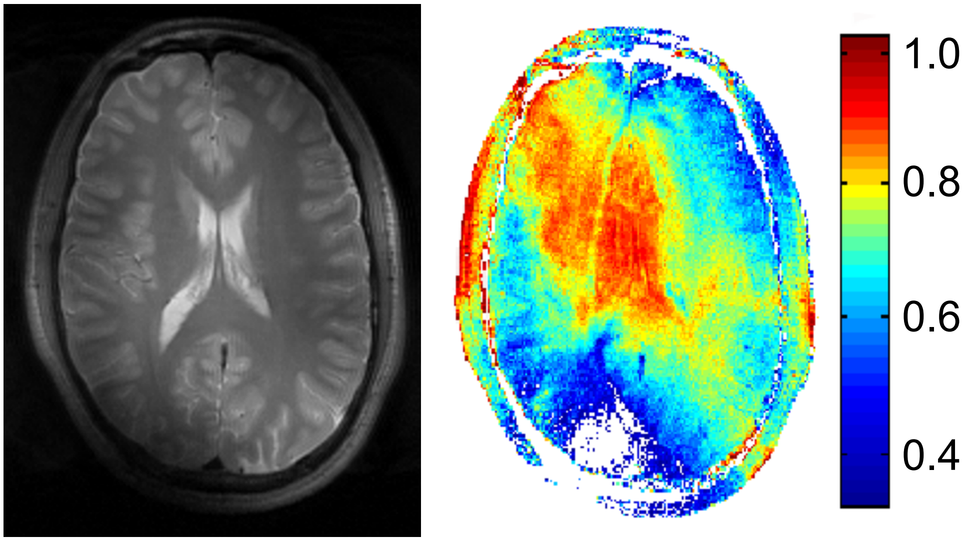

(a)

(b)

Figure 21: (a) An example of image shading in a human brain MRI as a result of B_1 inhomogeneity. (b) A B_1 map inside the human brain for an MRI using the TORO coil for transmit and PulseTeq 4-element array for receive.

formance of the coil elements of the array differ from one another as shown in figure 20. The top left element couples to the bottom right element and the top two elements produce lower SNR than the bottom elements.

3.2.5 Motivation

The asymmetric TORO birdcage coil suffers B_1 inhomogeneity which is apparent in images acquired using this coil. In a typical brain MRI, the B_1 field distribution results in signal loss to the upper right and/or bottom left of human head images (Figure 21a). This is seen as image shading. Regions of dark signal can be seen which are not reflected by the construction of the imaging phantom or anatomy of the human head.

Because the second transmit channel is not used on the 4.7T console, an RF shimming solution was attempted using only a single transmit channel. The objective was to develop a hardware solution which would achieve improved B_1 homogeneity without the need to take coils out of service to make extensive modifications and adjustments (as they are used on a daily basis by researchers). Simple phase shifting was attempted and the results were analyzed in order to understand the behavior and shape of the observed B_1 field.

The most widely used method for B_1 shimming involves altering the phase and amplitude of the RF pulse to each port [5, 6, 60]. In a single transmit scenario, any modifications to the RF pulse must happen after it has been split by the quadrature hybrid and prior to arriving at the transmit coil. The phase delay imposed by the quadrature hybrid is a fixed 90°, and this phase delay is usually intentionally maintained by using equal length coaxial cables between the quadrature hybrid and the coil. If, however, the coaxial cable lengths are different, the phase will be shifted away from quadrature. Phase shifting was therefore achieved simply by increasing or decreasing the relative electrical length of the coaxial cable on the quadrature port relative to the in-phase port by adding varying coaxial cable lengths.

All experiments were conducted using the TORO coil in transmit only mode and the Pulseteq 4-element array for receive. The receive array was aligned with iso-centre using the notch provided on the coil which is 85 mm from the top and bottom extent of the coil elements. Each B_1 map was calculated in MATLAB using the double-angle method (DAM) with data acquired from two fast spin-echo (FSE) proton density weighted sequences using flip angles of 60° and 120° (TR/TE = 7000/43 ms). Electrical characteristics (S-parameters and phase delay) were measured using a combination spectrum and network analyzer (HP 4396A with Agilent 85046A S-parameter Test Set).

3.3 Phantoms for Phase Shifting Experiments

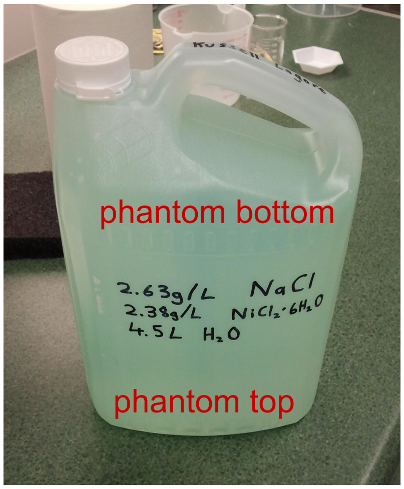

Figure 22: Phase Shift Phantom for phase shifting experiments. The top of the phantom refers to the portion which is oriented towards +Z along the magnet bore, and the bottom is towards -Z.

Three phantoms were used in experimentation. The first of these phantoms is a 7.3 L SIEMENS Large Plastic Bottle phantom with a per 1000g H_2O solution of 1.24g $NiSO_4$ x 6·H_2O and 2.62g NaCl. This phantom is a cylindrical plastic bottle with a radius of 8 cm and length of 37 cm.

The second phantom is a small cylindrical Silicone transformer oil phantom (ST50, Clearco Products Co., Inc., Bensalem, PA, USA) with a radius of 7 cm and height of 20 cm.

The third phantom (referred to as the Phase Shift Phantom) is a self-built asymmetric phantom, used to explore the effects of phase shifting without the need to do long experiments with volunteers. Since the human head is somewhat elliptical, a radially asymmetric phantom was needed to replicate the properties of the human head better than the axially symmetric phantoms mentioned previously. The phantom was a generic plastic jug filled with a solution that replicates the dielectric properties of the human body (figure 22). The jug is 19.5 cm by 12.5 cm at its base and 26.5 cm high. The solution used contains 2.63 g/L NaCl and 2.38 g/L $NiCl_2$·6H_2O in 4.5 L H_2O (distilled) [61]. Using conductance values for $NiCl_2$ from [62] and

NaCl from [63], the conductivity of the phantom can be calculated using the formula provided by [64]. The calculated conductivity of the phantom is 0.72 S/m which is within the range of conductivities of tissues in the human head [65–67].

3.4 RF Hardware Port Loading

When the TORO coil is being used in transmit-only mode, common practice among researchers in the research centre has been to leave the receive port of the quadrature hybrid disconnected. This is not the intended connection of the quadrature hybrid, however, and it is likely that this is done routinely due to the lack of 50 Ω loads with acceptable power ratings within the magnet room. Any unused port should be terminated using a 50 Ω load to prevent uncontrolled reflections that would affect phase and amplitude at the drive ports. Normally reflected power from the transmit coil is recombined at the receive port of the quadrature hybrid and absorbed by the load connected to this port. In the absence of a load, this reflected power has nowhere to go. An unterminated port can potentially affect the performance of the device (whether it be a coil or quadrature hybrid) or result in RF power being reflected back to the power amplifier. The effect of port loading of the quadrature hybrid and transmit coil on B_1 field and electrical parameters is explored in this section.

3.4.1 B_1 Field Variation

In order to study the effect of loaded or unloaded ports on the B_1 field, B_1 maps were acquired with a 50 Ω load resistor (TERMALINE 8402, Bird Technologies, Solon, Ohio, USA) used to terminate unused ports. This load, which was located outside the magnet room, was connected via an RG-223 coaxial cable routed through a waveguide into the magnet room. This load is power rated to 600 W continuous wave [68]. This is more than adequate, considering that power is attenuated along the coaxial cable and RF transmit power for MRI pulse sequences has a small duty cycle. Experiments were repeated with the load disconnected from unused ports. Lastly, difference maps were calculated from the B_1 maps obtained with and without the load to determine the impact of port loading.

Quadrature Hybrid In order to determine the impact of having the receive port of the quadrature hybrid terminated in a 50 Ω load, B_1 maps were acquired in the typical way with that port of the quadrature hybrid open and with the port terminated by a 50 Ω load.

In all cases, B_1 peak intensity increased by 10% when the quadrature hybrid was properly terminated. However, this B_1 field intensity change was not constant across the imaging sample. When the receive port was left open, B_1 field distribution spread out. Peaks were reduced and the periphery saw increases in flip angle. Difference maps were calculated from the B_1 maps when the receive port of the quadrature hybrid was loaded and unloaded. These B_1 and difference maps are shown in figure 23. Distribution of the B_1 field was impacted by port loading as well. Experiments on the TORO coil, below, show that this is due to a change in B_1 field contributed by each port due to the impedance match seen at the input ports of the coil.

Transmit Coil The TORO coil was linearly excited by connecting only the in-phase port (with the quadrature port left unused) and then only the quadrature port (with the in-phase port left unused). While acquiring B_1 maps of the in-phase and quadrature ports, the effect of loading the unused port was explored. B_1 maps were acquired both with and without the unused birdcage port loaded and the maps were compared.

When the coil was excited via the in-phase port, B_1 field magnitude increased in the centre of the imaging sample when the quadrature port was terminated with a 50 Ω load. This demonstrates that the load impedance on the quadrature port has an impact on the B_1 field produced by the in-phase port.

In contrast, when the coil was excited via the quadrature port, B_1 field magnitude decreased in the centre of the imaging sample as a consequence of terminating the in-phase port with a 50 Ω load. Higher B_1 field intensity was encountered with the in-phase port left unloaded. This demonstrates that the load impedance on the in-phase port has an impact on the B_1 field produced by the quadrature port.

Resulting B_1 maps and difference maps are shown in figure 23. Electrical measurements of the hardware help explain these results.

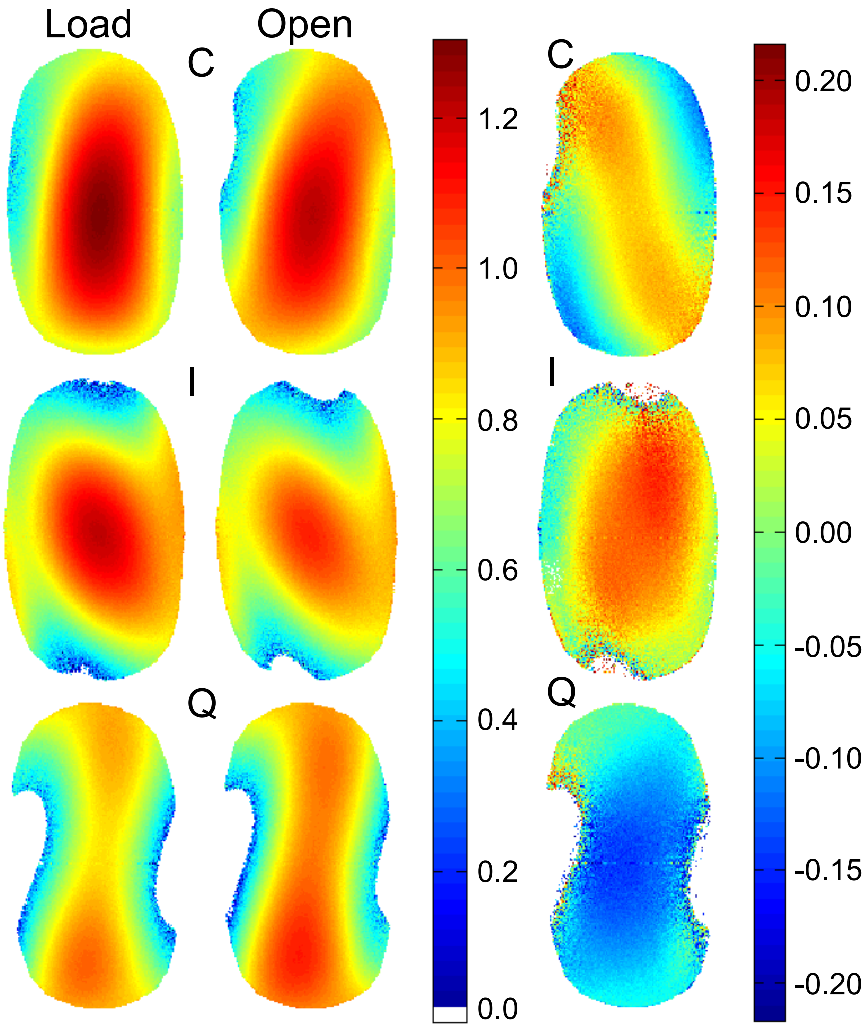

(a) (b)

Figure 23: (a) B_1 maps of the circularly polarized coil (C) when the RX port of the quadrature hybrid is loaded (left) or open (right) and the linearly polarized transmit coil (I or Q) when the opposite port (Q or I, respectively) is either loaded (left) or open (right). (b) B_1 maps of the difference between the B_1 maps for the loaded B_1 minus open B_1 in (a). Map values are normalized by the target excitation flip angle ($\alpha = 60°$).

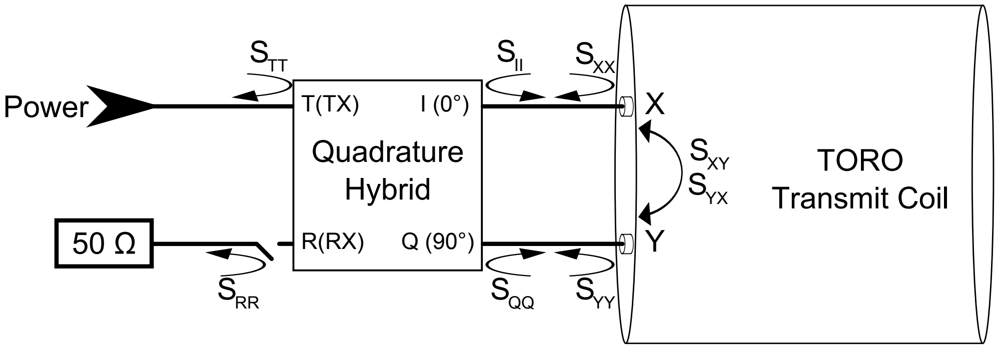

Figure 24: Block diagram of the transmit coil (TORO) and quadrature hybrid as well as some of the S-parameters (transmission parameters of the quadrature hybrid excluded to prevent clutter).

3.4.2 Electrical Measurements

In order to make sense of the B_1 field results above in §3.4.1, the quadrature hybrid and transmit coil were measured on the network analyzer using an S-parameter test set. It should be noted that S-parameter measurements conducted below, with some ports not matched, do not yield true S-parameters since S-parameters are defined for matched ports. Consequently, the measured parameters are described as coupling coefficients (for S_{ij} parameters) and reflection coefficients (for S_{ii} parameters).

Quadrature Hybrid Electrical parameters of the quadrature hybrid were measured in different circumstances. These measurements were done while the receive port (R) was both open and matched (table 6). The coupling to the quadrature port (S_{QT}) and in-phase port (S_{IT}) were measured while the port not being measured (I or Q, respectively) was connected to the TORO coil (figure 24). The reflection coefficients at all the ports of the quadrature hybrid (S_{TT}, S_{RR}, S_{II}, and S_{QQ}) were also measured.

Regardless of port loading, power is divided unevenly between the I and Q ports. The forward coupling coefficient for port Q (S_{QT}) was consistently higher than for port I (S_{IT}) by a ratio (Q/I) of 1.03 to 1.08. When I and Q are matched but the RX port is open there is an 18.1% power imbalance in favor of port Q. The phase shift between the ports is within a few degrees of 90° for all conditions. The phase drifted randomly, varying by 2.5° to 4° over the course of one minute. As such, measurement error is greater than the phase differences measured. Results are summarized in table 6.

Transmit Coil In addition to the quadrature hybrid, S-parameters of the transmit (TORO) coil were measured while the coil was loaded by the receive coil and phantom and was at iso-centre within the magnet bore. Long cables were run into the magnet room and the network analyzer was calibrated using

I, Q	**TORO**		**50Ω**	
RX	**OPEN**	**50Ω**	**OPEN**	**50Ω**
S_{TT}	-20 dB	-20 dB	-30 dB	-30 dB
S_{RR}	—	-22 dB	—	-30 dB
S_{II}	-5.5 dB	-30 dB	-5.8 dB	-30 dB
S_{QQ}	-7.0 dB	-30 dB	-7.4 dB	-49 dB
S_{TR}	—	-7.5 dB	—	-30 dB
S_{TI}	$0.74\angle -36^\circ$	$0.7\angle -36^\circ$	$0.76\angle -34^\circ$	$0.71\angle -36^\circ$
S_{IT}	$0.68\angle -38^\circ$		$0.69\angle -36^\circ$	
S_{TQ}	$0.62\angle -127^\circ$	$0.72\angle -126^\circ$	$0.68\angle -128^\circ$	$0.74\angle -128^\circ$
S_{QT}	$0.70\angle -126^\circ$		$0.75\angle -128^\circ$	
$\Delta\phi$	91° / 88°	90°	94° / 92°	92°
I/Q	1.19 / 0.97	0.97	1.12 / 0.92	0.96

Table 6: Coupling and reflection coefficients of the quadrature hybrid when the TORO coil is connected to the I and Q ports (left) and when the I and Q ports are terminated by 50 Ω (right). Additionally, separate sets of parameters were collected for the condition that the RX port is left open or terminated by 50 Ω. Measurements were performed at 200.44 MHz on the bench.

a full two-port SOLT (Short, Open, Load, Thru) calibration.

S_{XX}	$0.57\angle 93^\circ$ (-4.9 dB)
S_{XY}	$0.27\angle -20^\circ$ (-11.4 dB)
S_{YX}	
S_{YY}	$0.59\angle 83^\circ$ (-4.9 dB)

Table 7: In-bore measured S-parameters for the TORO transmit coil on in-phase (X) and quadrature (Y) ports.

The S-parameters of the transmit coil measured in the bore indicate poor performance (table 7). The coil resonates at 200.9 MHz instead of 200.1 MHz. The coil ports are not well matched and reflect about one third of the power delivered to them. Lastly, the ports exhibit strong coupling so some of the power delivered to one port is simply coupled to the opposite port with a phase that is not controlled by the hybrid rather than dissipated in the coil. In-bore measurements can be replicated on the bench via careful positioning of the loading phantom.

3.4.3 Discussion

Taken together, the transmit coil and quadrature hybrid present a complex system of interacting devices. Power is coupled to the in-phase and quadrature ports of the quadrature hybrid unequally. One third of this power is reflected back towards the quadrature hybrid due to the poor match on the transmit coil. Due to poor decoupling between the ports of the coil, the loading on one port influences the B_1 map of the excited port, as determined experimentally (figure 23) by linearly exciting the coil while the unused port is loaded and unloaded.

If the quadrature hybrid is properly loaded on its RX port, the I and Q ports of the quadrature hybrid are matched to 50 Ω, and any power that is reflected from the transmit coil is dissipated in the load on the RX port. If, however, the RX port is left open, the I and Q ports become reflective and power reflected by the transmit coil back to the quadrature hybrid is reflected again towards the transmit coil.

For the case where the RX port is open, power which reflects from the coil back into the quadrature hybrid is sent back to the power amplifier. The power amplifier on the 4.7 T Varian INOVA MRI system does not have a circulator which would normally protect the power amplifier. Instead, only a fault switch exists to shut down the system if the reflected power is too high. By not loading the RX port on the quadrature hybrid, the power amplifier is at greater risk of damage. Damage to the power amplifier has not occurred as a result of leaving the RX port open, however. This is because, regardless of loading, the reflection coefficient of the TX port (S_{TT}) is always -20 dB or better. This is because the majority of the power reflected from the coil back to the quadrature hybrid is either dissipated in the load on the RX port (for the loaded case) or simply reflected back to the coil due to reflective I and Q ports (for the unloaded case).

3.5 Phase Shifting

3.5.1 Phase Shifting with Coaxial Adapters

To verify that phase shifting will affect the B_1 field, three preliminary experiments were run. The first experiment was run on the SIEMENS 7.3 L phantom. The second was run on the silicone oil phantom, and the third was run on a human volunteer. Because the TORO coil was not being used for receive, the receive port of the quadrature hybrid was left open. Ideally, this unused port should be terminated by a 50 Ω load to absorb any power reflected by the coil, but this was the standard practice among researchers at the centre and therefore this setup was used for consistency.

The coaxial cable length was altered through the use of BNC adapters after the quadrature hybrid to increase the coaxial cable length on one port and affect the phase difference. The phase delay of the combination of one female-female and one male-male BNC adapter was measured to be between 14.7° and 15.4°. Connected in series to the in-phase and then the quadrature port would produce phase shifts (relative to quadrature) of approximately -45°, -30°, -15°, 15°, 30°, and 45°. A positive value was defined as one that produces a phase delay of greater than 90° (quadrature) on the quadrature port. For all phase shifts, B_1 maps were acquired and compared to one another in terms of B_1 amplitude and homogeneity.

Phase shifting results from the silicone oil phantom indicate that a -45° phase shift produces a B_1 map with the greatest homogeneity (figure 25). At 0°, B_1 standard deviation was 5.5% to 6.7% over ten slices of the phantom. Standard deviation was 2.9% to 4.7% for the -45° phase shift. To put this in perspective, error between successive measurements in human imaging is 2.9% to 7.5%. The silicone oil phantom has low permittivity (from the manufacturer's datasheet, $\epsilon_r = 2.7$ at 25°C and 50 Hz) and the B_1 field in this phantom is indicative of the B_1 field of the unloaded transmit coil.

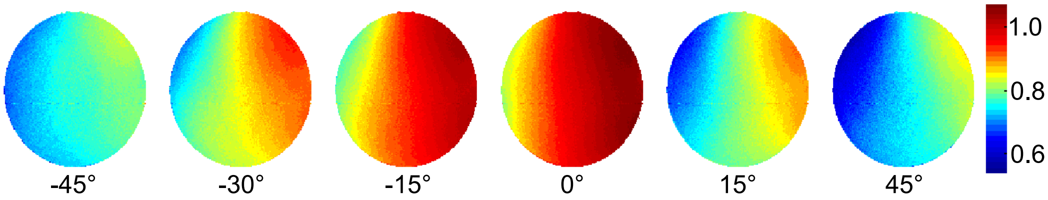

Figure 25: Silicone oil phantom B_1 maps for phase shifting via coaxial adapters. Some B_1 homogeneity exists even for a minimally loaded coil with a low permittivity phantom. Map values are normalized by the target excitation flip angle ($\alpha = 60°$).

Preliminary aqueous phantom phase shift results obtained using coaxial adapters showed an increase in B_1 magnitude for a phase shift of 30°. Positive phase shifts caused an increase in the B_1 magnitude while negative phase shifts caused a decrease in B_1 magnitude. The experiment was repeated on a human volunteer and the effect was even more pronounced (figure 26). For no phase shift, the B_1 field in the human head had a higher standard deviation, when compared to the silicone oil phantom, of 8.9% to 18.4%. As expected, there was greater inhomogeneity in the human head compared to the silicone oil phantom due to dielectric effects. Also, as expected, the effect of phase shifting is much different between these two very different imaging samples. The 30° phase shift, while increasing B_1 magnitude by a visually noticeable amount, improved homogeneity very little (standard deviation of 8.8% to 17.9%). Based on human head results, phase shifts in the region of 30° were explored more carefully in further experiments.

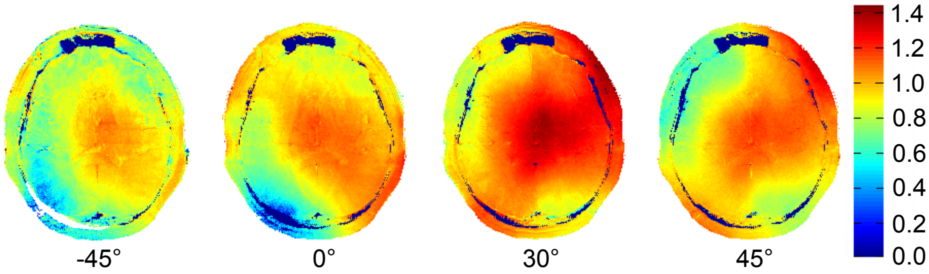

Figure 26: Preliminary phase shifting B_1 maps using coaxial adapters. Note the color bar range difference between this figure and figure 25. Map values are normalized by the target excitation flip angle ($\alpha = 60°$).

3.5.2 Phase Shifting with a Line Stretcher

l (mm)	$\Delta\phi$
101	95.0°
91	92.6°
81	90.1°
71	87.8°
61	85.4°
51	83.1°
41	80.9°
31	79.1°
21	76.6°
11	73.6°
0	71°

Table 8: Measurement of the phase delay ($\Delta\phi$) of the SR-15N at 200 MHz for increments in physical length (l).

Based on preliminary results, phase shifts around 30° were explored with phase increments smaller than before. Since smaller phase shifts were not achievable using coaxial adapters as before, a line stretcher (SR-15N, MICROLAB/FXR) was used. The SR-15N line stretcher is a telescoping variable length coaxial transmission line segment with a screw-down locking cap for fixing the length. It has a peak power rating of 5 kW and is thus capable of handling power from the power amplifier of the MRI system (4 kW). The SR-15N has N-type connectors which were adapted to female and male BNC connectors at either end of the device so it could be connected to other hardware. The SR-15N telescopes out to 101 mm. The phase delay was measured at increments of 10 mm from its shortest to longest length. Table 8 contains the results of these measurements. The length to phase relationship is linear (the measured values deviate somewhat due to measurement error). The adjustable range of the SR-15N is 24° at 200 MHz.

To compensate for the significant minimum phase delay (71°) introduced by the line-stretcher, it was paired with a length of RG-223 coaxial cable with a phase delay of 105.5° which would be connected on the other port. Lastly, a combination of one male-male and one female-female BNC adapter could be used to control the range of phase shifts by ±15°. Data was acquired from a SIEMENS 7.3L phantom and two human volunteers for phase shifts between 19.9° and 39.9°.

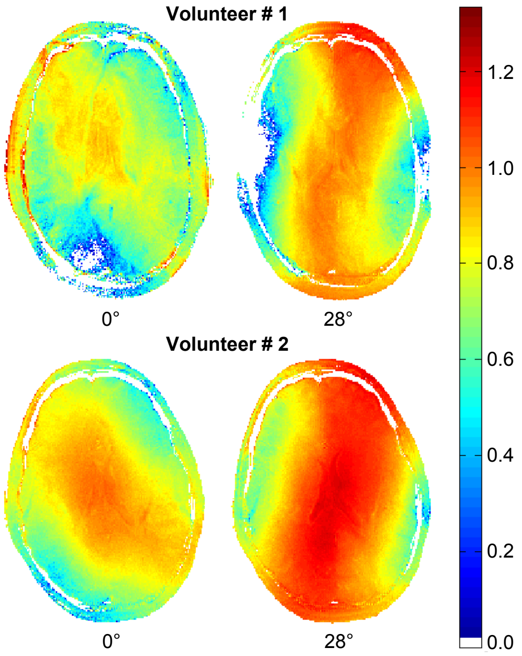

Figure 27: B_1 maps of two volunteers for no phase shift (0°) and a 28° phase shift using the line-stretcher to alter phase. Map values are normalized by the target excitation flip angle ($\alpha = 60°$).

The B_1 maps acquired from phantom experiments for a wide range of phase shifts were all similar. For this reason, difference maps and numerical methods were used to evaluate changes in B_1 maps for phase shift increments. The B_1 magnitude in some regions of the phantom increased by 5% but the field distribution did not change. Experiments on two human volunteers produced more dramatic changes. Results from these two experiments indicated that positive phase shifts between 20° and 40° increased the B_1 field magnitude relative to quadrature. The interference pattern was altered such that B_1 field was improved in some regions and degraded in others (figure 27). While not improving overall B_1 homogeneity, this could prove useful if the region of interest overlaps a region with low B_1 field or if more efficient use of RF power is needed, for instance, if an experiment is approaching SAR limits.

TORO Coil Failure and Repair After three experiments with human volunteers (one large phase increment and two small phase increment experiments), the TORO coil suffered a failure. Following a repair with re-tuning of the TORO coil, a further human volunteer was scanned using a setup identical to that described above. Figure 28 shows B_1 maps before and after the repair. The B_1 field pattern is altered as a result of the repair. Whereas previously the coil had regions of low B_1 in the bottom left and top right of the phantom, the present coil has regions of low B_1 in the top left and bottom right of the phantom.

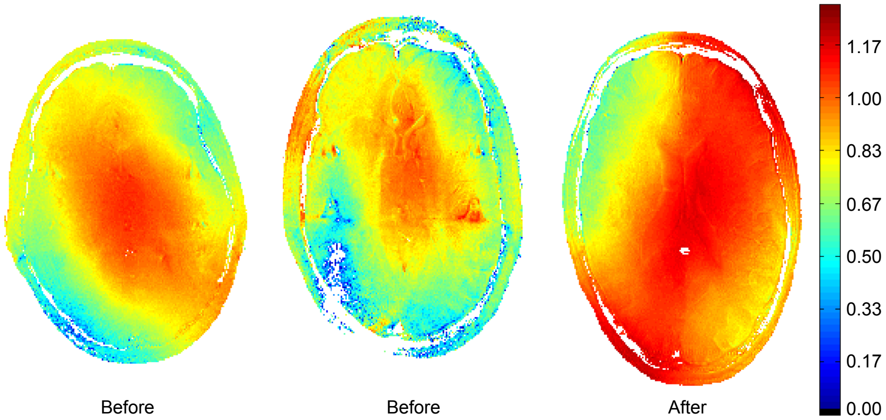

Figure 28: The two B_1 maps on the left are from two separate volunteers from before the TORO failure and subsequent repair. The right B_1 map is from after repairs and retuning of the TORO coil. Transmit power was not controlled for since individual volunteers required different transmit powers to achieve the same nominal flip angle. The coil is driven in quadrature (no phase shift) for this comparison. Map values are normalized by the target excitation flip angle ($\alpha = 60°$).

As mentioned, phase shifts between 20° and 40° were explored for a third volunteer. An additional phase shift experiment was run on the same volunteer using phase shifts between -4.7° and 19.3° to examine a broader range of small-increment phase shifts. Additionally, experiments were run on the self-built Phase Shift Phantom for phase shifts between -4.7° and 34°. After TORO coil repair, a region of low B_1 exists in the top left region of the human head. By visual inspection, the B_1 field looks better distributed for a phase shift between 24° and 28° (figure 29). The region of low B_1 is eliminated.

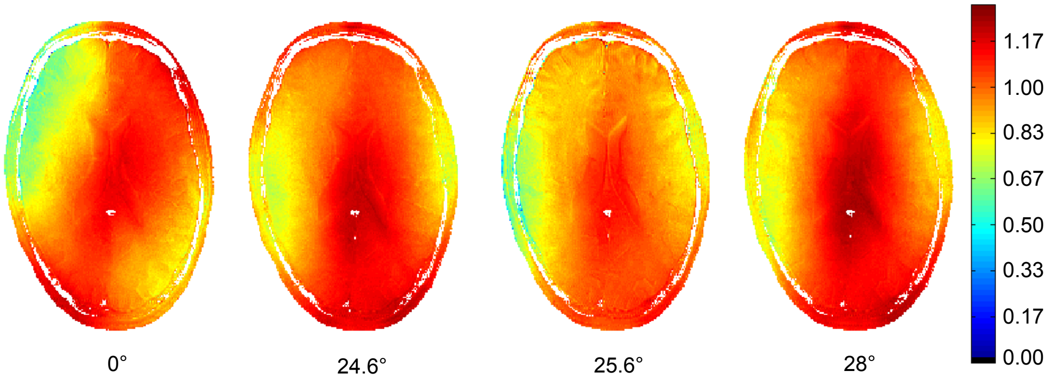

Figure 29: Phase shifting results for small increments on the repaired TORO coil. Shown is the B_1 map with no phase shift compared with three phase shifts with best B_1 field distribution. Map values are normalized by the target excitation flip angle ($\alpha = 60°$).

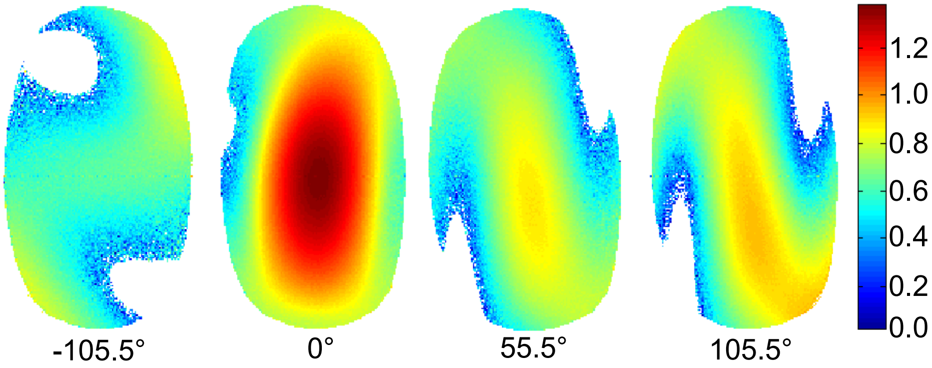

Figure 30: The resulting B_1 maps for -105.5°, 55.5°, and 105.5° phase shifts compared to quadrature (0°) for the Phase Shift Phantom. Map values are normalized by the target excitation flip angle ($\alpha = 60°$).

Phase shifting results from the Phase Shift Phantom did not match those from human trials. Phase shifts from -4.7° all the way up to 34° were explored and there was minimal change in the B_1 field. Difference maps did indicate a change, but it was not significant. Only for drastic phase shifts of 55.5° or ±105.5° (figure 30) did the B_1 map change substantially. Homogeneity did not improve but certain regions saw improvement in B_1 field homogeneity and/or intensity while other regions saw serious degradation.

3.6 Positioning of the Transmit Coil and Phantom

Researchers found that by rotating the TORO coil a quarter turn about the imaging sample, image quality improved. Furthermore, the TORO coil seemed to perform better in human head imaging when placed higher on the head (less of the coil enveloping the head). In order to determine why this was the case, the B_1 field was studied as the transmit coil was re-positioned relative to the receive coil and phantom (which were kept aligned with iso-centre). Additionally, the phantom was also repositioned relative to the transmit coil and the resulting B_1 field was studied. Repositioning the transmit coil during setup for an MRI on a human subject is practical as the time commitment is minimal if prior knowledge exists of what coil positions optimize the B_1 field.

3.6.1 Transmit Coil Rotation

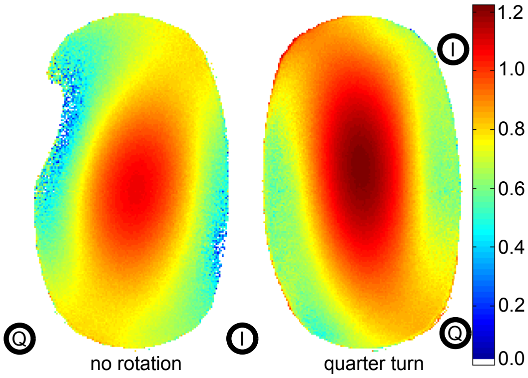

Figure 31: A comparison of the B_1 maps for the TORO coil with the notch positioned at the top (left) and with the notch rotated 90° counter-clockwise (right). Port positions are marked by circles with port letter (in-phase, I, and quadrature, Q). Map values are normalized by the target excitation flip angle ($\alpha = 60°$).

If the TORO coil were perfectly symmetrical (both in terms of geometry and electrical tuning) then coil rotation about the Z-axis should not affect observed image quality. For an asymmetric transmit B_1 field, a rotation of the coil is expected to translate into a rotation of the B_1 field. But since the B_1 field inhomogeneity is due mostly to wave interference in the imaging sample, rotating the coil will not translate to a direct rotation of the observed B_1 map for a radially asymmetric phantom. In this case, the regions of constructive and destructive interference will not simply rotate but change in a more complex way. As indicated by empirical results obtained by some reasearchers, this may prove useful for optimizing the B_1 field homogeneity for a specific area of interest. B_1 maps were acquired as before when the top notch of the coil was centred. Then B_1 maps were acquired again with the transmit coil rotated a quarter turn clockwise (when viewing from the +Z direction) such that the notch was centred over the left side of the imaging sample pictured in B_1 maps and images.

As the transmit coil was rotated about the Z-axis, the B_1 maps changed. As expected, the B_1 field could not be predicted by simply rotating the B_1 map because the interference pattern will change in a radially asymmetric phantom due to coil rotation. In the case of the post-repair TORO coil, the low B_1 field region in the upper left is eliminated by rotating the transmit coil left by one quarter turn (figure 31). Originally assumed to be due to coil coupling on the receive array, the low B_1 field region is more likely due to the transmit coil (however coupling cannot be completely ruled out). Calculating difference maps from the individual coil element images shows an increase in signal from the top left region due to rotation and a corresponding loss in signal for the bottom left coil element. It seems that there is a region of low B_1 field in the upper left region of the TORO coil. This region can be identified in the B_1 map of the rotated coil in the lower left corner of the phantom. By rotating the TORO coil a quarter turn, the ports are symmetric about the X-axis rather than the Y-axis, which is likely to change the interference pattern since the geometry has been altered.

3.6.2 Transmit Coil Translation

B_1 maps changed greatly from slice to slice with higher slices, which are closer to the coil centre, showing much greater homogeneity than lower slices which are near the edge of the coil (figure 32). This suggested that position along the Z-axis was important to axial B_1 homogeneity.

The TORO transmit coil has three markings along the outside body of the coil. The first, placed by the manufacturer, indicates the coil centre along the Z-axis. The other two markings indicate positioning to minimize power coupling to the human body during brain imaging. These markings were placed by researchers after experimentation and coil repairs. The first mark is 30 mm below coil centre and the second mark is another 30 mm below the first mark, a mere 70 mm from the bottom end ring (figure 33).

The B_1 field was studied when each of these markings coincided with magnet iso-centre. The phantom and receive array were not re-positioned. The B_0 field was shimmed each time after the coil was repositioned to ensure results were not biased by an inhomogeneous B_0.

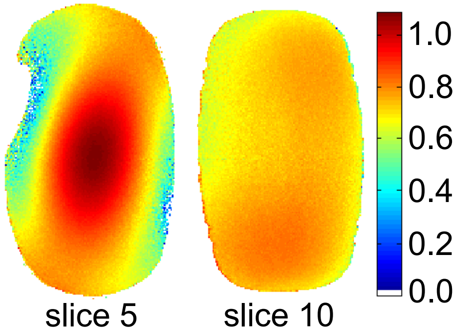

Figure 32: A comparison of the B_1 maps in slice 5 (left) and slice 10 (right) of the Phase Shift Phantom demonstrating the more homogeneous B_1 map in higher slices near the top of the coil. Slice 10 is a few millimeters from the top of the phantom while slice 5 is approximately 5 cm from the top. Map values are normalized by the target excitation flip angle ($\alpha = 60°$).

When the transmit coil was moved along the Z-axis relative to iso-centre and the receive coil with phantom were not moved, the B_1 field distribution changed minimally. There were obvious differences in B_1 intensity however. The B_1 map acquired when the coil centre was aligned with iso-centre is shown on the left in figure 34. This was used as a comparison point for B_1 maps acquired at the first and second markings (as indicated in figure 33 in §3.6).

By using the first marking to centre the coil, the transmit coil centre is placed 30 mm above iso-centre. Difference B_1 maps calculated from the B_1 maps for each coil position indicates a constant increase in B_1 intensity throughout the phantom which indicates that there is no change to the B_1 profile, but only the field strength. From inspection of the peak values for each B_1 map there is a 6% increase in B_1 values by centring the coil 30 mm above iso-centre.

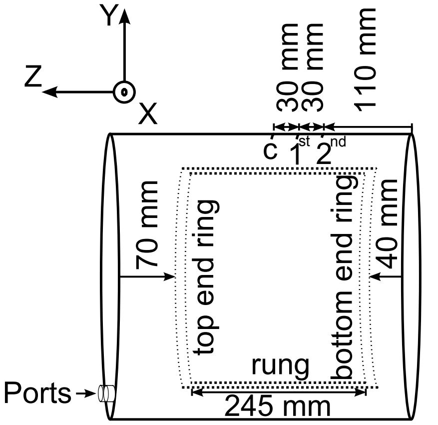

Figure 33: TORO birdcage coil lengthwise view showing positions of port connectors, rung length, end ring locations, and exterior markings: centre (c), first marking (1^{st}), and second marking (2^{nd}).

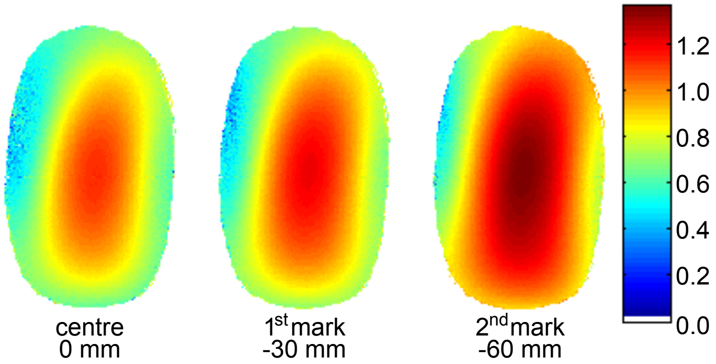

centre
0 mm

1st mark
-30 mm

2nd mark
-60 mm

Figure 34: A comparison of the B_1 maps for the TORO coil for varying positions along the Z-axis where centre refers to the coil centre being aligned with magnet iso-centre, 1^{st} mark refers to a mark 30 mm down the coil, and 2^{nd} mark refers to a mark a further 30 mm down the coil. B_1 distribution does not change, only the magnitude. Global scaling factors can be used on the B_1 maps to produce identical maps. Map values are normalized by the target excitation flip angle ($\alpha = 60°$).

For the second marking, which placed the transmit coil centre 60 mm above iso-centre (The bottom of the surface array elements approximately coincides with the bottom end ring of the transmit coil in this position), overall B_1 distribution did not change. For higher slices, the B_1 field is stronger. Difference B_1 maps verify that the increase in B_1 is constant throughout the phantom. Comparing peak values for B_1, there is a 20% increase in B_1 values by centring the coil 60 mm above iso-centre.

These results suggest that either the B_1 maps are being biased by the receive array instead of the transmit coil, or the dielectric effect is the dominant effect and not the inherent homogeneity of the transmit coil. To determine what the cause of this field distribution is, experiments were run with the phantom repositioned.

3.6.3 Translation of the Phantom

To disambiguate the interactions between the transmit coil, receive array, and phantom, B_1 maps were acquired with the phantom positioned such that it completely fills the receive array (the phantom top is flush with the top of the receive array which is 85 mm above iso-centre) and with the phantom shifted down the Z-axis by 30 mm. Again, in order to rule out B_0 homogeneity effects, the B_0 field was re-shimmed after the phantom was repositioned. The phantom was positioned 30 mm lower than usual such that the top of the phantom was aligned with iso-centre. B_1 maps were acquired with the slice position adjusted for this new setup. These B_1 maps were nearly identical. B_1 maps for lower slices were noisier due to the poor sensitivity far from the receive array elements. This is to be expected. Because B_1 maps didn't change when the phantom was positioned differently relative to the receive array, it is safe to assume that B_1 field distribution is affected mostly by dielectric effects, or so called field focusing [50], rather than by the inherent B_1 homogeneity of the unloaded transmit coil or the sensitivity of the receive array.

3.6.4 Transmit Power Efficiency

The coil efficiency expresses how much power entering the RF coil is converted into B_1 field. Transmit power efficiency, on the other hand, will refer to the amount of power transmitted by the power amplifier that is converted into B_1 field.

Transmit power efficiency changed as the TORO coil loading changed. This explains the change in B_1 magnitude as the coil was repositioned along the Z-axis. As the transmit coil position is moved up along the Z-axis, the position varies relative to the imaging sample and the coil is loaded to a lesser extent for the first and second marks relative to coil centre. The network analyzer was connected to the TX and RX ports of the quadrature hybrid which was in turn connected to the TORO transmit coil. As the phantom was slid in and out of the transmit coil, the power transmitted from the TX port to the RX port (S_{RT}) changed. In the case of the fully loaded coil (top of phantom is 20 cm inside, 16 cm from the bottom end ring), 18% of the power transmitted is dissipated in the 50 Ω load (connected to the RX port) and not in the transmit coil. When 11 cm of the phantom remains within the coil (70 mm beyond the bottom end ring, coinciding with the second mark), the power delivered to the RX port is at a minimum. This is the point of greatest transmit power efficiency since almost no power is deposited in the 50 Ω load (less than 1%).

3.7 Phantom Evaluation

As established in §3.6, the electromagnetic properties of the imaging sample have the greatest influence on B_1 field distribution so it is important to understand how a phantom used in experimentation behaves similar to, or differently from, the human head.

The self-built Phase Shift Phantom for phase shifting was meant to act as a substitute for a human head for long B_1 mapping experiments. The assumption made was that the B_1 field would behave similar to its behaviour in the human brain, and while not an exact analogue, would prove useful for studying phase shifting.

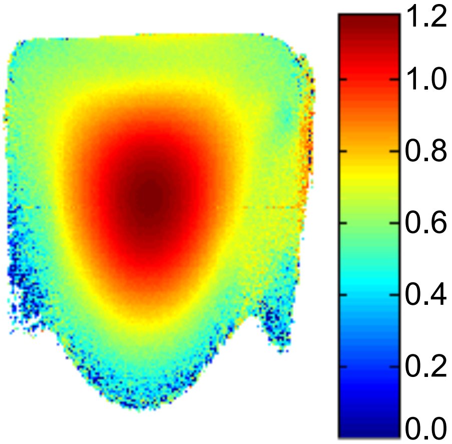

Figure 35: A sagittal B_1 map of an imaging phantom demonstrating the lack of field focusing near the top boundary of the phantom, possibly due to the longer wavelengths in this region. Map values are normalized by the target excitation flip angle ($\alpha = 60°$).

Results from §3.5.2 show a different field pattern when comparing the human brain to the phantom. While phase shifting produced visually noticeable changes to the B_1 field in the human brain for phase shifts between 0° and 30°, phase shifting in the phantom produced little noticeable change until the shift reached about 50°. While the Phase Shift Phantom does replicate the elliptical cross-section of the human head, it fails to take into account the ellipsoidal nature of the human head as the phantom is closer to an elliptical cylinder than an ellipsoid. Furthermore, the phantom uses an aqueous solution with the relative permittivity of water ($\epsilon_r = 81$) and a conductivity of the solution described in §3.3 ($\sigma = 0.72$ S/m). In contrast, the human head is made up of (among other things) blood ($\sigma = 1.28$ S/m, $\epsilon_r = 68$), white matter ($\sigma = 0.38$ S/m, $\epsilon_r = 47$), gray matter ($\sigma = 0.64$ S/m, $\epsilon_r = 65$), and cerebro-spinal fluid ($\sigma = 2.2$ S/m, $\epsilon_r = 77$) [65–67, 69]. While the average tissue conductivity in the head may indeed be close to the phantom conductivity, the phantom has a dielectric constant which is substantially higher. This higher dielectric constant will exacerbate the field focusing effect and B_1 shimming becomes more difficult.

One characteristic of the Phase Shift Phantom is that the B_1 field is more evenly distributed in high slices of the phantom while in lower slices, the field focusing effect dominates and there is an intensifying of B_1 in the centre of the phantom as illustrated by figure 32 in §3.6.2. As concluded in §3.6, this effect is due to the phantom and neither transmit nor receive coils.

Sagittal B_1 maps from an unrelated project demonstrate this field distribution (figure 35). Field focusing seems to also occur along the Z-axis. Since the human head has a rounded top rather than a (roughly) flat top, the field focusing effect along the Z-axis is likely to be different. The hot spot caused by field focusing is likely to occur lower in the human head and have a different shape than it does in a cylindrical phantom.

3.8 B_1 Maps of Individual Transmit Ports

3.8.1 Computing B_1 Field for the Circularly Polarized Coil

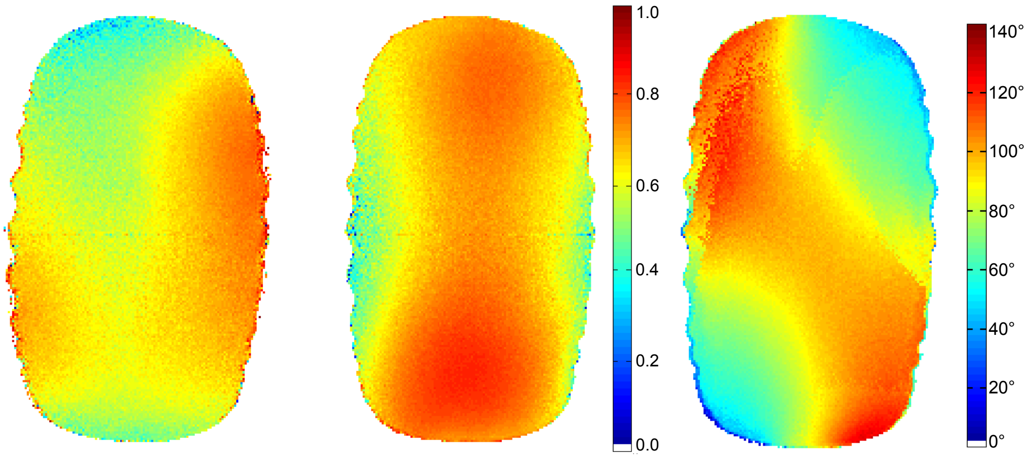

(a) (b)

Figure 36: (a) B_1 maps of the linearly driven transmit coil from the in-phase port (left) and quadrature port (right). Map values are normalized by the target excitation flip angle ($\alpha = 60°$). (b) The relative phase difference between the in-phase and quadrature ports.

In order to gain a deeper understanding of the behavior of the circularly polarized B_1 field and the changes that phase shifting cause, B_1 maps were obtained from the individual ports of the coil. After being power calibrated with both ports excited via the quadrature hybrid (with RX port properly terminated by 50 Ω), the quadrature hybrid was replaced with bulkhead BNC connectors joined together with a metal plate (to maintain the same grounding conditions in the circuit) and the transmit channel was connected to only the in-phase and then only the quadrature port while the load was connected to the unused port.

Complex data images for each receive array element were reconstructed and the phase computed for the in-phase and quadrature ports. These images were thresholded to remove noisy regions. The relative phase was computed by subtracting the phase of the quadrature port from the in-phase port. Phase was unwrapped on the relative phase map for each element and the relative phase images were combined on a pixel by pixel basis using a weighted average determined by the image intensities of each coil element. This method assumes there is no global offset of phase between element maps. In actuality, the offset between element maps could be as high as 10%, however for higher slices where less thresholding was required and data was more reliable, the phase offset between element maps was minimal. It is important to understand that the phase difference maps do contain some error and are not optimum reconstructions, however this error is not significant. Future efforts will involve optimizing this method.

B_1 fields resulting from phase shifting can be predicted from individual port B_1 maps from the linearly polarized transmit coil, which are combined with a phase shift. Since B_1 maps are magnitude maps and not complex valued, equation 35 from §3.2.1 can be modified to yield equation 41. The in-phase (X) port map remains unchanged, but the quadrature (Y) port map is multiplied by a relative phase matrix to create a complex valued map with phase values relative to the in-phase port.

$$\hat{\boldsymbol{B}}_{\mathbf{1}}^{+} = \left(a\boldsymbol{B_X} + \jmath b\boldsymbol{B_Y} e^{-\jmath(\boldsymbol{\phi}+\phi_o)}\right)/2 \tag{41}$$

Where $\boldsymbol{B_X}$ and $\boldsymbol{B_Y}$ are matricies of B_1 magnitude (figure 36a); a, b, and ϕ_o are real-value constants; and $\boldsymbol{\phi}$ is a matrix of phase values (figure 36b).

slice #	ϕ_o	a	b
1	2.5°	0.930	1.266
2	5.0°	1.005	1.222
3	0.0°	1.042	1.213
4	0.0°	1.100	1.154
5	-2.5°	1.023	1.265
6	0.0°	1.093	1.193
7	0.0°	1.042	1.247
8	0.0°	1.014	1.277
9	-2.5°	1.077	1.225
10	-2.5°	0.990	1.291
Avg	**0.0°**	**1.032**	**1.235**

Table 9: Phase offset and B_1 scaling factors that minimize the error between experimental B_1 maps and calculated B_1 maps for the circularly polarized coil.

The combination of port B_1 maps resulted in a computed circularly polarized B_1 field. It was compared against the experimental B_1 map for the circularly polarized coil using a difference map. The error was minimized by adjusting three parameters to determine the phase offset between the ports as well as the contribution of each port. This was used to verify that hardware changes actually caused the intended effect in the B_1 field.

The B_1 map computed from the individual port maps very closely matched the B_1 map acquired using the quadrature hybrid (circularly polarized coil) (figure 38). The phase offset (ϕ_o) and scaling factors (a and b), defined in equation 41, that minimized the error for each of ten slices are shown in table 9. The scaling factor for the quadrature port (b) was 19.7% greater than for the in-phase port (a). This is likely due to the elliptical, rather than linear, polarization of the transmit coil when it is driven from a single port only. Since the ports are symmetric about the Y-axis, the direction of elliptical polarization (clockwise or counter-clockwise) will be opposite.

3.8.2 Elliptical Polarization

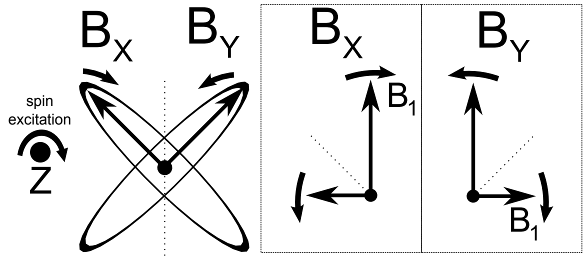

Figure 37: The left figure shows elliptical polarization from the in-phase (X, B_X) and quadrature (Y, B_Y) ports of the transmit coil with the counter-rotating vectors which describe each field (B_X and B_Y, respectively) to the right where the vector component that contributes to spin excitation is labeled as B_1. The counter-rotating vectors are not equal in magnitude, and the components responsible for excitation between port X and Y are also not equal. Orientation is as viewed from the +Z-axis.

Elliptical polarization as a result of a linear excitation can occur when the dimensions of the RF coil become large in comparison to the RF wavelength, as is the case at 4.7 T where transmit coil dimensions (diameter of 28 cm and length of 25 cm) are about one-fifth of the 1.5 m wavelength [70]. Elliptical polarization can alternatively occur for a linearly polarized coil if the imaging sample is conductive [71]. The Phase Shift Phantom has a conductivity of 0.72 S/m so this is likely to be the case. Elliptical polarization can be represented using counter-rotating vectors (as in §1.6.4) where the larger of the two vectors rotates in the direction of the elliptical polarization. Since only the clockwise rotating vector excites proton spins, one port will more effectively excite proton spins than the other due to its polarization. This is shown in figure 37.

At sufficiently low B_1 field strengths, the flip angles of the double angle-method enter a linear region and mapping B_1 is no longer possible. For this reason, there is increasingly less B_1 map data at lower slice numbers (further from coil centre). This is because thresholding is performed on intensity images prior to B_1 mapping to prevent noise from appearing in the B_1 maps. This causes large gaps in B_1 maps where there are regions of low B_1 intensity. Consequently, the reliability of the data in table 9 decreases with slice number. Because higher slices provided complete B_1 and phase difference maps of the imaging phantom, these slices were used to examine the phase difference and B_1 field contributions. There is persistently significant error along the edges of the computed B_1 maps, possibly due to the use of different threshold levels and masks.

3.8.3 Computing Optimum Phase Shift for B_1 Shimming

As noted in §3.6, the greatest influence on B_1 field distribution within the imaging sample is the dielectric effect. Despite the limitations of B_1 shimming on a volume coil described, it is still possible to do B_1 shimming in the human head due to the relatively weak field focusing compared to an aqueous phantom.

The Phase Shift Phantom was analyzed in a high slice where the B_1 field is well distributed. The computed B_1 map was examined for a variety of different values for a, b, and ϕ_o. A comparison was made between B_1 maps using the coefficients in table 9 and ideal coefficients ($a = b$, $\phi_o = 0$). The B_1 maps agreed to within a few percent, suggesting that the slight port imbalance does not affect the B_1 field too greatly.

The greatest influence on the B_1 field was the phase offset (ϕ_o). For this reason, the mean and standard deviation in the computed B_1 map was plotted as phase offset (ϕ_o) was varied from -180° to 180° for equation 41. A region-of-interest was was designated for these calculations and the calculations were done using this region-of-interest as well as without it (to determine whether results changed if B_1 optimization was restricted to a smaller region within the imaging sample). The mean was maximized in all slices for a phase offset of zero. The phase offset which minimized standard deviation was quite different from slice to slice and whether or not the region-of-interest was used. No solution for minimum standard deviation produced a B_1 map that was clearly optimal. Altering the phase offset between only two ports is limited in its usefulness to shim the B_1 field. In order to illustrate the impact of phase offset and determine how accurately a B_1 map of a particular phase shift can be predicted, experimental results from phase shifts of ±105.5° are compared to computed B_1 maps in figures 38d and 38e.

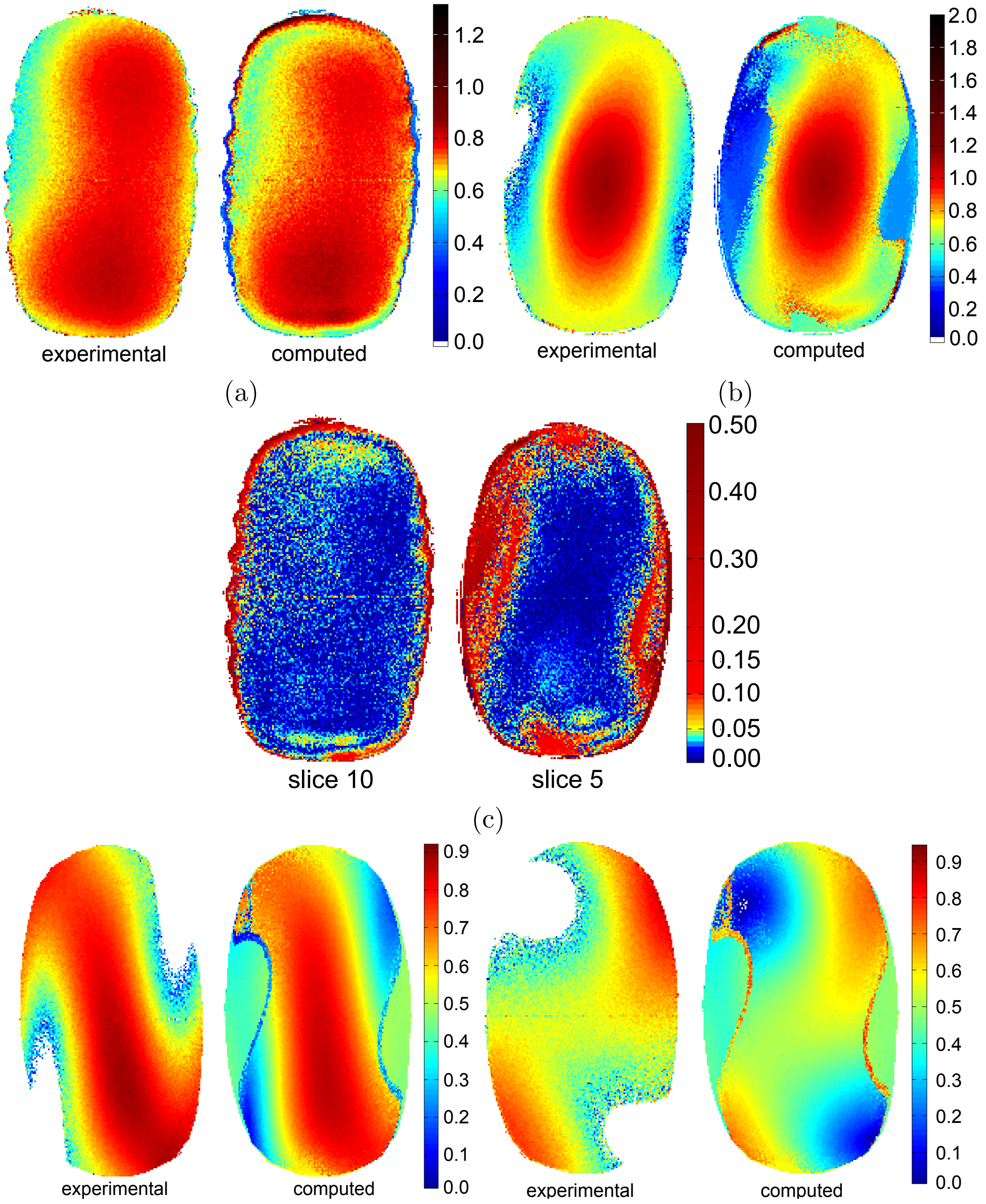

(a) (b)

(c)

(d) (e)

Figure 38: Comparison between the experimentally obtained B_1 map and the computed B_1 map of a circularly polarized transmit coil for (a) slice 10, and (b) slice 5. (c) Difference maps showing the error in the computed B_1 maps compared to experimental B_1 maps illustrating the poorer results for lower slices. Poorest computed results are at the edges of the phantom. Errors in excess of 0.5 are set to 0.5 so small error can be shown on this scale. (d) Comparison between the B_1 map of a phase shift of 105.5° and computed B_1 map with the phase offset parameter (ϕ_o) set to 105.5°. (e) The same comparison made for a phase shift and phase offset of -105.5°.

3.9 Current Limitations and Future Work

The B_1 homogeneity of the current system is limited both by the available hardware (RF coils and transmit channels) as well as the available software (pulse sequences).

The current TORO transmit coil is limited in terms of transmit power efficiency. More efficient use of RF power can be ensured by properly matching the transmit coil to the characteristic impedance to ensure minimal power is reflected from the ports of the coil. Since port matching can change with the load presented to the coil, the coil should be matched in the bore while loaded with a typical human head. Matching can be done manually if there are variable capacitors on the coil. One limitation to the TORO transmit coil is the lack of these variable capacitors. They were removed during repairs and never replaced. In practice, however, the coil is not tuned for each individual subject due to the time requirements. One possible direction for future work could be the implementation of L-section matching circuits with control circuitry capable of matching the ports automatically [72, 73].

The B_1 field within a phantom can be very different from that in the human head. For this reason, a phantom built to study the B_1 field for brain imaging must replicate both the shape and electromagnetic properties of the average human head [65]. Both conductivity and relative permittivity are important quantities to consider in the design of such a phantom.

Since phase shifting has such a significant effect on the B_1 field, it makes sense to expand on this work in the future. Altering the phase difference between the in-phase and quadrature ports offers one degree of freedom. If, however, the coil were to be driven from multiple ports, phase shifting would offer more degrees of freedom. Modern techniques which combine multiple transmit channels with variable phase and amplitude as well as complex pulse sequences are able to effectively improve B_1 homogeneity [60, 74]. Coil design for high field MRI is moving towards transmit arrays. These coils are no longer single structures such as the birdcage coil but are made up of individual coil elements which are tuned to the Larmor frequency and decoupled from one another. While these coils are usually built to be used in systems with multiple transmit channels, it is possible to employ such a coil with a single transmit channel. In a multiple port coil, the first port would be the in-phase ($0°$) port, while all other ports would have their phase adjusted after optimization experiments. For optimization experiments, a phantom like the one described above could be used. Port B_1 maps could be acquired as well as relative phase difference maps (where phase is relative to the in-phase port) and these maps could be combined while varying phase offset to find the optimal phase shift for each port. The single transmit channel used to drive the coil could be split evenly among the ports using a power divider or cascaded quadrature hybrids. The phase shift on each port that optimizes B_1 homogeneity could be hardwired into the coil downstream from the power divider. Additional hardware could even be employed (such as line-stretchers) to allow for further phase shift adjustments after the fact.

3.10 Conclusions

There is an asymmetry in the transmit coil which is a source of B_1 inhomogeneity. This is seen as changes in B_1 map due to coil rotation, which should not occur if the coil is symmetric and produces a symmetrical B_1 field. Consequently, rotating the transmit coil one quarter turn counter-clockwise (when viewed from the side of the magnet where the patient bed is located) about the axis of the magnet bore (Z-axis) improves the B_1 homogeneity. In specific, it improves B_1 intensity in the top left region of an elliptical imaging sample.

Greater transmit power efficiency was achieved by translating the coil along the axis of the magnet bore. If the coil centre was positioned 60 mm above magnet iso-centre, the B_1 field experienced a 20% increase in magnitude without suffering any measurable degradation in homogeneity. This coil positioning allows the same flip angle to be achieved using less power, thus decreasing SAR.

Phase shifting altered the B_1 field within the imaging sample. Phase shifts between 24° and 28° maximized B_1 field magnitude and altered the B_1 pattern, rotating regions of high and low B_1 intensity about the periphery of the imaging sample.

The B_1 field homogeneity was affected by the presence or absence of a 50 ohm load at the receive port of the quadrature hybrid. Peak B_1 values increased when the receive port was loaded, while B_1 homogeneity improved when the port was left open.

The change in B_1 field pattern as a result of phase shifting can be explained using a superposition of the individual port B_1 fields. Altering the phase offset between port B_1 maps resulted in a much more noticeable change in B_1 pattern than altering the magnitude of each port B_1 field. Most of the optimization to B_1 can be achieved by altering phase. Altering the phase difference between only two ports, however, offers only a single degree of freedom.

A number of strategies were developed to optimize the transmit power efficiency or B_1 homogeneity of the transmit coil. Best practices are as follows:

- Rotate the transmit coil counter-clockwise (viewed from the side with the patient bed) by a quarter-turn to improve B_1 field homogeneity.
- Phase delay the quadrature port on the transmit coil by 28° downstream of the quadrature hybrid to improve B_1 field magnitude and alter the field pattern.
- Leave the RX port on the quadrature hybrid unloaded for greater B_1 homogeneity, or
- load the RX port of the quadrature hybrid to achieve greater peak B_1 values.

- Align the transmit coil centre 60 mm above magnet iso-centre (small black mark on exterior of the coil) to improve B_1 field magnitude.

Transmit coil positioning is of greatest importance in optimizing the B_1 field in terms of homogeneity and transmit power efficiency. While phase shifting has a significant impact on B_1 field patterns, its ability to produce a homogeneous B_1 field is limited for a two port coil. Coil design remains an important area of innovation in the pursuit of B_1 field homogeneity.

4 Conclusion

Better image quality will always be a goal in high field magnetic resonance imaging research. This image quality depends not only on well-designed pulse sequences, but also on well-designed radio frequency (RF) hardware. Well-designed RF hardware offers improvement in terms of high signal-to-noise ratio (SNR) (which can allow for increased image acquisition speed or increased image resolution) and uniform contrast (which allows for anatomy to be accurately imaged).

4.1 Noise Figure of MRI Preamplifiers

4.1.1 Summary

High SNR can be achieved by increasing magnetic field strength of the MRI system. The consequence, however, is that measurement electronics (namely receive coil preamplifiers) will be subjected to stronger magnetic fields. Measurement electronics amplify the received NMR signal but also add noise to this signal. The noise added by measurement electronics, and the resulting loss in SNR is described by the noise figure. A measurement system to measure noise figure for MRI preamplifiers was developed. This measurement system was used to measure noise figure and available gain variation of MRI preamplifiers as preamplifiers were subjected to increasingly strong magnetic fields. This variation was studied as position was altered. In addition to noise figure, the noise parameters of MRI preamplifiers were determined through use of an electronically controlled tuning board.

4.1.2 Results and Conclusions

Noise figure and gain variation depends on both preamplifier orientation within a magnetic field as well as the strength of the magnetic field. Noise figure increases with increasing magnetic field while gain decreases with increasing field. These effects can be attributed to the Hall effect. Variation in noise figure and gain was measured for gallium arsenide, indium gallium phosphide, silicon, and silicon germanium. Gallium arsenide devices, while being capable of achieving very low noise figures, were the most susceptible to increasing magnetic field and saw large increases in noise figure and decreases in gain. However, these effects could be minimized or even eliminated through careful selection of orientation of the device relative to the magnetic field. In stark contrast to gallium arsenide, silicon germanium devices experienced no measurable variation in noise figure or gain as magnetic field strength increased. Orientation of the device had no effect on its performance within the field. This is likely due to the thin base of the silicon germanium bipolar transistor. Charge carriers are only acted on over a short distance and thus performance of the transistor does not degrade in fields up to 9.4 tesla.

Noise parameter results obtained with the developed noise figure measurement system and corresponding tuning board agreed well with manufacturer data and measurements from other sources. Noise parameters for the indium gallium phosphide and silicon preamplifiers are undesirable due to the high noise resistance of these devices. A high noise resistance translates into a large increase in noise figure for even a small mismatch in source impedance. Furthermore, these preamplifiers were found to have a relatively large minimum noise figure. In contrast, the gallium arsenide and silicon germanium devices were found to have a low minimum noise figure and small noise resistance. Low noise figure can be achieved even with a small mismatch in source impedance.

4.1.3 Future Work

Future work will involve implementation of RF switches to increase the level of automation in the measurement system and allow for faster measurements. This system, developed for the Department of Oncology, should be replicated at the Peter S. Allen MR Research Centre so researchers in the Department of Biomedical Engineering have a system with which they can characterize the noise figure of MRI preamplifiers. Beyond improvements to the measurement system, a low noise silicon germanium preamplifier should be developed with the source impedance matched to achieve low noise figure common to gallium arsenide devices. Current preamplifiers used at the research centre should be measured to ensure only devices with low noise figure are being used, and that they are being used properly (in the case of gallium arsenide, that the preamplifiers are being properly oriented relative to the magnetic field).

4.2 B_1 Shimming via Quadrature Phase Shifting

4.2.1 Summary

One consequence of moving to a higher magnetic field in MRI is an inhomogeneous radio frequency (B_1) field. The homogeneity of the B_1 field suffers in high field MRI due to the reduced RF wavelength at higher frequencies and the shortening effects of an imaging sample (which usually has a high relative permittivity) upon this wavelength. B_1 shimming techniques were employed on a quadrature-driven birdcage transmit coil to determine the best way to optimize field homogeneity.

4.2.2 Results and Conclusions

The unloaded asymmetric transmit coil had an asymmetric B_1 field, determined by imaging a low relative permittivity silicone oil phantom. A region of low B_1 field intensity exists in the top left region of the coil (as viewed from the side of the bore with the patient bed). As a result, rotating the transmit coil about the axis of the magnet bore and relative to the imaging phantom was able to alter the axial B_1 field homogeneity. Homogeneity was improved when the coil was rotated a quarter turn about the imaging phantom.

Increased transmit power efficiency was achieved by translating the transmit coil up along the axis of the magnet bore, leaving less of the imaging sample enveloped in the coil. When the coil centre was aligned 60 mm above the magnet iso-centre, transmit power efficiency improved by 20% with no degradation in B_1 field homogeneity.

The common practice among researchers at the research centre is to leave the unused receive port of the quadrature hybrid disconnected when the transmit coil is being used in transmit-only mode. Since the quadrature hybrid is intended to operate with all ports loaded, the effect of leaving a port disconnected was unknown. The B_1 field homogeneity was affected by the presence or absence of a load at the receive port of the quadrature hybrid. Peak B_1 values increased when the receive port was loaded, while B_1 homogeneity improved when the port was left open.

Phase shifting the quadrature port by 28° improved B_1 field intensity and rotated regions of low B_1 field around the periphery of the imaging sample. Homogeneity of the B_1 field was not significantly improved by phase shifting. This is likely a limitation of B_1 shimming on a two port coil. Better phase shifting results could be obtained for a transmit coil with a greater number of ports, as the degrees of freedom increase.

4.2.3 Future Work

The B_1 field observed is largely a consequence of the imaging sample and the B_1 homogeneity of the unloaded coil has a smaller impact. As such, to properly study the behavior of the B_1 field in human brain imaging, an imaging phantom must be constructed that accurately replicates both the geometry and dielectric properties of the human head.

Phase shifting on a quadrature driven birdcage coil was limited to a single degree of freedom. Phase shifting caused variations in the B_1 field pattern, but was insufficient to improve B_1 homogeneity. One possible future project involves development of a transmit array. A fixed phase shift could be hardwired for each port of this transmit array after the optimal phase shifts were computed using B_1 maps from the individual ports and phase difference maps from each port. These ports could be driven off a single transmit channel by including a power splitter in the transmit RF chain. A more homogeneous B_1 field excitation would likely be achievable due to the increased degrees of freedom. Furthermore, this would enable the use of a transmit array (typically developed for multiple transmit channels) on an MRI system that possesses only a single transmit channel.

4.3 RF Hardware in High Field MRI

It is hard to project how high field strength will get in high field MRI research, but as long as field strengths continue to increase, the pulse sequences and hardware of the MRI system will need to keep up with this increase. The RF subsystem is no exception to this, as this hardware will be subjected to ever increasing field strengths and be required to operate at ever increasing frequencies. There remains room for improvement in the B_1 shimming techniques presented in this work. The hope is that this will provide a starting point for future development of simple but effective B_1 shimming techniques on the 4.7 tesla MRI system. Preamplifiers, which have been characterized up to 9.4 tesla in this thesis, will probably continue to see variation in performance beyond 9.4 tesla. Even the silicon germanium devices, which show no variation up to 9.4 tesla, may suffer performance degradation at higher field strengths. A valuable extension of this work will be to continue characterizing MRI preamplifiers as new high field magnets become available so that researchers stay informed about the performance of their RF hardware in the magnet bore.

5 References

[1] M. Elmaolu and A. Çelik, "A Brief History of Magnetic Resonance Imaging," in *MRI Handbook*. Boston, MA: Springer US, 2012, pp. 3–6. [Online]. Available: http://www.springerlink.com/index/10.1007/978-1-4614-1096-6

[2] Z. Liang and P. Lauterbur, "Introduction," in *Principles of Magnetic Resonance Imaging*. Wiley - IEEE Press, Jan. 2000, vol. 104, ch. 1, pp. 1–8. [Online]. Available: http://ieeexplore.ieee.org/xpl/bkabstractplus.jsp?bkn=5264284

[3] J. T. Vaughan, M. Garwood, C. M. Collins, W. Liu, L. DelaBarre, G. Adriany, P. Andersen, H. Merkle, R. Goebel, M. B. Smith, and K. Ugurbil, "7T vs. 4T: RF power, homogeneity, and signal-to-noise comparison in head images." *Magnetic resonance in medicine*, vol. 46, no. 1, pp. 24–30, Jul. 2001. [Online]. Available: http://www.ncbi.nlm.nih.gov/pubmed/11443707

[4] G. Glover, C. Hayes, N. Pelc, W. Edelstein, O. Mueller, H. Hart, C. Hardy, M. O'Donnell, and W. Barber, "Comparison of linear and circular polarization for magnetic resonance imaging," *Journal of Magnetic Resonance (1969)*, vol. 64, no. 2, pp. 255–270, Sep. 1985. [Online]. Available: http://linkinghub.elsevier.com/retrieve/pii/002223648590349X

[5] L. Wald and E. Adalsteinsson, "Parallel transmit technology for high field MRI," *MAGNETOM Flash*, pp. 124–135, 2009. [Online]. Available: http://www.medical.siemens.com/siemens/

[6] U. Katscher, P. Börnert, C. Leussler, and J. S. van den Brink, "Transmit SENSE." *Magnetic resonance in medicine*, vol. 49, no. 1, pp. 144–50, Jan. 2003. [Online]. Available: http://www.ncbi.nlm.nih.gov/pubmed/12509830

[7] Z. Liang and P. Lauterbur, "Signal Generation and Detection," in *Principles of Magnetic Resonance Imaging*. Wiley - IEEE Press, 2000, ch. 3, pp. 57–105. [Online]. Available: http://ieeexplore.ieee.org/xpl/bkabstractplus.jsp?bkn=5264284

[8] M. L. Lipton, "Laying the foundation," in *Totally Accessible MRI*. New York: Springer, 2008, no. 1, ch. 1, pp. 3–18. [Online]. Available: http://link.springer.com/book/10.1007/978-0-387-48896-7/page/1

[9] J. Mispelter, M. Lupu, and A. Briguet, *NMR Probeheads for Biophysical and Biomedical Experiments: Theorectical Priciples and Practical Guidelines*. London, GBR: Imperial College Press.

[10] R. Salzer, "Magnetic Resonance Technology," in *Biomedical Imaging: Principles and Applications*. John Wiley & Sons, 2012, ch. 5. [Online]. Available: http://proquest.safaribooksonline.com/book/-/9781118271926

[11] D. I. Hoult and R. E. Richards, "The signal-to-noise ratio of the nuclear magnetic resonance experiment." *Journal of Magnetic Resonance*, vol. 213, no. 2, pp. 329–43, Dec. 2011. [Online]. Available: http://www.ncbi.nlm.nih.gov/pubmed/22152352

[12] M. L. Lipton, "Hardware , Especially Gradient Magnetic Fields," in *Totally Accessible MRI*. New York: Springer, 2008, ch. 5, pp. 47–72. [Online]. Available: http://link.springer.com/book/10.1007/978-0-387-48896-7/page/1

[13] ——, "Spatial Localization: Creating an Image," in *Totally Accessible MRI*. New York: Springer, 2008, ch. 6, pp. 75–100. [Online]. Available: http://link.springer.com/book/10.1007/978-0-387-48896-7/page/1

[14] H. Liebel, "High-Field Superconducting Magnets," in *High-Field MR Imaging*, J. Hennig and O. Speck, Eds. Springer, 2011, ch. 3, pp. 7–25.

[15] V. Kuperman, "Basic Principles of Nuclear Magnetic Resonance," in *Magnetic Resonance Imaging: Physical Principles and Applications*. San Diego: Academic Press, ch. 2, p. 12.

[16] W. A. Edelstein, G. H. Glover, C. J. Hardy, and R. W. Redington, "The intrinsic signal-to-noise ratio in NMR imaging." *Magnetic resonance in medicine*, vol. 3, no. 4, pp. 604–18, Aug. 1986. [Online]. Available: http://www.ncbi.nlm.nih.gov/pubmed/3747821

[17] A. G. Webb, "Radiofrequency Coils," in *High-Field MR Imaging*, J. Hennig and O. Speck, Eds. Heidelberg: Springer-Verlag Berlin, 2011, pp. 41–56.

[18] D. G. Norris, "High field human imaging," *Journal of magnetic resonance imaging : JMRI*, vol. 18, no. 5, pp. 519–29, Nov. 2003. [Online]. Available: http://www.ncbi.nlm.nih.gov/pubmed/14579394

[19] T. S. Ibrahim, R. Lee, B. A. Baertlein, A. Kangarlu, and P. M. L. Robitaille, "Dielectric Resonance in Ultra High Field MRI," *Proceedings of the 8th Annual Meeting of the International Society of Magnetic Resonance in Medicine*, vol. 8, p. 1681, 2000.

[20] C. A. Balanis, "Electrical Properties of Matter," in *Advanced Engineering Electromagnetics*, 1989, p. 57.

[21] D. K. Cheng, "Static Magnetic Fields," in *Field and Wave Electromagnetics*, 4th ed. Addison-Wesley Publishing Company, 1989, pp. 225–294.

[22] Q. X. Yang, J. Wang, X. Zhang, C. M. Collins, M. B. Smith, H. Liu, X.-H. Zhu, J. T. Vaughan, K. Ugurbil, and W. Chen, "Analysis of wave behavior in lossy dielectric samples at high field." *Magnetic resonance in medicine*, vol. 47, no. 5, pp. 982–9, May 2002. [Online]. Available: http://www.ncbi.nlm.nih.gov/pubmed/11979578

[23] P.-F. Van de Moortele, C. Akgun, G. Adriany, S. Moeller, J. Ritter, C. M. Collins, M. B. Smith, J. T. Vaughan, and K. Uurbil, "B1 destructive interferences and spatial phase patterns at 7 T with a head transceiver array coil." *Magnetic resonance in medicine*, vol. 54, no. 6, pp. 1503–18, Dec. 2005. [Online]. Available: http://www.ncbi.nlm.nih.gov/pubmed/16270333

[24] N. Kinayman, "Microwave Network Theory," in *Modern Microwave Circuits.* Boston, MA: Artech House, ch. 1, pp. 46–64.

[25] J. D. Glover, M. S. Sarma, and T. J. Overbye, "Transmission-Line Differential Equations," in *Power System Analysis and Design*, 4th ed. Thomson, 2008, ch. 5, pp. 242–245.

[26] C. A. Balanis, "Wave Propagation and Polarization," in *Advanced Engineering Electromagnetics.* John Wiley & Sons, 1989, ch. 4, p. 150.

[27] D. K. Cheng, "Theory and Applications of Transmission Lines," in *Field and Wave Electromagnetics*, 4th ed. Addison-Wesley Publishing Company, 1989, ch. 9, pp. 427–509.

[28] P. B. Roemer, W. a. Edelstein, C. E. Hayes, S. P. Souza, and O. M. Mueller, "The NMR phased array." *Magnetic resonance in medicine*, vol. 16, no. 2, pp. 192–225, Nov. 1990. [Online]. Available: http://www.ncbi.nlm.nih.gov/pubmed/2266841

[29] G. Breed, "Transmission Line and Lumped Element Quadrature Couplers," *High Frequency Electronics*, no. November, pp. 44–48, 2009. [Online]. Available: http://highfrequencyelectronics.com/Archives/Nov09/HFE1109_Tutorial.pdf

[30] N. Kinayman and M. I. Aksun, "Hybrid Couplers," in *Modern Microwave Circuits.* Artech House, pp. 400–408.

[31] G. D. Vendelin, A. M. Pavio, and U. L. Rohde, "Noise in Linear Two-Ports," in *Microwave Circuit Design Using Linear and Nonlinear Techniques*, 2nd ed. John Wiley & Sons, 2005, pp. 311–387. [Online]. Available: http://www.knovel.com/web/portal/basic_search/display?_EXT_KNOVEL_DISPLAY_bookid=1974

[32] E. Daw and R. Bradley, "Effect of high magnetic fields on the noise temperature of a heterostructure field-effect transistor low-noise

amplifier," *Journal of applied physics*, vol. 82, no. 4, pp. 1925–1929, 1997. [Online]. Available: http://ieeexplore.ieee.org/xpls/abs_all.jsp?arnumber=5019187

[33] C. Possanzini and M. Boutelje, "Influence of magnetic field on preamplifiers using GaAs FET technology," *Proceedings of the 16th Annual Meeting of the ISMRM*, vol. 16, p. 1123, 2008. [Online]. Available: http://cds.ismrm.org/ismrm-2008/files/01123.pdf

[34] D. Hoult and G. Kolansky, "A magnetic-field-tolerant low-noise SiGe pre-amplifier and T/R switch," *Proceedings of the 18th Annual Meeting of the ISMRM*, vol. 18, no. 2008, p. 2010, 2010. [Online]. Available: http://cds.ismrm.org/protected/10MProceedings/files/649_3988.pdf

[35] L. F. Tiemeijer, R. J. Havens, R. de Kort, and A. J. Scholten, "Improved Y -Factor Method for Wide-Band On-Wafer Noise-Parameter Measurements," *IEEE Transactions on Microwave Theory and Techniques*, vol. 53, no. 9, pp. 2917–2925, 2005.

[36] J.-M. Collantes, R. Pollard, and M. Sayed, "Effects of DUT Mismatch on the Noise Figure Characterization: A Comparative Analysis of Two Y-Factor Techniques," *IEEE Transactions on Instrumentation and Measurement*, vol. 51, no. 6, pp. 1150–1156, Dec. 2002. [Online]. Available: http://ieeexplore.ieee.org/lpdocs/epic03/wrapper.htm?arnumber=1177905

[37] S. Pak, T.-H. Chen, and M. Kumar, "Simple System Yields On-Wafer Noise Parameters," *Microwaves & RF*, vol. 29, no. 7, pp. 103–108, 1990.

[38] D. Vondran, "Noise Figure Measurement: Corrections Related to Match and Gain," *Microwave Journal*, vol. 42, no. 3, pp. 22–38, 1999.

[39] Agilent Technologies, "Agilent PN 4395 / 96-1 How to Measure Noise Accurately Using the Agilent Combination Analyzers," Tech. Rep., 2000.

[40] E. Marsan, "Make Accurate Sub-1 dB Noise Figure Measurements Part 2: The Measurements," *High Frequency Electronics*, vol. 9, no. 2, pp. 18–25, 2010. [Online]. Available: http://highfreqelec.summittechmedia.com/Archives/Feb10/HFE0110_Marsan_Part2.pdf

[41] "Noise Figure Measurement Accuracy The Y-Factor Method Application Note 57-2," Agilent Technologies, Santa Clara, CA, USA, Tech. Rep., 2004.

[42] R. Lane, "The determination of device noise parameters," *Proceedings of the IEEE*, no. August 1969, pp. 1461–1462, 1969. [Online]. Available: http://ieeexplore.ieee.org/xpls/abs_all.jsp?arnumber=1449241

[43] L. Escotte, R. Plana, and J. Graffeuil, "Evaluation of Noise Parameter Extraction Methods," *IEEE Transactions on Microwave Theory and Techniques*, vol. 41, no. 3, pp. 382–387, 1993.

[44] R. Pollard and M. Pierpoint, "Programmable Tuner System Characterizes Gain and Noise," *Microwaves & RF*, no. May, pp. 265–269, 1987.

[45] B. Albinsson, M. Guo, M. Schöön, and H.-O. Vickes, "A New Programmable Load for Noise Parameter Determination," *Microwave Theory and Techniques, IEEE Transactions on*, vol. 39, no. 2, pp. 216–223, 1991.

[46] R. Lane, "A microwave noise and gain parameter test set," in *IEEE International Solid State Circuits Conference*, vol. 78, 1978, pp. 172–173, 274. [Online]. Available: http://ieeexplore.ieee.org/xpls/abs_all.jsp?arnumber=1155852

[47] J. a. Nordmeyer-Massner, N. De Zanche, and K. P. Pruessmann, "Noise figure characterization of preamplifiers at NMR frequencies." *Journal of magnetic resonance*, vol. 210, no. 1, pp. 7–15, May 2011. [Online]. Available: http://www.ncbi.nlm.nih.gov/pubmed/21439871

[48] SIEMENS AG Semiconductor Group, "M8084010.s2p," 1988. [Online]. Available: http://www.infineon.com/

[49] Infineon Technologies, "V2804010.S2P," 2005. [Online]. Available: http://www.infineon.com/

[50] D. I. Hoult and D. Phil, "Sensitivity and power deposition in a high-field imaging experiment." *Journal of magnetic resonance imaging : JMRI*, vol. 12, no. 1, pp. 46–67, Jul. 2000. [Online]. Available: http://www.ncbi.nlm.nih.gov/pubmed/10931564

[51] E. Insko and L. Bolinger, "B1 mapping," *Proceedings of the 11th Annual Meeting of SMRM*, vol. 365, no. 1983, p. 4302, 1992. [Online]. Available: https://www-mrsrl.stanford.edu/studygroup/2/Files/Insko_92.pdf

[52] ——, "Mapping of the radiofrequency field," *Journal of magnetic resonance. Series A*, 1993. [Online]. Available: http://cat.inist.fr/?aModele=afficheN\&cpsidt=4934748

[53] C. H. Cunningham, J. M. Pauly, and K. S. Nayak, "Saturated double-angle method for rapid B1+ mapping." *Magnetic resonance in medicine*, vol. 55, no. 6, pp. 1326–33, Jun. 2006. [Online]. Available: http://www.ncbi.nlm.nih.gov/pubmed/16683260

[54] W. M. Teeuwisse, W. M. Brink, and A. G. Webb, "Quantitative assessment of the effects of high-permittivity pads in 7 Tesla MRI of

the brain." *Magnetic resonance in medicine*, vol. 67, no. 5, pp. 1285–93, May 2012. [Online]. Available: http://www.ncbi.nlm.nih.gov/pubmed/21826732

[55] N. I. Avdievich, S. Oh, H. P. Hetherington, and C. M. Collins, "Improved homogeneity of the transmit field by simultaneous transmission with phased array and volume coil." *Journal of magnetic resonance imaging : JMRI*, vol. 32, no. 2, pp. 476–81, Aug. 2010. [Online]. Available: http://onlinelibrary.wiley.com/doi/10.1002/jmri.22257/abstract

[56] "Varian 4.7T," 2012. [Online]. Available: http://www.invivonmr.ualberta.ca/MRI_systems/4_7T.php

[57] E. a. Barberi, J. S. Gati, B. K. Rutt, and R. S. Menon, "A transmit-only/receive-only (TORO) RF system for high-field MRI/MRS applications." *Magnetic resonance in medicine*, vol. 43, no. 2, pp. 284–9, Feb. 2000. [Online]. Available: http://www.ncbi.nlm.nih.gov/pubmed/10680693

[58] J. T. Vaughan, G. Adriany, M. Garwood, E. Yacoub, T. Duong, L. DelaBarre, P. Andersen, and K. Ugurbil, "Detunable transverse electromagnetic (TEM) volume coil for high-field NMR." *Magnetic resonance in medicine*, vol. 47, no. 5, pp. 990–1000, May 2002. [Online]. Available: http://www.ncbi.nlm.nih.gov/pubmed/11979579

[59] D. W. Carmichael, D. L. Thomas, E. De Vita, M. a. Fernández-Seara, N. Chhina, M. Cooper, C. Sunderland, C. Randell, R. Turner, and R. J. Ordidge, "Improving whole brain structural MRI at 4.7 Tesla using 4 irregularly shaped receiver coils." *NeuroImage*, vol. 32, no. 3, pp. 1176–84, Sep. 2006. [Online]. Available: http://www.ncbi.nlm.nih.gov/pubmed/16806980

[60] T. Vaughan, L. DelaBarre, C. Snyder, J. Tian, C. Akgun, D. Shrivastava, W. Liu, C. Olson, G. Adriany, J. Strupp, P. Andersen, A. Gopinath, P.-F. van de Moortele, M. Garwood, and K. Ugurbil, "9.4T human MRI: preliminary results." *Magnetic resonance in medicine*, vol. 56, no. 6, pp. 1274–82, Dec. 2006. [Online]. Available: http://www.ncbi.nlm.nih.gov/pubmed/17075852

[61] G. D. Clarke, "Overview of the ACR MRI Accreditation Phantom," in *41st Annual Meeting of the AAPM*, 1999, pp. 1–10. [Online]. Available: http://www.aapm.org/meetings/99AM/pdf/2728-58500.pdf

[62] R. H. Stokes, S. Phang, and R. Mills, "Density, conductance, transference numbers, and diffusion measurements in concentrated solutions of nickel chloride at 25 ° C," *Journal of Solution Chemistry*, vol. 8, no. 7, pp. 489–500, Jul. 1979. [Online]. Available: http://link.springer.com/10.1007/BF00655205

[63] P. Vanýsek, “Equivalent Conductivity of Electrolytes in Aqueous Solution,” in *CRC Handbook of Chemistry and Physics*, 93rd ed., W. M. Haynes, Ed., 2013, ch. Section 5:, p. 76. [Online]. Available: http://www.hbcpnetbase.com/

[64] J. G. Och, G. D. Clarke, W. T. Sobol, C. W. Rosen, and S. K. Mun, “Acceptance Testing of Magnetic Resonance Imaging Systems: Report of AAPM Nuclear Magnetic Resonance Task Group No. 6,” Tech. Rep. 34, 1992.

[65] S. Gabriel, R. W. Lau, and C. Gabriel, “The dielectric properties of biological tissues: I. Literature survey.” *Physics in medicine and biology*, vol. 41, no. 11, pp. 2231–49, Nov. 1996. [Online]. Available: http://www.ncbi.nlm.nih.gov/pubmed/8938024

[66] ——, “The dielectric properties of biological tissues : II . Measurements in the frequency range 10 Hz to 20 GHz,” *Physics in medicine and biology*, vol. 41, no. 11, pp. 2251–2269, 1996. [Online]. Available: http://www.ncbi.nlm.nih.gov/pubmed/8938025

[67] ——, “The dielectric properties of biological tissues: III. Parametric models for the dielectric spectrum of tissues.” *Physics in medicine and biology*, vol. 41, no. 11, pp. 2271–93, Nov. 1996. [Online]. Available: http://www.ncbi.nlm.nih.gov/pubmed/8938026

[68] Bird Technologies, “OPERATING INSTRUCTIONS LOAD RESISTOR SERIES 8400,” Tech. Rep. 920, 1998. [Online]. Available: http://www.bird-technologies.com/$\sim$/media/Bird/Files/PDF/Products/manuals/920-8400S.ashx

[69] D. Andreuccetti, R. Fossi, and C. Petrucci, “An Internet resource for the calculation of the dielectric properties of body tissues in the frequency range 10 Hz - 100 GHz,” 1997. [Online]. Available: http://niremf.ifac.cnr.it/tissprop/

[70] T. S. Ibrahim, Y.-K. Hue, and L. Tang, “Understanding and manipulating the RF fields at high field MRI.” *NMR in biomedicine*, vol. 22, no. 9, pp. 927–36, Nov. 2009. [Online]. Available: http://www.ncbi.nlm.nih.gov/pubmed/19621335

[71] P. H. Wardenier, “Local Intensity Shift Artifact,” in *Proceedings of the International Society of Magnetic Resonance in Medicine*, vol. 1989, no. S3, 1989, p. 1175.

[72] A. T. Hess, C. J. Snyder, G. A. Keith, C. T. Rodgers, S. Neubauer, J. T. Vaughan, and M. D. Robson, “Coil tuning with piezoelectric actuators using the MRI signal as the optimization parameter,” in *Proceedings of*

the 21st Annual Meeting of the International Society of Magnetic Resonance in Medicine, vol. 21, 2013, p. 2745.

[73] S.-m. Sohn, L. Delabarre, A. Gopinath, and J. T. Vaughan, "RF coil design with automatic tuning and matching," in *Proceedings of the 21st Annual Meeting of the International Society of Magnetic Resonance in Medicine*, vol. 21, 2013, p. 0731.

[74] G. J. Metzger, C. Snyder, C. Akgun, T. Vaughan, K. Ugurbil, and P.-F. Van de Moortele, "Local B1+ shimming for prostate imaging with transceiver arrays at 7T based on subject-dependent transmit phase measurements." *Magnetic resonance in medicine*, vol. 59, no. 2, pp. 396–409, Feb. 2008. [Online]. Available: http://www.ncbi.nlm.nih.gov/pubmed/18228604